Volume 47 | Number 19 | 7 October 2018 | Pages 7183–7496

Chem Soc Rev

Chemical Society Reviews

rsc.li/chem-soc-rev

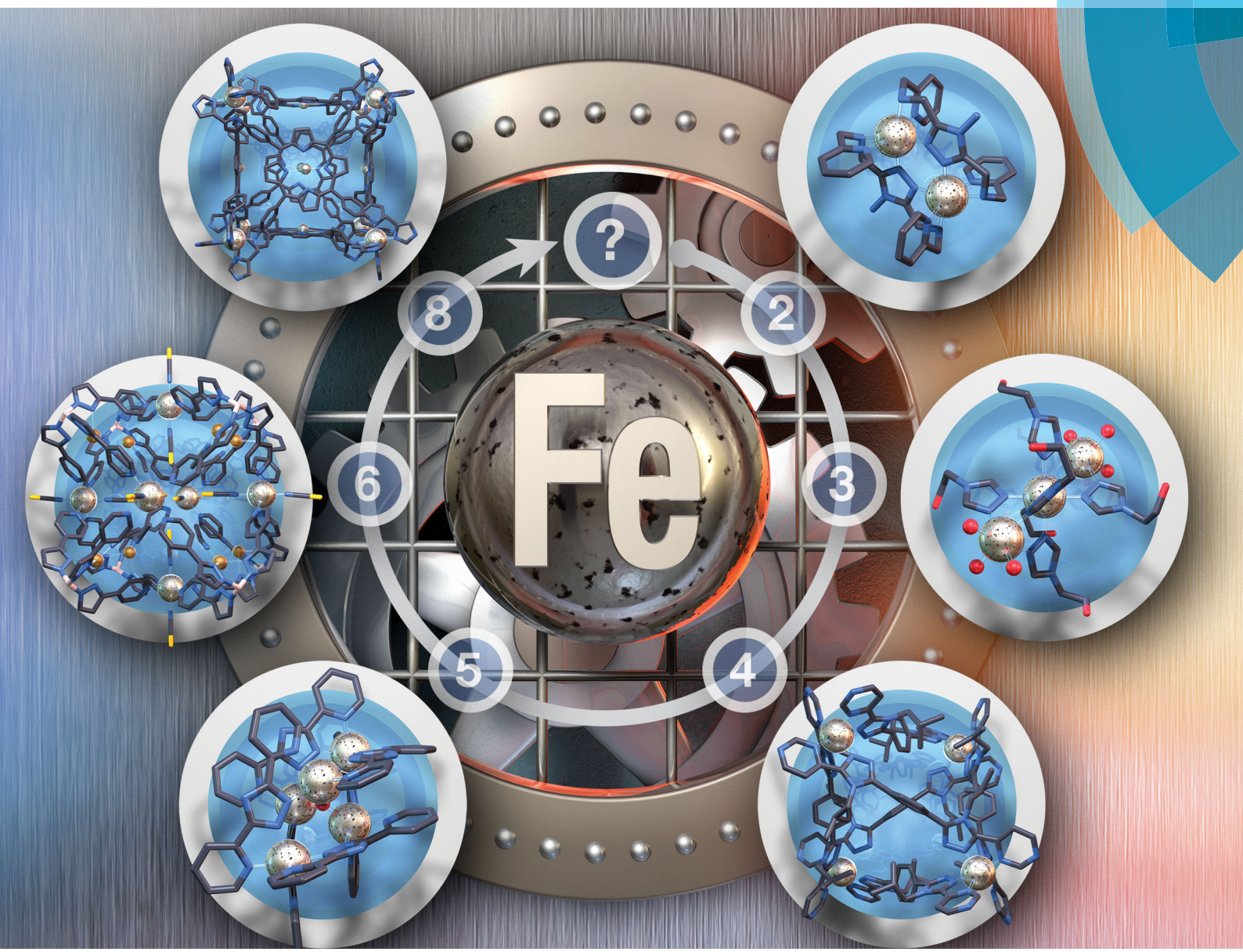

ISSN 0306-0012

ROYAL SOCIETY OF CHEMISTRY

REVIEW ARTICLE

Sally Brooker *et al.*

Spin crossover in discrete polynuclear iron(II) complexes

Chem Soc Rev

REVIEW ARTICLE

View Article Online
View Journal | View Issue

Cite this: *Chem. Soc. Rev.*, 2018, **47**, 7303

Spin crossover in discrete polynuclear iron(II) complexes†

Ross W. Hogue, ‡ Sandhya Singh ‡ and Sally Brooker *

Iron(II) spin crossover (SCO) materials have been widely studied as molecular switches with a wide variety of potential applications, including as displays, sensors, actuators or memory components. Most SCO materials have been either monometallic or polymeric, and it is only relatively recently that chemists have really started to focus on linking multiple metal centres together within the one, discrete, molecule in an effort to enhance the SCO properties, such as abrupt, hysteretic, and multistep switching, as well as the potential for quantum cellular automata, whilst still being readily amenable to characterisation. Here we present a review of the ligand designs of the last two decades that have led to self assembly of discrete di- to poly-nuclear iron(II) complexes of helicate, cage, cube, and other supramolecular architectures with rich SCO activity, and to an increased focus on host–guest interactions. Analysis of selected octahedral distortion parameters (Σ, CShM) reveals interesting differences between these structural types, for example that the iron(II) centres in grids are generally significantly more distorted than those in squares or cages, yet are still SCO-active. Of the 127 complexes reviewed (79 published 2012–Feb. 2018), 54% are dinuclear, 10% trinuclear, 31% tetranuclear, and the remaining 5% are penta, hexa and octanuclear. Of the 93 designer ligands utilised in these polynuclear architectures: 60 feature azoles; 55 provide all donors to the Fe(II) centres (no co-ligands coordinated) and form exclusively 5-membered chelate rings *via* either bidentate azole-imine/pyridine or tridentate heterocycle-imine/amine/thioether/pyridine-heterocycle binding pockets.

Received 30th May 2018

DOI: 10.1039/c7cs00835j

rsc.li/chem-soc-rev

Department of Chemistry and the MacDiarmid Institute for Advanced Materials and Nanotechnology, University of Otago, PO Box 56, Dunedin 9054, New Zealand. E-mail: sbrooker@chemistry.otago.ac.nz

† Electronic supplementary information (ESI) available. See DOI: 10.1039/c7cs00835j

‡ Equal contributions from these authors.

Ross W. Hogue

Dr Ross W. Hogue completed his BSc(Hons) with first class honours in 2012 in Professor Sally Brooker's group at the University of Otago, having scooped many awards during his undergraduate studies, including the Joseph and Emma Mellor Prize for the top final year honours chemistry student. After a gap year travelling the world, he returned to carry out his PhD research, again in the Brooker team (2014–2017). His PhD thesis, "Discrete polynuclear complexes: from spin crossover to hydrogen evolution", was placed on the list of exceptional theses. Ross is currently a postdoctoral fellow working on inorganic materials for non-aqueous redox flow batteries with Dr Kathryn Toghill at Lancaster University, United Kingdom.

Sandhya Singh

Sandhya Singh was awarded a 5 year INSPIRE Fellowship to support her integrated BS-MS studies (2011–2016) at the Indian Institute of Science Education & Research (IISER) Mohali, India. She completed her MS thesis, 'Synthesis, structural characterization, physico-chemical properties and sensing applications of lanthanide based metal organic frameworks (MOFs)', in the research group of Professor Sanjay K. Mandal. During this time she qualified CSIR-UGC NET. In 2017 she moved to Dunedin, New Zealand, to take up a University of Otago PhD scholarship in Professor Sally Brooker's research group, working on the self-assembly of discrete polynuclear spin crossover complexes using designer polytopic ligands.

Introduction

General introduction to spin crossover

Spin crossover (SCO) complexes are an interesting class of materials exhibiting molecular bistability with potential applications in nanotechnological devices such as memory storage units, sensors, actuators or displays.[1–8] The bistability arises from their ability to be switched between two electronic states – high spin (HS) and low spin (LS) – by external stimuli such as a change in temperature or pressure, or light irradiation or guest presence/absence, in a readily detectable and reversible way.

For octahedral $3d^4$–$3d^7$ transition metal ions, there are two ways that electrons can populate the t_{2g} and e_g orbitals (Fig. 1), depending on ligand field splitting (Δ_O) and the energy cost associated with pairing two electrons in the same orbital, the pairing energy (P). If strong field ligands are present, Δ_O is large so the lowest energy configuration involves the pairing of electrons in the t_{2g} set being favoured over population of the e_g set ($\Delta_O > P$), resulting in the maximum amount of paired electrons and thus a LS state. On the contrary, if weak field ligands are present, Δ_O is small and the maximum number of unpaired electrons, *i.e.* the HS state, is the lowest energy configuration as populating the e_g set costs less energy than pairing the electrons in the t_{2g} set ($\Delta_O < P$).[9]

When Δ_O is of a comparable magnitude to P, the possibility of inducing switching between the HS and LS states arises, *i.e.* SCO, by perturbing the system through application of an external stimulus (Fig. 1). SCO can be induced by pressure, magnetic or electric field, light irradiation, and the presence/absence of guest molecules, however, the most common perturbation is a change in temperature, due in large part to facile application and measurement.[1]

Sally Brooker

Professor Sally Brooker (MNZM, FRSNZ, FNZIC, FRSC) studied at the University of Canterbury, New Zealand [BSc(Hons) first class; PhD with Professor Vickie McKee]. After postdoctoral research at Georg-August-Universität Göttingen, Germany with Professor George M. Sheldrick, she took up a Lectureship at the University of Otago where she is now a full Professor. She has been the recipient of numerous awards, most recently including a 2017 Queens Birthday Honour for services to science (MNZM), the 2017 Hector Medal (RSNZ) and 2017 Burrows Award (RACI). Her research interests concern the design, synthesis and full characterisation of, primarily paramagnetic, di- and poly-metallic complexes of transition metal and lanthanide ions with polydentate acyclic and macrocyclic ligands, as these have interesting redox, magnetic, catalytic and photophysical properties (otago.ac.nz/brooker).

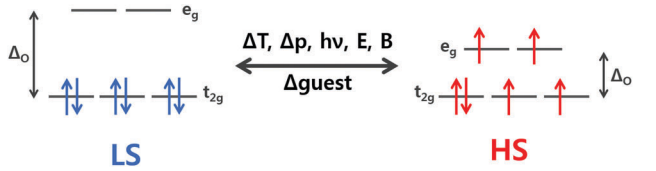

Fig. 1 The d orbital splitting diagram for an octahedral Fe(II) ion. When Δ_O is large, the LS state is adopted (left); when Δ_O is small, the HS state is adopted (right). When Δ_O is tuned for SCO, a change in temperature, pressure, magnetic or electric field, light irradiation, or guest molecules, can result in the switching between HS and LS states.

The HS and LS states have different physical properties, which allows for detection and quantification of SCO by many different methods. Fe(II) SCO compounds often exhibit thermochromism, as the LS state absorbs visible light more strongly than the HS state and usually at distinctly different wavelengths, making UV-vis spectroscopy a useful tool for observing SCO.[9] The HS state has more electrons in the antibonding e_g orbitals than the LS state so has longer metal–ligand bond lengths. Hence X-ray crystallography, often done at more than one temperature, can be used to determine the spin state. This powerful technique can also pinpoint within a structure which ions are HS and which are LS in a mixed spin state system.[10] A direct and detailed readout of the spin state of a SCO compound is the molar magnetic susceptibility (χ_M). In the case of Fe(II) the HS state ($S = 2$) is paramagnetic, while the LS state ($S = 0$) is diamagnetic, so for Fe(II) SCO switches the paramagnetism "on" and "off". The most convenient way to quantify SCO is therefore variable temperature $\chi_M T$ (the product of molar magnetic susceptibility and temperature) measurements, which are routinely performed on modern SQUID, PPMS, or Versalab magnetometers. UV-vis,[9] IR,[11] Raman,[12] NMR,[13–16] Mössbauer,[17] and fluorescence[18] spectroscopies, as well as PXRD[19] and DSC,[20,21] can also be invaluable tools for monitoring SCO.

Advantages of discrete polynuclear systems for SCO

From a materials perspective, SCO systems were identified as potential molecular switch components in memory storage devices some time ago.[22] Hence the development of spin crossover research is heavily influenced by the target of molecular switch and memory applications, with a drive towards SCO which is complete, abrupt, hysteretic, and ideally switchable about room temperature.[23,24] Complete transitions are favoured, as they allow for easier and unambiguous detection of distinct fully HS and fully LS states, while abrupt transitions allow for a large change in output (*e.g.* colour, $\chi_M T$) for a small input (*e.g.* small change in temperature). A thermal hysteresis provides a memory effect, where the spin state depends on the thermal history of the complex. Hence at temperatures within the hysteresis loop the system is bistable and there is the potential for binary information storage. The design of ligands which not only provide the right Δ_O for SCO, but will also facilitate cooperativity within or between complexes which may in turn facilitate abrupt and/or hysteretic spin transitions, is the main goal of many SCO chemists.[25]

Cooperativity arising from crystallographic disorder, crystal packing interactions, or large molecular size/shape differences between HS and LS states, can have a significant influence on SCO properties of complexes, including mononuclear and polymeric complexes, in the solid state.[26] Cooperativity may also be imparted by covalently linking multiple metal centres in a polynuclear or polymeric architecture – but it must be noted that this approach is certainly not guaranteed to lead to cooperativity. That said, a beautiful illustration of the successful application of this 'linking' approach is provided by the now famous Fe(II) 4-*R*-1,2,4-triazole 1-D chain polymers, $[Fe(Rtz)_3]^{2+}$, which feature triply-triazole bridged Fe(II) centres and have remarkably large hysteresis loops around room temperature.[22–24,27–29] A single crystal structure of these widely studied $[Fe(Rtz)_3]^{2+}$ chains was only obtained recently, as despite considerable attention these polymers had resisted all attempts at crystallisation until then.[30]

Discrete polynuclear complexes, in which multiple metal centres are covalently bridged in order to enhance cooperativity, have advantages over polymeric systems in that the design and synthesis can be more controlled, and the characterisation more straightforward.[31–35] Polynuclear complexes, discrete or polymeric, have the added bonus of potential polynary, rather than binary, information storage as multiple spin states can be accessed by multi-step SCO.[23,36,37] Furthermore the geometric arrangement of HS and LS Fe(II) centres within one complex molecule could be used in quantum cellular automata,[38,39] potentially leading to logic gates consisting of only a few molecules.[40,41]

Scope of this review of SCO-active discrete polynuclear Fe(II)

Iron(II) complexes are by far the most common SCO systems studied[1] (of the order of >90%), and almost all subsequent in depth studies by physicists and materials scientists are done on iron(II) systems.[7] Most SCO-active Fe(II) complexes are mononuclear or polymeric, while discrete di to poly-nuclear complexes (Fig. 2) are much rarer.[7,25,31,35,42–44]

This is also true for Fe(III), Co(II), and Mn(II), where only a handful of polynuclear SCO systems are known.[35] In 2013[35] we reviewed the development of discrete polynuclear SCO-active complexes, focussing mainly on the 90 new complexes reported over the period 2004–2011: all of the new complexes were either Fe(II) (68) or Fe(III) (22), and the nuclearities ranged from 63 dinuclear to 3 trinuclear to 14 tetranuclear, with another 10 in an assortment of higher nuclearities including mixed metal clusters. Here we review the various classes of structurally characterised, SCO-active, discrete di- to poly-nuclear complexes, specifically of Fe(II), focussing mostly on those published 2012–2017, as there has been considerable growth in this field since our previous review, including an expansion of the range of architectures employed and the setting of a new record for the largest number of metal centres in a discrete SCO-active complex = 8.[45] The 127 complexes included in this review were identified by a CSD search (version 5.38, November 2016) for dinuclear and trinuclear iron(II) 1,2,4-triazoles (as structural search fragments) and a Scifinder search (28 February, 2018) for

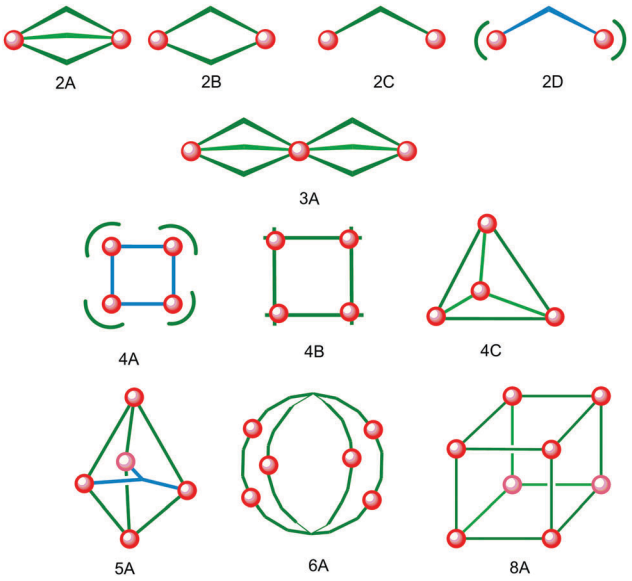

Fig. 2 Topologies observed for the discrete polynuclear SCO-active complexes reviewed herein: dinuclear (**2A–2D**); trinuclear (**3A**); tetranuclear squares (**4A**), grids (**4B**), tetrahedral cages (**4C**); pentanuclear cage (**5A**), hexanuclear nanoball (**6A**) and octanuclear cube (**8A**). Green = di- to polydentate N-donor ligand. Blue = bridging anion.

the keywords "Fe(II) or iron(II)" and "dinuclear or trinuclear or tetranuclear or pentanuclear or hexanuclear or septanuclear or nanoball or octanuclear" and "spin crossover or spin-crossover or spin cross-over or spin transition or spin equilibrium", followed by manually sorting through the resulting 'hits'. The resulting family of 79 discrete polynuclear SCO-active Fe(II) complexes published from 2012 to February 2018, along with selected examples published before then, brings the total reviewed here to 127. They are reviewed in order of increasing nuclearity: dinuclear (**2A–2D**), trinuclear (**3A**), tetranuclear squares (**4A**)/grids (**4B**)/cages (**4C**), pentanuclear (**5A**), hexanuclear 'nanoballs' (**6A**), and octanuclear cubes (**8A**) (Fig. 2).

Of these groups, dinuclear remains the most common of the nuclearities seen for discrete SCO-active complexes. A range of structural types can be identified within this dinuclear class: triply bridged triazole $[Fe_2L_5(NCE)_4]$ and helicate $[Fe_2L_3]$ (Fig. 2, **2A**), doubly bridged helicate and **PMRT**-type and pyridine bridged $[Fe_2L_2]$ (Fig. 2, **2B**), singly ligand linked dinuclear $[Fe_2L]$ (Fig. 2, **2C**) and assorted anion bridged dinuclear complexes with capping ligands (Fig. 2, **2D**).

Dinuclear triply triazole-bridged $Fe_2L_5(NCE)_4$

Fundamental questions in the field of SCO materials are; what factors influence the spin transition temperature ($T_{1/2}$) and transition profile.[29,46] Therefore it is important to study structurally and magnetically similar series of complexes with minor changes in substituents, counterions, and/or solvent molecules. The triply triazole bridged dinuclear complexes (Fig. 2, **2A**) are one type of dinuclear family suitable for such studies, for which crystal structures can be readily determined.

As mentioned in the introduction, the use of N^4-substituted triazoles to form 1D polymers of triply triazole bridged iron(II) is

well known, with wide thermal hysteresis loops and tuneable transition temperatures near room temperature, based on the choice of N^4 substituent.[47] But it is interesting to note that those 1D-chain complexes resisted single crystal X-ray characterisation until 2011.[30] In contrast, dinuclear systems tend to more readily characterised, and facilitate the probing of cooperative effects between the two metal ions.

Here, in the seven examples, plus a solvatomorph, of dinuclear SCO-active $[Fe_2\mathbf{L}_5(NCE)_4]$ with **L** = **L1–L7** (Chart 1), three of the 1,2,4-triazoles provide short N^1N^2, and fairly rigid, bridges between the iron(II) centres, and two more triazoles act as terminal monodentate ligands. The somewhat distorted octahedral geometry of each iron(II) centre is completed by two NCE mono-anions, affording N_6 coordination spheres (Fig. 3). All eight of these complexes showed an abrupt one-step incomplete spin transition, with $T_{1/2}$ in the range of 100–165 K, with no hysteresis loops observed and Fe–Fe distances in same range, 3.6–4.0 Å (Table 1).[18,48–50] As expected, the octahedral distortion parameters (Σ, defined as the sum of the absolute values of the difference of each of the 12 *cis* angles from 90°) for the Fe(II) centres range from 12–19° for LS to the somewhat higher values of 14–35° for HS (Table 1). Some additional details are provided below.

The first of this family of SCO-active dinuclear Fe(II) triply triazole bridged complexes, phenol N^4-substituent (**L1**, Chart 1), $[Fe_2\mathbf{L1}_5(NCS)_4]\cdot 4MeOH$ in the low-spin and high-spin states, was reported in 2011 by Garcia and co-workers.[18] SQUID magnetometry revealed a sharp [HS–HS] to [LS–LS] transition with $T_{1/2}$ = 150 K (Fig. 4a) and the complex was also structurally characterised in both spin states, at 100 and 200 K respectively (Table 1). DSC measurements showed a single phase transition at T_{max} = 155 K (Fig. 4a inset). The SCO event was also able to be monitored by variable temperature fluorescence of the enol, as a bathochromic shift of 20 nm is observed in the emission band across the temperature range of 135–179 K (Fig. 4b).

Fresh crystals of $[Fe_2\mathbf{L2}_5(NCS)_4]\cdot 5MeOH$ showed a gradual, approximately half, SCO centred at 115 K.[50] In contrast, a bulk powder sample of unsolvated $[Fe_2\mathbf{L2}_5(NCS)_4]$ remained [HS–HS] to low temperature. By introducing electron withdrawing chloride substituents (**L3**, Chart 1), the ligand field was adjusted, giving a more complete spin transition, with $T_{1/2}$ = 150 K. The LIESST (light-induced excited spin state trapping) effect was also seen for the $[Fe_2\mathbf{L3}_5(NCS)_4]$ system: irradiating with 532 nm light at 5 K the χ_mT value increased abruptly to 4.6 cm^3 K mol^{-1}, which was attributed to SCO of the two Fe(II) centres from LS to HS*, with a $T_{(LIESST)}$ of 61 K.[48]

Liu and co-workers used a naphthalene group as the N^4 substituent, generating $[Fe_2\mathbf{L4}_5(NCSe)_4]\cdot 2DMF\cdot 2H_2O$ (**L4**, Chart 1) which showed an abrupt [HS–HS] to [LS–LS] SCO with $T_{1/2}$ = 164 K (Fig. 5a).[49] They also studied the photoinduced SCO. Upon irradiation with 532 nm light at 10 K for 2 h, χT increased max. to 2.5 cm^3 K mol^{-1} at 48 K, consistent with the LS Fe(II) centres undergoing partial conversion to metastable HS*. At 10 K, cycles of irradiation at 532 nm followed by irradiation at 808 nm switched the χT value reversibly between 1.23 to 0.47 cm^3 K mol^{-1} implying reversible SCO between metastable HS* and LS (Fig. 5b).[49]

Wang and co-workers studied the effect of differing solvents of crystallisation, comparing $[Fe_2\mathbf{L5}_5(NCS)_4]\cdot MeOH\cdot EtOH$ and $[Fe_2\mathbf{L5}_5(NCS)_4]\cdot 2EtOH$ and showing that the $T_{1/2}$ value for the observed half SCO increased slightly, from 116 K to 122 K.[51] Changing the N^4 substituent from phenyl (**L5**) to 2-pyridyl (**L6**, Chart 1) resulted in a negligible effect magnetically, with the $T_{1/2}$ remaining at 116 K.[52] In contrast, changing from a phenyl (**L5**) to *p*-tolyl (**L7**)[53] N^4 substituent (Chart 1), had a dramatic impact, with two dinuclear $Fe_2\mathbf{L7}_5(NCS)_4$ units bridged by hydrogen bonding to the coordinated water molecules of a mononuclear $Fe\mathbf{L7}_2(NCS)_2(H_2O)_2$ unit. But the magnetic behaviour of the resulting material is not much different from other triply triazole bridged dinuclear Fe(II) complexes; it undergoes SCO centred at 111 K, with variable temperature magnetometry and Mössbauer spectroscopy both consistent with four out of five Fe(II) centres transitioning from HS to LS, *i.e.* the dinuclear $Fe_2\mathbf{L7}_5(NCS)_4$ units are SCO-active while the mononuclear $Fe\mathbf{L7}_2(NCS)_2(H_2O)_2$ unit remains HS to low temperature.[53]

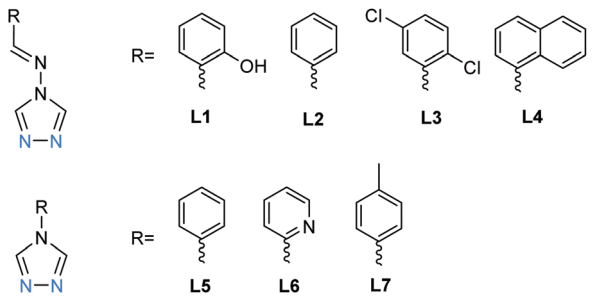

Chart 1 The seven ligands, **L1–L7**, all of which are N^4-substituted 1,2,4-triazoles, reported in the literature to form SCO-active triply-triazole bridged dinuclear complexes.

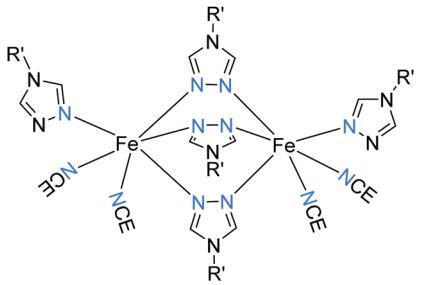

Fig. 3 Schematic representation of $[Fe_2\mathbf{L}_5(NCE)_4]$ where **L** = **L1–L7**, E = S or Se (**L** = **L4**).

Dinuclear triply stranded helicates $Fe_2\mathbf{L}_3$

The other type of triply bridged dinuclear Fe(II) SCO-active complex is the helicate architecture, $Fe_2(\mathbf{L})_3$ (Fig. 2, **2A**). Helicates are made through controlled and predictable self assembly of carefully designed components. They are intrinsically stable, and have wide ranging properties owing to their versatility with respect to choice of metal ion.[54–60] Through careful design of the polydentate ligand, the cavity of such helicates can be optimised for favourable host–guest interactions, which can

Table 1 Selected parameters for SCO-active triply-triazole bridged dinuclear Fe(II) complexes (Fig. 2, **2A**). LS centres in italics

Complex	T (K)	Fe–Fe (Å)	Σ (°)	Spin state	$T_{1/2}$ (K)	Lit.
$[Fe_2\mathbf{L1}_5(NCS)_4]\cdot 4MeOH$	100	3.65	*15*	2LS	150	18
	200	3.97	19	2HS		
$[Fe_2\mathbf{L2}_5(NCS)_4]\cdot 3.5MeOH$	100	3.79	*17*/20	LS–HS	115	50
	250	3.97	23/23	HS–HS		
$[Fe_2\mathbf{L3}_5(NCS)_4]\cdot H_2O$	100	3.72	*13*/*13*	LS–LS	150	48
	180	3.96	*17*/35	LS–HS		
$[Fe_2\mathbf{L4}_5(NCSe)_4]\cdot 2DMF\cdot 2H_2O$	92	3.63	*12*/*13*	LS–LS	164	49
	280	3.95	24/20	HS–HS		
$[Fe_2\mathbf{L5}_5(NCS)_4]\cdot MeOH\cdot EtOH$	100	3.92	*19*/24	LS–HS	116	51
	296	3.99	16/26	HS–HS		
$[Fe_2\mathbf{L5}_5(NCS)_4]\cdot 2EtOH$	296	3.97	14/19	HS–HS	122	51
$[Fe_2\mathbf{L6}_5(NCS)_4]\cdot MeOH\cdot EtOH$	173	3.92	*19*/24	LS–HS	116	52
$2[Fe_2\mathbf{L7}_5(NCS)_4][Fe\mathbf{L7}_2(NCS)_2(H_2O)_2]$	295	3.94	23/24/8	HS–HS, HS	111	53

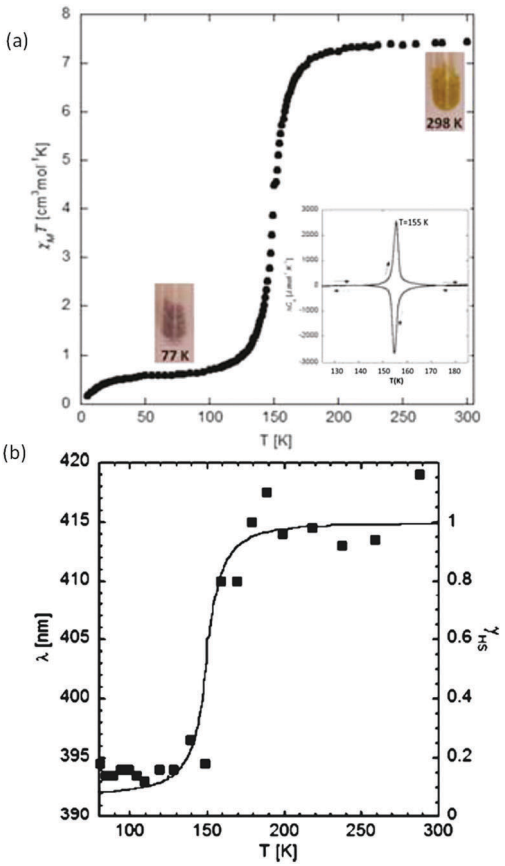

Fig. 4 Data obtained on $[Fe_2\mathbf{L1}_5(NCS)_4]\cdot 4MeOH$: (a) plot of X_mT *vs.* T. The inset shows the DSC peaks, both exothermic and endothermic. (b) λ_{max} of the emission spectrum *vs.* T (black dots), follows the γ_{HS} determined from the SQUID data (solid line). (a) Adapted and (b) reproduced with permission from ref. 18. Copyright 2011 ACS.

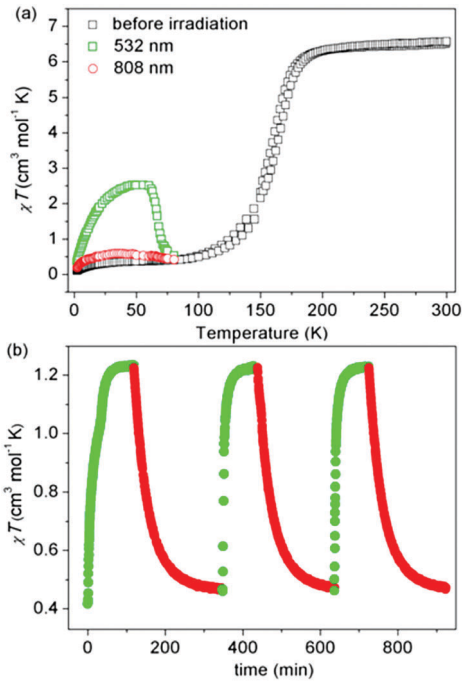

Fig. 5 Data obtained on $[Fe_2\mathbf{L4}_5(NCSe)_4]\cdot 2DMF\cdot 2H_2O$: (a) χT *vs.* T (black), including before and after irradiation at 10 K at the stated wavelengths (green and red). (b) χT *vs.* time during cycles of successive irradiation at 532 nm (green) and 808 nm (red) at 10 K. (a and b) Reproduced with permission from ref. 49. Copyright 2017 ACS.

dictate the self-assembly process, and can also be exploited for tuning of the metal ion properties.[61–65] In line with the theme of this review, only Fe(II) examples of this architecture which are SCO-active are discussed herein.

A reliable route to such helicates is the 2 : 3 combination of octahedral Fe(II) ions and bis-bidentate linker ligands to give dinuclear Fe_2L_3 helicates, of which only a handful of examples, 14, have been reported to be SCO-active. Indeed only nine ligands (Chart 2) have been used to produce all of the SCO-active Fe_2L_3 helicates reported to date,[61,66–72] the first of which was reported in 1998.[66] In these helicates the three ligands provide all of the donor atoms to the two Fe(II) centres which results in greatly increased Σ values (54–94°, Table 2; 64–159°, Table 3; 59–116°, Table 4) compared to those in the triply bridged triazoles with monodentate co-ligands (12–35°, Table 1).

Williams and co-workers reported the first SCO-active Fe(II) dinuclear triply stranded helicate, based on the bis[2-(pyrid-2′-yl)benzimidazol-5-yl]methane ligand **L8** (Chart 2).[66,73] The SCO was monitored in CD_3CN solution by the Evans method, and revealed a gradual and far from complete spin transition over the measured temperature range (240–330 K). Interestingly, the mononuclear analogue of the 2-(pyrid-2-yl)benzimidazole

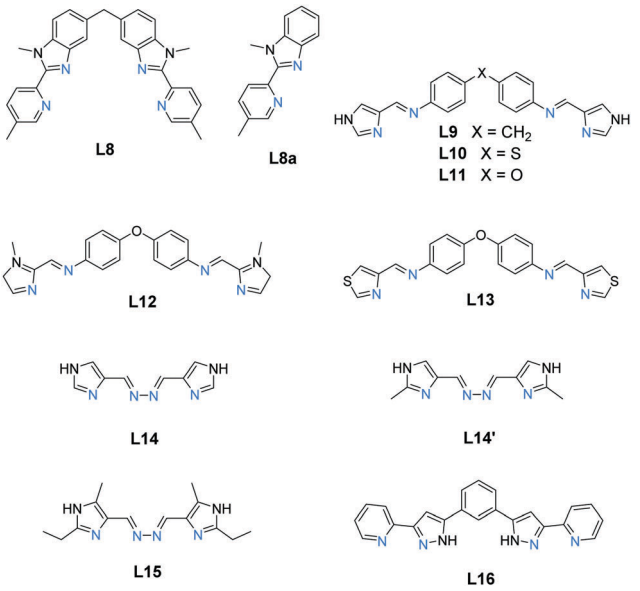

Chart 2 The nine ligands, **L8–L16**, reported in the literature to form SCO-active Fe_2L_3 helicates. All are bis-bidentate and provide N_6 donor sets to the octahedral Fe(II) metal ions.

"half" ligand, $[Fe\mathbf{L8a}_3](ClO_4)_2$, was also studied, and it was found that the LS state is better stabilised in the dinuclear $[Fe_2(\mathbf{L8})_3]^{4+}$ helicate than in mononuclear $[Fe\mathbf{L8a}_3](ClO_4)_2$.

A family of $[Fe_2(\mathbf{L9})_3]X_4$ helicates prepared using a neutral bis-imidazoleimine ligand which features a central methylene linker (**L9**, Chart 2; bis-imine made from 4(5)-imidazolecarboxaldehyde and 4,4′-methylenedianiline) was reported by Hannon and co-workers in 2004 (Fig. 6a).[67] Variation of the counter-anion X (PF_6^-, BF_4^-, ClO_4^-) led to different solid state SCO behaviours being observed (Fig. 6b). While the use of PF_6^- or BF_4^- resulted in SCO transitions from fully HS to ~20% HS, centred at approximately 200 K and 150 K respectively, the ClO_4^- analogue underwent a HS to ~50% HS transition, *i.e.* half SCO, centred around 150 K (Fig. 6b). Subsequent Mössbauer experiments indicated that for $[Fe_2\mathbf{L9}_3](ClO_4)_4$, the half SCO occurs *via* half of the helicates undergoing a complete [HS–HS] to [LS–LS] transition and the other half remaining [HS–HS], giving 1 : 1 [HS–HS] : [LS–LS], as no localised [HS–LS] species was detected.[74]

The ditopic ligand scaffold of **L9** is well predisposed to forming Fe_2L_3 helicates, so it is unsurprising that several more recent examples of SCO-active complexes have employed thioether and ether analogues of **L9**, **L10–L13** (Chart 2).

Li and co-workers recently reported the Fe_2L_3 helicates of the most closely related thioether and ether analogues of **L9**, **L10** and **L11**, which differ only in the linker (methylene *vs.* thioether *vs.* ether), whilst providing the same imidazole-imine binding pocket.[71] The magnetic properties of $[Fe_2(\mathbf{L10})_3](BF_4)_4$ and $[Fe_2(\mathbf{L11})_3](BF_4)_4$ were compared to that of a re-synthesised sample of the $[Fe_2(\mathbf{L9})_3](BF_4)_4$ helicate originally reported by Hannon and co-workers. All three samples were found to undergo a [HS–HS] → [HS–LS] transition with a 15 K wide hysteresis loop, but with $T_{1/2}$ values which varied by 40 K. Changing the linker group of the ligand from methylene to thioether to ether was shown to influence the crystal packing and the intramolecular Fe–Fe separation varied by up to 0.16 Å (Table 2) and the inter-helicate Fe–Fe separation by up to 0.75 Å. But these structural differences were difficult to correlate to the SCO behaviours, which are possibly influenced more heavily by harder to predict inter-helicate interactions *e.g.* CH–π or hydrogen bonding interactions. This is perhaps illustrated by the differences in the packing and SCO of $[Fe_2(\mathbf{L9})_3](BF_4)_4$ seen in the reports of Hannon *versus* Li. While Hannon crystallised $[Fe_2(\mathbf{L9})_3](BF_4)_4$ from acetonitrile by diisopropyl ether vapour diffusion and observed a hydrogen bonded 2D network of helicates (through imidazole-NH and BF_4^- counteranions) which exhibited abrupt SCO,[67] Li crystallised the material by diethyl ether vapour diffusion, observed no hydrogen-bonded network, and a less abrupt SCO.[71]

While most SCO-active Fe_2L_3 helicates exhibit [HS–HS] to 50% HS transitions (half SCO), a desolvated $[Fe_2(\mathbf{L12})_3](ClO_4)_4$ complex based on the methylimidazole analogue of **L11**, **L12** (Chart 2, bis-imine made from 1-methyl-2-imidazole-carboxaldehyde and 4,4′-oxydianiline), was shown by Kruger and co-workers to undergo a complete SCO (Fig. 7b).[69] The χT value at 300 K was 6.6 cm^3 K mol^{-1}, consistent with two uncoupled HS Fe(II) ions. At 80 K, all HS transit into LS with $T_{1/2}$ 140 K. At low temperature, a metastable fully [HS–HS] state can be populated by light irradiation, providing a remarkable example of the LIESST effect. Subsequently, when the complex was instead obtained as $[Fe_2\mathbf{L12}_3](ClO_4)_4{\cdot}4H_2O$, only half SCO was achieved, and the $T_{1/2}$ value was found to be dependent on the degree of hydration, thus the helicate exhibits moisture-sensitive SCO.[75]

In 2018, Li and co-workers went on to report the $[Fe_2(\mathbf{L13})_3](BF_4)_4$ helicate of a thioazolyl-imine analogue, **L13**, of the ligand **L11** (Chart 2).[72] The complex, $[Fe_2(\mathbf{L13})_3](BF_4)_4$, was structurally characterised in the [LS–LS] state at 100 K, and again at 298 K at which temperature it showed slightly increased Fe–N bond lengths and octahedral distortion parameter at one of the Fe(II) centres, consistent with slight population of a [HS–LS] state. Indeed, the magnetic data show that at 298 K there is an onset of a SCO, which becomes complete above room temperature, with $T_{1/2}$ = 348 K. This complete [LS–LS] to [HS–HS] SCO was also observed by X-ray photoelectron spectroscopy (XPS). This report provides a nice example of deliberately tuning the $T_{1/2}$ of a SCO-active complex, in this case by ~200 K, by changing the ligand field strength of these ether linked ditopic ligands upon changing the terminal imidazole group of the **L11** and **L12** ligands to the stronger ligand field thiazole group of **L13** (Chart 2).

Abrupt SCO was achieved for two complexes of a 'tight' Fe_2L_3 helicate architecture derived from the relatively short **L14** ligand (Chart 2) reported by Sunatsuki, Kojima, and co-workers.[68] This short, conjugated, ditopic **L14** ligand is prepared by the 2 : 1 condensation of imidazole-4-carbaldehyde with hydrazine hydrate. In order to bind in a bis-bidentate manner, and provide a two-atom NN bridge between the two iron(II) centres, the ligand twists significantly away from being flat, forming the triple

Table 2 Selected parameters for SCO-active triply-stranded helicate dinuclear Fe(II) complexes (Fig. 2, **2A**). LS centres in italics

	T (K)	Σ (°)	Fe–Fe (Å)	Spin state	$T_{1/2}$ (K)	Lit.
$[Fe^{II}_2(\mathbf{L8})_3](ClO_4)_4$	295	*62*	9.16	2LS	341, 402	66 and 73
$[Fe^{II}_2(\mathbf{L9})_3](PF_6)_4$	180	*64*	11.40	2LS	Not stated	67
$[Fe^{II}_2(\mathbf{L9})_3](BF_4)_4$	180	*63*, 83	11.56	LS–HS	Not stated	
$[Fe^{II}_2(\mathbf{L9})_3](ClO_4)_4$	180	76, 94	11.58	HS–HS	Not stated	
$[Fe^{II}_2(\mathbf{L9})_3](BF_4)_4$	100	76	11.71	2HS/LS	↓155 ↑170	71
$[Fe^{II}_2(\mathbf{L10})_3](BF_4)_4$	100	*60*, 90	11.78	LS–HS	↓115 ↑130	71
$[Fe^{II}_2(\mathbf{L11})_3](BF_4)_4$	100	84.9, 74.5	11.62	HS–HS/LS	↓150 ↑165	71
$[Fe^{II}_2(\mathbf{L12})_3](ClO_4)_4{\cdot}2MeCN$	150	*65*, *62*	11.45	LS–LS	140	69
$[Fe^{II}_2(\mathbf{L12})_3](ClO_4)_4{\cdot}1.5H_2O$	150	*62*, 85	11.45	LS–HS	210–265	75
$[Fe^{II}_2(\mathbf{L13})_3](BF_4)_4$	100	*54*, *65*	11.33	LS–LS	348	72
$[Fe^{II}_2(\mathbf{L13})_3](BF_4)_4$	298	*58*, 70	11.36	LS–LS/HS		

Table 3 Selected parameters for SCO-active triply-stranded 'tight' helicate dinuclear Fe(II) complexes (Fig. 2, **2A**) of the 'short' **L14–L15** ligands (Chart 2). LS centres in italics

	T (K)	Σ (°)	Fe–Fe (Å)	Spin state	$T_{1/2}$ (K)	Lit.
$[Fe^{II}_2(\mathbf{L14})_3](BF_4)_4{\cdot}2MeNO_2{\cdot}1H_2O$	173	*66*, 159	3.87	LS–HS	↑190 ↓183	68
$[Fe^{II}_2(\mathbf{L14})_3](ClO_4)_4{\cdot}5MeNO_2$	103	*64*, 152	3.85	LS–HS	240	
	293	116, 124	4.04	HS–HS		
$[Fe^{II}_2(\mathbf{L15})_3](ClO_4)_4{\cdot}3MeCN{\cdot}0.5H_2O$ (plate)	163	138, *65*	3.84	HS–LS	120	70
$[Fe^{II}_2(\mathbf{L15})_3](ClO_4)_4{\cdot}2MeCN$ (block)	113	132, 135	4.178	HS–HS	HS	70

Table 4 Selected parameters for SCO-active triply-stranded helicate dinuclear Fe(II) complexes (Fig. 2, **2A**) of the **L16** ligand (Chart 2) which can encapsulate a halide ion. LS centres in italics

	T (K)	Σ (°)	Fe–Fe (Å)	Spin state	$T_{1/2}$ (K)	Lit.
$Cl@[Fe_2(\mathbf{L16})_3]Cl(PF_6)_2{\cdot}5.7MeOH$	100	116, *59*	9.73	HS–LS	302	61
	280	113, *62*	9.73	HS–LS		
$Cl@[Fe_2(\mathbf{L16})_3]Cl(PF_6)_2{\cdot}3MeOH{\cdot}H_2O$	90	*62*	9.67	2LS	160, 265	
	300	95	9.80	2HS		
$Br@[Fe_2(\mathbf{L16})_3]Br(PF_6)_2{\cdot}4MeOH$	100	114, *61*	9.67	HS–LS	258	
	280	110, 84	9.70	HS–HS		
$Br@[Fe_2(\mathbf{L16})_3]Br(PF_6)_2{\cdot}MeOH{\cdot}H_2O$	90	*64*	9.69	2LS	200	
	296	97	9.79	2HS		

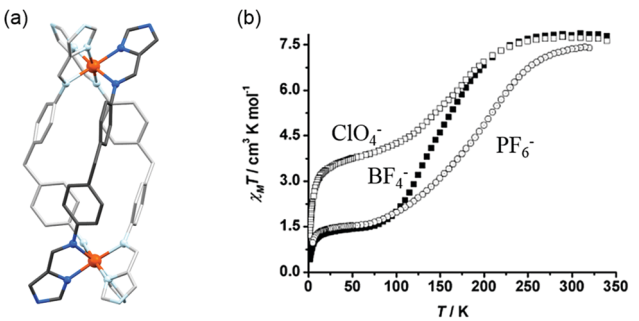

Fig. 6 Data obtained on the family of three $[Fe_2(\mathbf{L9})_3]X_4$ helicates: (a) the structure of the $[Fe_2(\mathbf{L9})_3]^{4+}$ cation. (b) $\chi_M T$ *vs.* T for the $[Fe_2(\mathbf{L9})_3]X_4$ helicates where X = PF_6^-, BF_4^- or ClO_4^-. Structure redrawn from CCDC data.[67] (b) Adapted with permission from ref. 67. Copyright 2004 John Wiley and Sons.

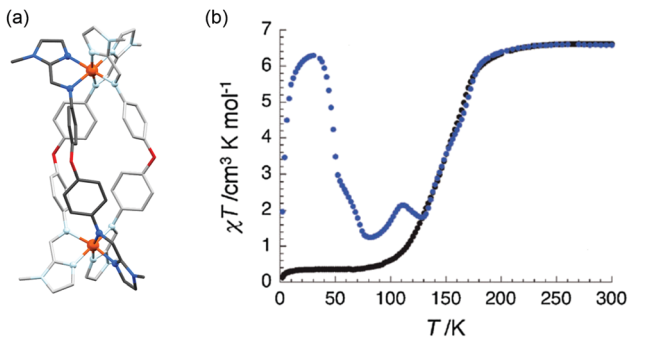

Fig. 7 Data obtained on $[Fe_2(\mathbf{L12})_3](ClO_4)_4$ (a) structure of the $[Fe_2(\mathbf{L12})_3]^{4+}$ cation. (b) Thermal SCO (black data) and LIESST (blue data) behaviour of desolvated $[Fe_2(\mathbf{L12})_3](ClO_4)_4$. Structure redrawn from CCDC data.[69] (b) Adapted with permission from ref. 69. Copyright 2009 RSC.

helicate complex, $[Fe_2(\mathbf{L14})_3](ClO_4)_4$ (Fig. 8a) with very short Fe–Fe distances ~4 Å (Table 3) for a helicate (Tables 2 and 4). This undergoes an abrupt [HS–HS] to 50% HS transition at 240 K (Fig. 8b, blue data), while the BF_4^- analogue has a lower $T_{1/2}$,

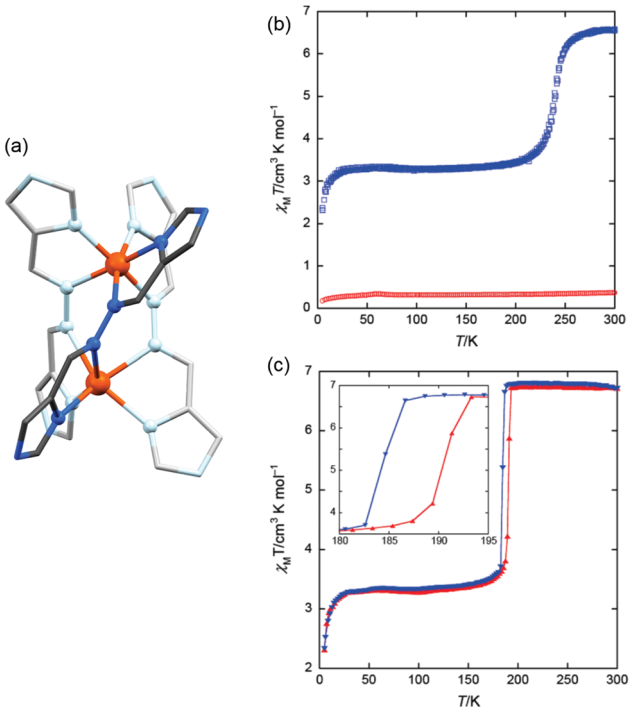

Fig. 8 Data obtained on $[Fe_2(\mathbf{L14})_3](ClO_4)_4$, $[Fe_2(\mathbf{L14})_3](BF_4)_4$ and $[Fe_2(\mathbf{L14'})_3](ClO_4)_4$: (a) structure of the cation of the $[Fe_2(\mathbf{L14})_3]^{4+}$ helicate. (b) $\chi_M T$ *vs.* *T* for $[Fe_2(\mathbf{L14})_3](ClO_4)_4$ in blue, and the methylimidazole analogue, $[Fe_2(\mathbf{L14'})_3](ClO_4)_4$ helicate, in red. (c) $\chi_M T$ *vs.* *T* for $[Fe_2(\mathbf{L14})_3](BF_4)_4$. Structure redrawn from CCDC data.[68] (b and c) Reproduced with permission from ref. 68. Copyright 2009 ACS.

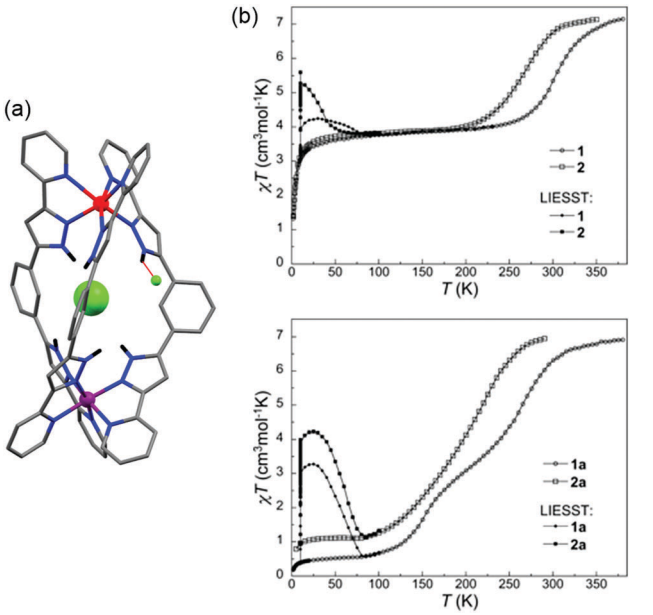

Fig. 9 (a) [HS–LS] $\{Cl@[Fe_2(\mathbf{L16})_3]\}Cl(PF_6)_2 \cdot 5.7MeOH$ structure (PF_6^- anions and solvents omitted), showing the encapsulated Cl^- (spacefill) nearer the HS Fe(II) (red) than the LS Fe(II) (purple), and also the external Cl^- which interacts with one pyrazole NH closer to HS Fe(II) (red dashed line). (b) Thermal SCO and LIESST effect of the helicates $\{Cl@[Fe_2(\mathbf{L16})_3]\}Cl(PF_6)_2 \cdot 5.7MeOH$ (**1** in this figure) and $\{Br@[Fe_2(\mathbf{L16})_3]\}Br(PF_6)_2 \cdot 4MeOH$ (**2** in this figure), and the corresponding SCSC generated helicates $\{Cl@[Fe_2(\mathbf{L16})_3]\}Cl(PF_6)_2 \cdot 3MeOH \cdot H_2O$ (**1a** in this figure) and $\{Br@[Fe_2(\mathbf{L16})_3]\}Br(PF_6)_2 \cdot MeOH \cdot H_2O$ (**2a** in this figure). Structure redrawn from CCDC data.[61] (b) Reproduced with permission from ref. 61. Copyright 2016 John Wiley and Sons.

at 190 K, with a hysteresis loop 7 K wide (2 K min^{-1} scan rate) (Fig. 8c). The methylimidazole analogue of L14, L14′ results in a [LS–LS] complex (no SCO) in the analogous perchlorate complex, $[Fe_2(\mathbf{L14'})_3](ClO_4)_4$ (Fig. 8b, red data), which the authors attribute to being a direct result of tuning of the ligand field by introduction of an electron donating group to the ligand scaffold.

A follow-up publication from the same authors reported the SCO-active dinuclear helicate $[Fe_2(\mathbf{L15})_3](ClO_4)_4 \cdot$solvents based on the (electron donating) ethyl/methyl substituted analogue, **L15**, of the bis-imidazole ligand **L14** (Chart 2).[70] $[Fe_2(\mathbf{L15})_3](ClO_4)_4 \cdot$solvents crystallised as two solvatomorphs, block shaped and plate crystals, both of which were structurally characterised (Table 3). The plate crystals, $[Fe_2(\mathbf{L15})_3](ClO_4)_4 \cdot H_2O$, undergo a half SCO from [HS–HS] to [HS–LS] at 120 K, with a localised [HS–LS] state confirmed by X-ray crystallography, and no [LS–LS] state is accessible. On the other hand, the block shape crystals, $[Fe_2(\mathbf{L15})_3](ClO_4)_4 \cdot \frac{1}{2}CH_3CN$, remain [HS–HS] to low temperature, as observed by SQUID magnetometry and X-ray crystallography. These results highlight the large influence that crystal packing and/or lattice solvent content can have on the SCO properties of a system, in this case overruling the expected electronic influence of methyl/ethyl substituents.

An example of a SCO-active Fe_2L_3 helicate which is triply switchable – by temperature, light, and guests – was reported by Aromi and co-workers in 2016.[61] Here the ligand strand, **L16** (Chart 2), consists of two bidentate pyrazole-pyridine units, linked by a central 1,3-benzene group, and features two internally facing 'spare' NH moieties. Due to these NH groups, the resulting triply stranded dinuclear helicates, $\{X@[Fe_2(\mathbf{L16})_3]\}X(PF_6)_2$ ($X = Cl^-$ or Br^-), can encapsulate a halide counteranion. One halide ion is encapsulated inside the cavity defined by the three ligand strands and the other is external (Fig. 9a). For the as-synthesised helicate structures, the encapsulated halide ion interacts with the six pyrazole rings through hydrogen bonding to the internally facing NH moieties, and is closer to one of the two Fe(II) centres. The external halide counteranion is closer to the same Fe(II) centre, and has one X···H–N interaction with a pyrazole ring. These out-of-sphere interactions stabilise this Fe(II) centre in the HS state down to low temperatures, and, as such, only a half SCO, to a localised [HS–LS] state, as determined by an X-ray structure determination at 100 K (Fig. 9a), is observed (Table 4).

The $X = Cl^-$ and $X = Br^-$ helicates are isostructural, with the only difference being the nature of the encapsulated/external halide ions, yet the $T_{1/2}$ of the SCO is shifted down by 40 K on changing from $X = Cl^-$ to Br^-, highlighting the significant impact of the out-of-sphere interactions on the ligand field strength and hence SCO properties. In both compounds, a single crystal to single crystal (SCSC) transformation of the helicate, by partial methanol solvent loss and uptake of water, results in the encapsulated halide ions being equidistant to the two Fe(II) centres, thus breaking the structural non-equivalence, and full

[HS–HS] to [LS–LS] SCO is observed (Fig. 9b and Table 4). Attempts to encapsulate the larger I^- anion were unsuccessful and instead yielded complexes with external I_3^- counteranions. These persisted in the [HS–HS] state to low temperatures.

Doubly stranded dinuclear helicates, Fe_2L_2

While there are numerous examples of SCO-active dinuclear Fe(II) triply stranded helicates made from bis-bidentate ligands, doubly stranded systems are rare (Fig. 2, **2B**). For just two ligand strands to complete the octahedral coordination sphere of two octahedral Fe(II) centres in a helicate complex, the ditopic ligand must be bis-terdentate. To date, only two such ligands, the neutral 1,2,3-triazole-based ligands **L17** and **L18** (Chart 3), have been reported to give SCO-active Fe_2L_2 helicates.[76,77]

In 2016 Hagiwara, Tanaka and Hora reported the first SCO-active dinuclear double helicate, $[Fe_2(\mathbf{L17})_2](PF_6)_4{\cdot}5H_2O{\cdot}MeCN$ (Fig. 10a).[76] X-ray structural analysis at 120 K revealed two identical LS Fe(II) centres in the dication, and no higher temperature structures could be obtained due to loss of crystallinity upon desorption of lattice solvent molecules. SQUID magnetometry on $[Fe_2(\mathbf{L17})_2](PF_6)_4{\cdot}5H_2O{\cdot}MeCN$ showed that the helicate remains [LS–LS] to 300 K, but measurements above room temperature revealed an unusual two-step SCO. Upon warming from 300 K to 435 K, the $\chi_M T$ value increases steadily from

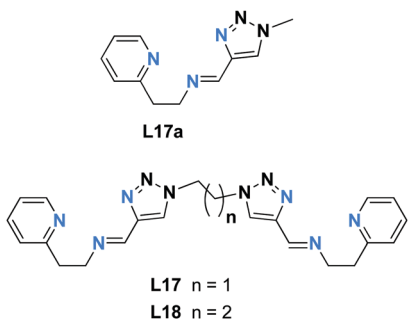

Chart 3 The two ditopic 1,2,3-triazole-based ligands, **L17** and **L18**, known to give dinuclear Fe(II) doubly stranded double helicates. Both are bis-terdentate and provide N_6 donor sets to the octahedral Fe(II) metal ions.

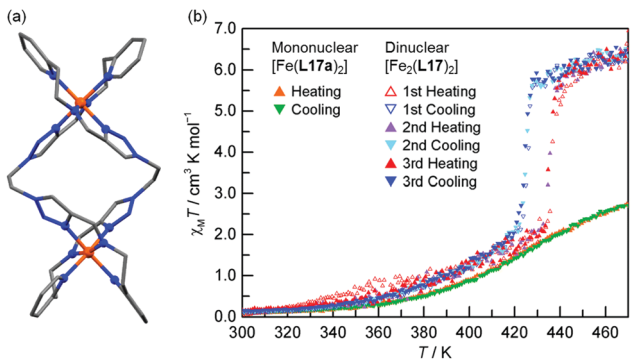

Fig. 10 (a) Structure of the cation $[Fe_2(\mathbf{L17})_2]^{4+}$ of $[Fe_2(\mathbf{L17})_2](PF_6)_4{\cdot}5H_2O{\cdot}MeCN$ (b) $\chi_M T$ *vs.* *T* for $[Fe_2(\mathbf{L17})_2](PF_6)_4{\cdot}5H_2O{\cdot}MeCN$ and the mononuclear analogue $[Fe(\mathbf{L17a})_2](PF_6)_2$. Structure redrawn from CCDC data.[76] (b) Adapted, with permission, from ref. 76. Copyright 2016 RSC.

Table 5 Selected parameters for SCO-active doubly-stranded helicate dinuclear Fe(II) complexes (Fig. 2, **2B**) of **L17–L18** (Chart 3). LS centres in italics

	T (K)	Σ (°)	Fe–Fe (Å)	Spin state	$T_{1/2}$ (K)	Lit.
$[Fe^{II}_2(\mathbf{L17})_2](PF_6)_4{\cdot}5H_2O{\cdot}MeCN$	120	*43*	7.85	2LS	↑437 ↓426	76
$[Fe^{II}_2(\mathbf{L18})_2](AsF_6)_4{\cdot}5H_2O{\cdot}MeCN$	120	*48*, *48*	10.87	LS–LS	↑485 ↓401	77

0.1 to 2.6 cm^3 K mol^{-1}, consistent with a gradual SCO to ~40% HS (Fig. 10b, red data). An abrupt second step is then observed between 435 and 443 K, with $\chi_M T$ increasing to 5.6 cm^3 K mol^{-1}, before again increasing gradually to 6.5 cm^3 K mol^{-1} at 470 K (Fig. 10b, red data), consistent with a [HS–HS] state. In cooling mode (Fig. 10b, blue data), the abrupt transition occurs at 426 K giving the double helicate an 11 K wide hysteresis loop: importantly this behaviour is also shown to be reversible over three cycles (Fig. 10b). Another key component of this report was the comparison of these SCO properties with those of the analogous mononuclear Fe(II) complex, $[Fe(\mathbf{L17a})_2](PF_6)_2$, where **L17a** is a monotopic terdentate ligand with a CH_3 group in place of the ethylene linker of **L17**. $[Fe(\mathbf{L17a})_2](PF_6)_2$ undergoes a gradual SCO from LS to HS that is very similar to the first SCO step of $[Fe_2(\mathbf{L17})_2](PF_6)_4$ between 300 and 435 K, however in the mononuclear compound there is no abrupt second step (Fig. 10b green/orange data). This example clearly demonstrates the enhanced SCO properties that can be achieved by linking two Fe(II) centres together in a dinuclear complex, in this case by simply joining two SCO-active mononuclear units through an ethylene linker. The resulting dinuclear double helicate is also remarkable for the high temperature SCO which occurs ($T_{1/2}$ ↑437 and $T_{1/2}$ ↓426 K) with an 11 K thermal hysteresis loop.

In a follow-up study, Hagiwara and Hora changed the linker length in the ligand from ethylene in **L17** to propylene in **L18**, and assembled the second example of an SCO-active double helicate, $[Fe_2(\mathbf{L18})_2](AsF_6)_4{\cdot}5H_2O{\cdot}MeCN$.[77] The change in linker from ethylene (**L17**) to propylene (**L18**) has changed the Fe–Fe distance from 7.85 to 10.87 Å (Table 5). This new double helicate is also [LS–LS] at 300 K, but above room temperature it undergoes an abrupt SCO to [HS–HS] with a remarkably wide hysteresis loop of 84 *K* ($T_{1/2}$↑ = 485 K, $T_{1/2}$↓ = 401 K). But in this case, upon further cycling in the SQUID, the SCO becomes more gradual and the hysteresis loop becomes narrower, due to lattice solvent loss and/or loss of crystallinity at high temperatures – once again highlighting the sensitivity of polynuclear SCO compounds to crystal packing and solvent content.

The use of these bis-terdentate ligands (Chart 3) results in higher $T_{1/2}$ values and less distorted Fe(II) centres in the resulting doubly-stranded helicates (43–48°, Table 5), than in the triply-stranded helicates (54–159°, Tables 2–4) formed using bis-bidentate ligands (Chart 2).

Dinuclear Fe_2L_2: PMRT and related ligands

Grouped together here are a range of bis-terdentate ligands, generated since the first SCO-active complex of such a **PMRT**-type

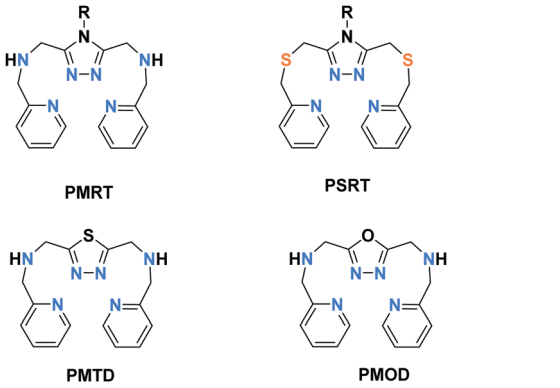

Chart 4 Bis-terdentate **PMRT** and **PSRT** (which vary in the choice of **R**, including **PMAT** where **R** = NH_2) and **PMTD** and **PMOD** ligands.

ligand was reported in 2005,[10] that provide an N^1N^2-bridge (of a five-membered heterocycle) between the binding pockets (Chart 4) forming doubly-bridged Fe_2L_2 complexes (Fig. 2, **2B**).

Of these ligands (Chart 4), the bis-terdentate 4-substituted-3,5-bis{[(2-pyridylmethyl)-amino]methyl}-4*H*-1,2,4-triazole ligands (**PMRT**, Chart 4)[10,78–82] have been widely studied within the present authors group since we first reported them in 2005.[10,78] The bis-terdentate ligand scaffold is strongly predisposed to forming dinuclear complexes. Key features include: two **PMRT** ligands provide all 12 N donors to the two octahedral metal ions, and double triazole bridges between them, and the **R** group can be widely varied (Fig. 2, **2B**). The $[Fe^{II}_2(\mathbf{PMAT})_2](BF_4)_4{\cdot}$DMF (**PMRT** with **R** = NH_2) complex undergoes an abrupt half-SCO at 224 K. The half SCO was determined to be to a localised [HS–LS] state,[10] rather than a 50 : 50 mixture of complexes in the [HS–HS] and [LS–LS] states,[83] by X-ray crystallography. The LS Fe(II) centre has a more regular octahedral coordination sphere, and hence a smaller octahedral distortion parameter, Σ, as well as shorter metal–ligand bond lengths (Fig. 11 and Table 6). This was the first report of a crystal structure of a localised mixed spin state dinuclear complex.[10] The localised mixed spin state was later further confirmed by standard Mössbauer spectroscopy, as the HS ion in the [HS–LS] state gave a distinct signal to that of the HS ions in the [HS–HS] state – the first time such a distinction had been made for a dinuclear complex without the use of an applied field.[79]

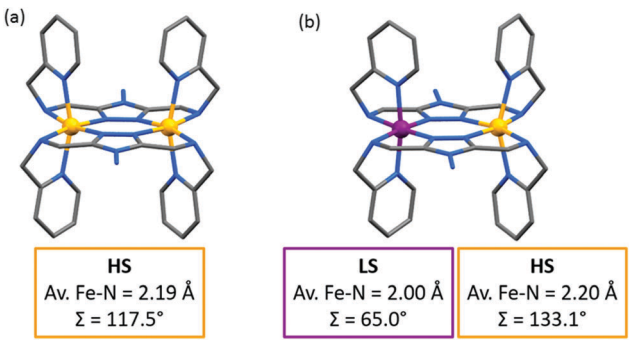

Fig. 11 (a) The [HS–HS] 298 K structure and (b) [HS–LS] 123 K structure of $[Fe^{II}_2(\mathbf{PMAT})_2](BF_4)_4{\cdot}$DMF. Structures redrawn from CCDC data.[10]

Variation of the N^4 substituent, **R**, to give other **PMRT** ligands was shown to greatly affect the SCO properties of the resulting dinuclear iron(II) complexes, $[Fe^{II}_2(\mathbf{PMRT})_2]X_4$, despite **R** being physically and electronically (when **R** is a ring it is usually almost at right angles to the triazole, switching off any possible resonance effects) remote from the donor atoms (Fig. 12).[84]

When the **R** group of **PMRT** was the 4-(*tert*-butyl)phenyl group, and specifically only for the solvatomorph $[Fe^{II}_2(\mathbf{PM^{t\text{-}Bu}PhT})_2](BF_4)_4{\cdot}3\frac{1}{2}H_2O$, an abrupt half SCO was observed with a wide thermal hysteresis loop of 22 K – at the time a record equalling hysteresis loop width for a dinuclear complex.[85] Hysteresis loops are a kinetic phenomenon so typically become narrower with a decreasing rate of change of temperature,[6] ultimately closing entirely (but potentially only after a very long time). However, remarkably, upon decreasing the temperature scan rate of the SQUID measurements on $[Fe^{II}_2(\mathbf{PM^{t\text{-}Bu}PhT})_2](BF_4)_4{\cdot}3\frac{1}{2}H_2O$ only the cooling mode narrows, while the $T_{1/2}$ of the warming mode is unchanged (Fig. 13).

The family of dinuclear iron(II) complexes of **PMRT** has revealed many interesting SCO features, with highlights including the first example of a localised [HS–LS] state to be identified by X-ray crystallography (Fig. 11) and Mössbauer spectroscopy (no applied field), and an example of unique thermal hysteresis behaviour (Fig. 12). However, in no case could the second potential SCO event, to the [LS–LS] state, be accessed, most probably because of the steric restraint of having all twelve donors to the two iron(II) centres, and two N^1N^2-triazole bridges between them, provided by just two ligands. These features lead to a significantly increased distortion at the HS centre in the [HS–LS] state, over that in the [HS–HS] state, which stabilises the mixed spin state and prevents the second HS centre from undergoing SCO (Table 6). Indeed, even under the immense pressure of 1.03 GPa and at the extremely low temperature of 4 K, the [LS–LS] state was inaccessible for $[Fe^{II}_2(\mathbf{PMAT})_2](BF_4)_4{\cdot}$DMF.[82] It is clear that the very constraining **PMRT** ligand family is extremely good at communicating the structural effects that SCO from HS to LS at the first metal ion induces, to the second metal ion such that it becomes even more distorted away from octahedral and therefore remains HS (Table 6).

The [LS–LS] state was recently accessed by changing the amino linkages to the pyridine side-arms of **PMRT** to thioether linkages in the **PSRT** family (Chart 4).[86] This change resulted in a more flexible ligand framework, due to longer C–S bonds compared to C–N bonds. In the corresponding $[Fe_2(\mathbf{PSRT})_2](BF_4)_4$ complexes (Fig. 14a), not only was SCO retained upon changing from the N_6 donor sphere provided by the **PMRT** family to N_4S_2, but, for the first time in complexes of this kind, all three of the possible spin states – [HS–HS], [HS–LS] and [LS–LS] – were accessible.

The complex $[Fe_2(\mathbf{PSPhT})_2](BF_4)_4$ in particular had interesting SCO properties, undergoing a multistep [HS–HS] → [HS–LS] → [LS–LS] transition (Fig. 14b). Unfortunately, the $[Fe_2(\mathbf{PSRT})_2](BF_4)_4$ complexes are only SCO active after MeCN solvent loss, which is associated with a loss of crystallinity, and no structural observations of the multistep SCO could be made. From the [HS–HS]

Table 6 Selected parameters for SCO-active doubly-bridged dinuclear Fe(II) complexes (Fig. 2, **2B**) of **PMRT**-type ligands (Chart 4). LS centres in italics

	T (K)	Σ (°)	Fe–Fe (Å)	Spin state	$T_{1/2}$ (K)	Lit.
$[Fe^{II}_2(\mathbf{PMAT})_3](BF_4)_4\cdot DMF$	123	*65*, 133	4.212	LS–HS	224	10
	298	117	4.296	2HS		
$[Fe^{II}_2(\mathbf{PMBzT})_2](BF_4)_4\cdot 2CH_3CN$	91	99	4.178	2HS	147	84
$[Fe^{II}_2(\mathbf{PMPh^{tBu}T})_2](BF_4)_4\cdot 3CH_3CN\cdot 0.5Et_2O$	91	118	4.262	2HS	↑217 ↓194	85
$[Fe^{II}_2(\mathbf{PSPhT})_2](BF_4)_4\cdot 2MeCN\cdot H_2O$	100	110	4.216	2HS	265, 210 and 87	86
$[Fe^{II}_2(\mathbf{PSPhT})_2](BF_4)_4\cdot 2.5MeCN\cdot 0.5H_2O\cdot THF$	100	105	4.231	2HS	Not stated	
$[Fe^{II}_2(\mathbf{PS^{Me}PhT})_2](BF_4)_4\cdot 2MeCN$	100	88	4.189	2LS/HS	109	
$[Fe^{II}_2(\mathbf{PMTD})_2](BF_4)_4\cdot 0.75MeOH\cdot 0.5H_2O$	173	*58*, *65*	3.946	LS–LS	Not stated	88
$[Fe^{II}_2(\mathbf{PMTD})_2](ClO_4)_4\cdot 0.75MeOH\cdot 0.5H_2O$	173	*59*, *66*	3.952	LS–LS	Not stated	
$[Fe^{II}_2(\mathbf{PMTD})_2](OTf)_4\cdot 1.5MeOH\cdot 0.5CH_2Cl_2$	173	*61*, *58*	3.948	LS–LS	Not stated	
$[Fe^{II}_2(\mathbf{PMTD})2](BF_4)_4\cdot 4DMF$	173	*59*, *60*	3.950	LS–LS	380	89
$[Fe^{II}_2(\mathbf{PMTD})2](ClO_4)_4\cdot 4DMF$	193	*59*, *60*	3.953	LS–LS	380	
$[Fe^{II}_2(\mathbf{PMOD})_2](ClO_4)_4\cdot 4MeCN$	193	121	4.402	2HS	150	90
	100	*70*, 137	4.326	LS–HS		
$[Fe^{II}_2(\mathbf{PMOD})_2](BF_4)_4\cdot 2MeCN$	173	126	4.378	2HS	Not stated	
$[Fe^{II}_2(\mathbf{PMOD})_2](OTf)_4\cdot 2MeCN$	193	125	4.361	2HS	150	

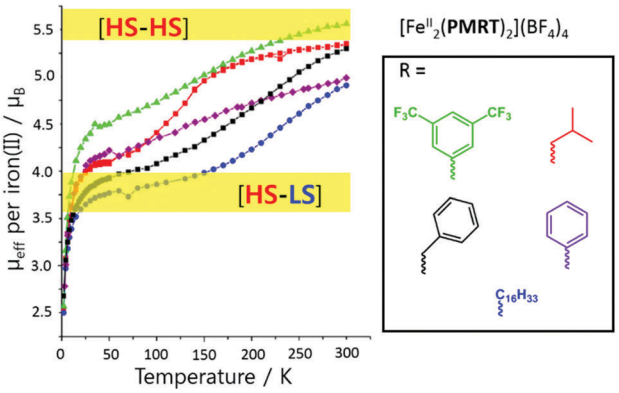

Fig. 12 Effective magnetic moment per iron(II) centre *vs.* T for the SCO-active complexes $[Fe^{II}_2(\mathbf{PMRT})_2](BF_4)_4$, where **R** is one of the five moieties shown in the box. Figure adapted with permission from ref. 84. Copyright 2013 ACS.

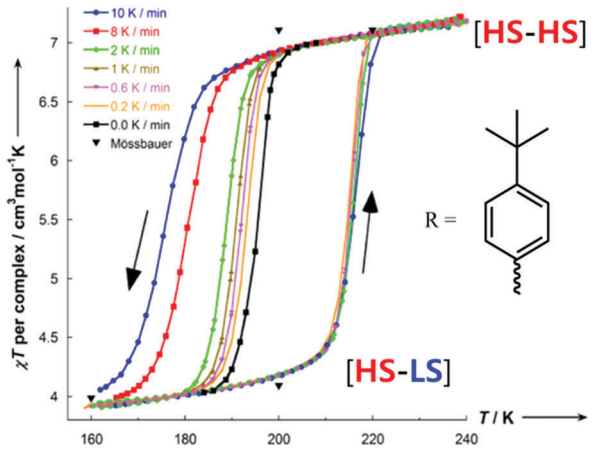

Fig. 13 Scan rate dependence of the thermal hysteresis loop of $[Fe^{II}_2(\mathbf{PM^{t\text{-}Bu}PhT})_2](BF_4)_4\cdot 3\frac{1}{2}H_2O$. Figure adapted with permission from ref. 85. Copyright 2014 ACS.

structures (MeCN solvated), however, one can observe the enhanced flexibility of these **PSRT** dinuclear systems, over the

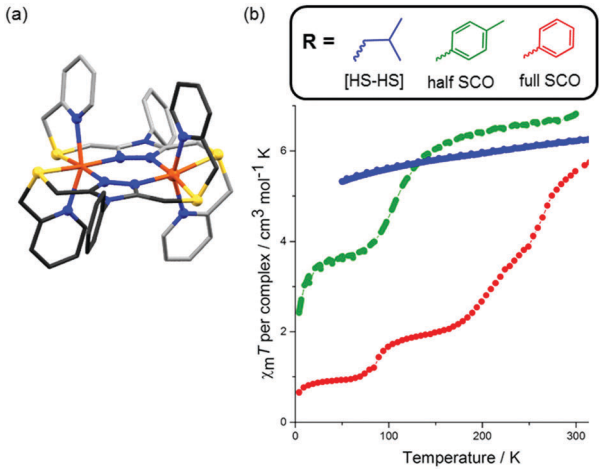

Fig. 14 (a) Structure of the complex cation of $[Fe_2(\mathbf{PSPhT})_2](BF_4)_4$, with carbons shaded dark/light grey on opposite ligands to highlight the *trans*-axial binding mode. (b) Solid state SCO of $[Fe_2(\mathbf{PSRT})_2](BF_4)_4$ complexes with varying **R**. Structure redrawn from CCDC data.[86] (b) Adapted with permission from ref. 86. Copyright 2016 ACS.

PMRT analogues, and this is believed to facilitate the observed complete [HS–HS] → [LS–LS] SCO. The Fe–N bond lengths in the **PSRT** structures are completely within the range expected for HS Fe(II) (Table 6). Furthermore, while **PMRT** ligands have always been observed to bind two Fe(II) metals in a bis-terdentate fashion and in a *cis*-axial mode (both pyridine arms up, but note that an alternative binding mode has been seen for an Fe(III) oxo product[87]), the more flexible **PSRT** ligands were observed to bind in bis-terdentate fashion and either a *cis*-axial mode or *trans*-axial mode (pyridine arms up/down, Fig. 14a). In addition to solid state SCO-activity, the $[Fe_2(\mathbf{PSRT})_2](BF_4)_4$ complexes exhibit SCO in MeCN solution, induced by both temperature and pressure, with more electron donating **R** groups predictably favouring LS more.[16,86]

The Rentschler group has reported an interesting family of **PMRT**-like complexes of a thiadiazole analogue of **PMRT**,

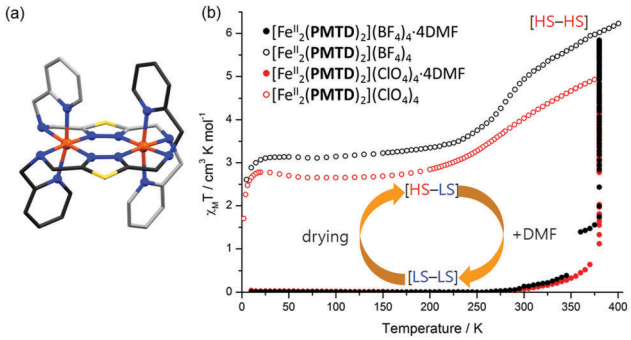

Fig. 15 (a) Structure of the cation of [Fe$^{II}_2$(**PMTD**)$_2$]X$_4$, with carbons shaded dark/light grey on opposite ligands to highlight the *trans*-axial binding mode. (b) [Fe$^{II}_2$(**PMTD**)$_2$]X$_4$·solvent $\chi_M T$ *vs.* T data sets showing the DMF sensing ability of the complexes. Structure redrawn from CCDC data.[88] (b) Adapted with permission from ref. 89. Copyright 2016 ACS.

2,5-bis[(2-pyridylmethyl)amino]methyl-1,3,4-thiadiazole (**PMTD**, Chart 4). The bis-terdentate **PMTD** ligand differs from **PMRT** ligands in that there is a non-coordinating sulphur atom in place of the non-coordinating N^4-**R** moiety of **PMRT**. It was shown to produce [Fe$^{II}_2$(**PMTD**)$_2$]X$_4$ complexes with the *trans*-axial binding mode (Fig. 15a, like the thioether **PSRT** systems), revealing more flexibility than in the analogous **PMRT** complexes (always *cis*-axial mode), and thus giving access to the fully [LS–LS] state.

The impact of the larger S heteroatom in the central five membered ring of **PMTD** (over the N atom in **PMRT**) on the overall flexibility can also be seen in the angle at which the amino side arms protrude from the thiadiazole/triazole, with N_{azole}–N_{azole}–N_{amino} angles averaging 176.04° for LS **PMTD** complexes and 172.30° for [HS–LS] [Fe$_2$(**PMAT**)$_2$](BF$_4$)$_4$. Indeed, all three [Fe$^{II}_2$(**PMTD**)$_2$]X$_4$ complexes highly favour the [LS–LS] state and undergo a gradual SCO starting above 250 K, not reaching the [HS–LS] state (or the [HS–HS] state) at the limit of the measurement, 380 K.[88] In 2016, the DMF solvates of [Fe$^{II}_2$(**PMTD**)$_2$](BF$_4$)$_4$ and [Fe$^{II}_2$(**PMTD**)$_2$](ClO$_4$)$_4$, which are both [LS–LS], were shown to undergo a transition to the [HS–HS] state upon thermal desolvation of the DMF molecules, and to subsequently undergo a half-SCO to the [HS–LS] state upon cooling (Fig. 15b and Table 6).[89]

The Rentschler group further investigated the effect of changing the non-coordinated-heteroatom in the five-membered ring, this time to an oxygen atom, generating the oxadiazole analogue, 2,5-bis{[(2-pyridylmethyl)amino]-methyl}-1,3,4-oxadiazole (**PMOD**, Chart 4). The more electronegative oxygen (*cf.* the sulphur atom of **PMTD**) was anticipated to decrease the ligand field strength at the N donor atoms of the heterocycle, and indeed the HS state is stabilised in comparison to the thiadiazole **PMTD** complexes: all three [Fe$_2$(**PMOD**)$_2$]X$_4$ (X = ClO_4^-, BF_4^-, or $CF_3SO_3^-$) complexes are [HS–HS] at room temperature. While the X = BF_4^- complex remains HS to low temperatures, the X = ClO_4^- and X = $CF_3SO_3^-$ complexes undergo abrupt [HS–HS] to [HS–LS] SCO centred about 150 K, with a 26 K wide hysteresis loop for [Fe$_2$(**PMOD**)$_2$](CF$_3$SO$_3$)$_4$. The [LS–LS] state was inaccessible due to steric constraints imposed by the rigid ligand: the smaller oxygen heteroatom tightens the angle of the

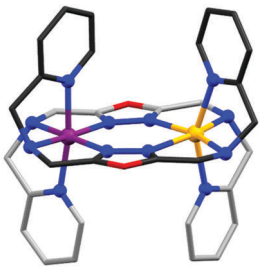

Fig. 16 Structure of the cation of [Fe$^{II}_2$(**PMOD**)$_2$]X$_4$, (yellow HS and purple LS Fe^{II} centre) with carbons shaded dark/light grey on opposite ligands to highlight the *cis*-axial binding mode.[90] Structure redrawn from CCDC data.

amino side arms relative to that in **PMTD**, as seen by a reduction of the N_{azole}–N_{azole}–N_{amino} angle from 177 to 168°, and by the *cis*-axial binding mode (Fig. 16). As was seen with the **PMRT** ligands, the transition to the [HS–LS] state for [Fe$_2$(**PMOD**)$_2$](ClO$_4$)$_4$ is associated with an increase in octahedral distortion parameter at the residual HS Fe(II) centre ([HS–HS] @ 193 K, Σ_{HS} = 121°; [HS–LS] @ 100 K, Σ_{HS} = 137° Fig. 16 yellow, Σ_{LS} = 70° Fig. 16 purple; Table 6). Crystal packing appears to have a large influence on the SCO behaviour. A hydrogen bonding network for one of the compounds, linking amino NH groups on neighbouring [Fe$_2$(**PMOD**)$_2$]$^{4+}$ cations *via* $CF_3SO_3^-$ counteranions, infers high cooperativity and results in the hysteresis loop. Also, all three compounds contain two or four solvent MeCN molecules, and although no significant interactions to the cations are obvious, SCO is lost upon desolvation.

Dinuclear Fe$_2$L$_2$ formed by assorted other ligands

Further examples of dinuclear Fe$_2$L$_2$ type complexes (Fig. 2, **2B**) are formed by the diverse family of ligands **L19–L21** (Chart 5).

Murray, Kepert and co-workers have reported a pyridyl rich ligand, **L19** (Chart 5), which binds in a bis-bidentate manner, forming a SCO active dinuclear Fe$_2$L$_2$ complex, [Fe$_2$(**L19**)$_2$(NCS)$_4$]·4CH$_2$Cl$_2$ (Fig. 17a).[91] It undergoes a two-step SCO with all three spin states accessed: [HS–HS], [HS–LS], and [LS–LS]. The plateaus occurred at 110 and 140 K with $T_{1/2}$ = 80 and 180 K (Fig. 17b, a circle). The authors traced the magnetic behaviour with Σ angle at different temperatures (Table S1, ESI†). At 25 K both Fe(II) centres

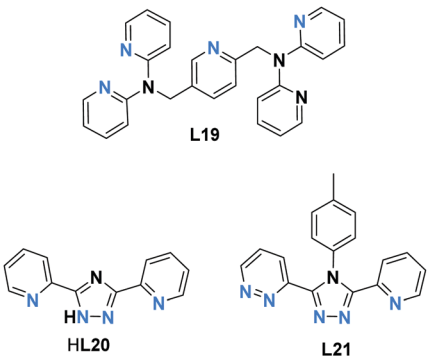

Chart 5 Assorted other ligands, **L19–L21**, forming SCO-active Fe$_2$L$_2$ type dinuclear Fe(II) complexes (Fig. 2, **2B**).

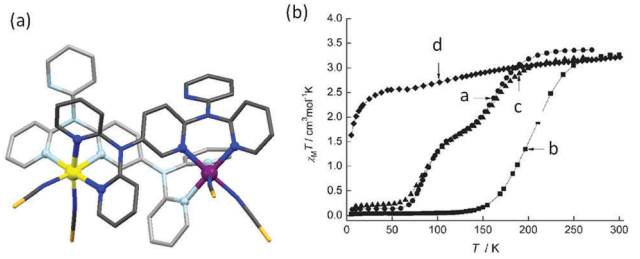

Fig. 17 (a) $[Fe^{II}_2(\mathbf{L19})_2NCS_4]$ structure, with carbons shaded dark/light grey. (b) Plots of χ_mT per Fe^{II} *vs.* *T*, for complex $[Fe_2(\mathbf{L19})_2(NCS)_4]\cdot x CH_2Cl_2$ (a) $x = 4$ (circle), (b) $x = 1$ (square) (c) re-solvated, $x = 4$ (triangle) (d) $x = 1$ (rhombus). Structure redrawn from CCDC data and (b) adapted from ref. 91 with permission. Copyright 2006 John Wiley and Sons.

were in the LS state with $\Sigma = 28.4^\circ$ and 35.2°. The intermediate [HS–LS] state observed at 123 K has Fe_{LS} $\Sigma = 27.7^\circ$ (Fig. 17a, purple) and Fe_{HS} $\Sigma = 45.9^\circ$ (Fig. 17a, yellow). Furthermore, heating from 123 K to 250 K the geometry around Fe2 is slightly changed from 45.9° to 46.7°, Fe1 = 41.8°. The partially de-solvated compound underwent a one-step SCO with increased transition temperature, $T_{1/2}$ of 200 K (Fig. 17b, b square). Furthermore, immersion of partially de-solvated compound into dichloromethane reverted the two-step SCO (Fig. 17b, c triangle). The fully de-solvated compound lost its SCO nature and remained HS all over the temperature range, $\chi_mT = 3.15$ cm^3 K mol^{-1} at 300 K (Fig. 17b, d rhombus).

Murray and co-workers also reported, in 2013, a triazolate bridged dinuclear complex of anionic **L20**, Chart 5 (Fig. 18a). Single crystal and powder forms of $[Fe_2(\mathbf{L20})_2(NCBH_3)_2(py)_2]$ showed distinctly different degrees of thermally induced SCO behaviour with different $T_{1/2}$ values. The powder sample showed a two-step complete SCO at $T_{1/2}$ = 194 and 151 K (Fig. 18b) whereas the crystal form showed an abrupt half step SCO at $T_{1/2}$ 102 K (Fig. 18c).[92]

Brooker and co-workers reported another kind of Fe_2L_2 type SCO–Fe(II) complex in 2016, by employing **L21** (Chart 5).[93] The resulting dark red dinuclear complex $[Fe_2(\mathbf{L21})_2(MeCN)_4](BF_4)_4$·2MeCN was shown by a crystal structure determination to be [LS–LS] at 100 K (Fig. 19a). It underwent a gradual SCO with a 13 K wide thermal hysteresis loop, at $T_{1/2}\downarrow$ = 356 K and $T_{1/2}\uparrow$ = 369 K (Fig. 19b, maroon curve). The χ_mT was 2.45 emu mol^{-1} K at 400 K, indicating about 80% conversion from [LS–LS] to [HS–HS]. Guest exchange, by reversible SCSC transformations, gave two other complexes, orange $[Fe_2(\mathbf{L21})_2(EtOH)_4](BF_4)_4$ and yellow polymer $\{[Fe_2(\mathbf{L21})_2(H_2O)_4](BF_4)_4\}_\infty$, both of which were [HS–HS] at all temperatures 50–400 K (Fig. 19b, orange and yellow curves, respectively).

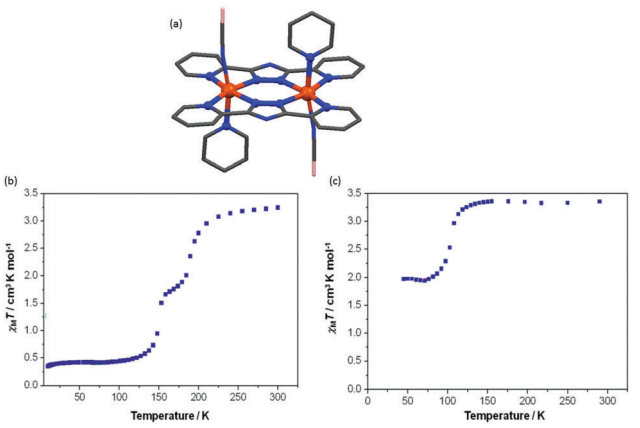

Fig. 18 (a) The crystal structure of $[Fe_2(\mathbf{L20})_2(NCBH_3)_2(py)_2]$. (b) χ_mT *vs.* *T* plot for powder sample and (c) crystal form. Structure redrawn from CCDC data. (b and c) Adapted from reference, with permission.[92] Copyright 2016 John Wiley and Sons.

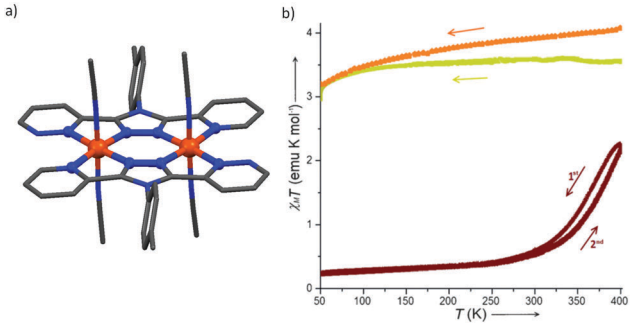

Fig. 19 Data for $[Fe_2(\mathbf{L21})_2(MeCN)_4](BF_4)_4$·2MeCN: (a) structure of the tetracation. (b) χ_mT (per Fe) *vs.* *T* plot (maroon). Structure redrawn from CCDC data and (b) adapted from reference, with permission.[93] Copyright 2013 John Wiley and Sons.

Dinuclear singly N-ligand linked Fe_2L

Grouped together in this section are the Fe_2L dinuclear complexes in which the two Fe(II) centres are linked by a single ligand L that provides some, or all, of the N-donors (Fig. 2, **2C**). The ligands employed vary considerably, ranging from bis-monodentate, to bis-bi-, bis-tri-, bis-tetra- and bis-hexa-dentate (Chart 6), but all give rise to dinuclear M_2L complexes of type **2C** (Fig. 2).

In 2015, Meyer and co-workers reported a dinuclear Fe_2L complex (Fig. 2, **2C**) of a bis-terdentate pyrazolate ligand, H**L22** (Chart 6).[94] H**L22** is deprotonated and provides a single pyrazolate bridge between the two Fe(II) centres as well as meridionally coordinated N_2P donors to each of them, in $[Fe_2$ $\mathbf{L22}(OTf)_3(CH_3CN)]$ (Fig. 20a). In addition to the bridging pyrazolate, the Fe(II) centres are also bridged by two triflate anions, and the octahedral geometry of HS Fe1 is completed by a terminal triflate (O_3N_2P), and that of Fe2 by a MeCN ligand (O_2N_3P). The magnetic behaviour of this complex was studied in both solid and solution (Fig. 20b). In the solid state it remains fully high spin, due to the O-donors. In contrast, in MeCN solution, the complex exchanges the triflate anions for MeCN solvent molecules, becoming N_5P-coordinated and enabling it to undergo a reversible and complete thermally induced SCO (Fig. 20b).[94]

Sato and co-workers[95] studied the pyrazine-bridged Fe_2L dinuclear complexes (Fig. 2, **2C**) $[Fe_2\mathbf{L}(NCS)_4]\cdot DMF\cdot 2H_2O$, of the bis-tetradentate pyrazine ligands **L** = **L23**, **L24** (Chart 6). The dinuclear complex of the 2,5-substituted pyrazine ligand **L23**, $[Fe_2\mathbf{L23}(NCS)_4]\cdot DMF\cdot 2H_2O$, underwent a one-step SCO at around 180 K (Fig. 21, red circles). After being heated to 400 K, desolvated

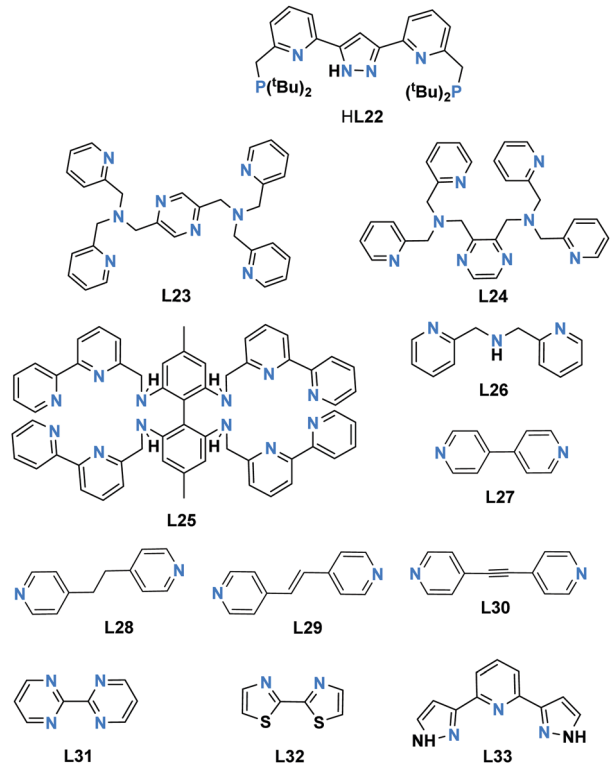

Chart 6 Ligands used to link two Fe(II) ions forming SCO-active singly-ligand linked dinuclear M_2L complexes (Fig. 2, **2C**).

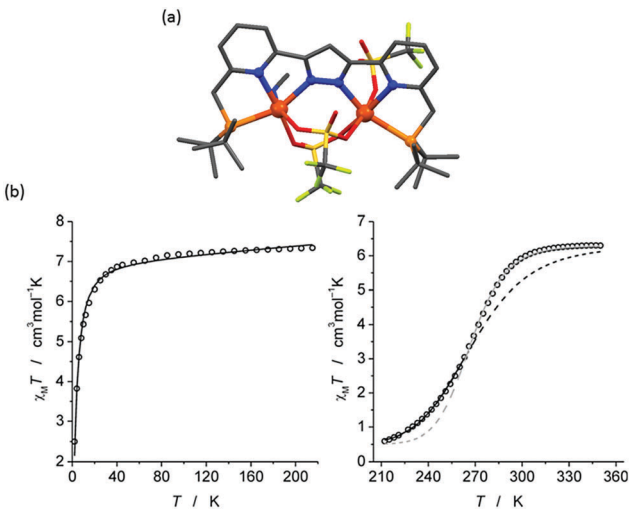

Fig. 20 (a) The solid state structure of $[Fe_2\mathbf{L22}(OTf)_3(CH_3CN)]$. (b) χ_mT *vs.* *T* plot in the solid state (left) and MeCN solution (right). Structure redrawn from CCDC data. (b) Reproduced from reference, with permission.[94] Copyright 2015 John Wiley and Sons.

$[Fe_2\mathbf{L23}(NCS)_4]$ showed a different SCO curve, with an abrupt transition ($T_{1/2}\uparrow$ = 189, $T_{1/2}\downarrow$ = 184 K) and 5 K wide hysteresis loop (Fig. 21, inset). In the case of the 2,3-substituted pyrazine ligand **L24**, the resulting complex displayed a gradual two step SCO, [HS–HS] ↔ [LS–HS] ↔ [LS–LS].[95] At 300 K, χ_mT value is 5.58 cm^3 K mol^{-1}, consistent with the [HS–HS] state, and decreases gradually to 0.71 cm^3 K mol^{-1} at 70 K, consistent

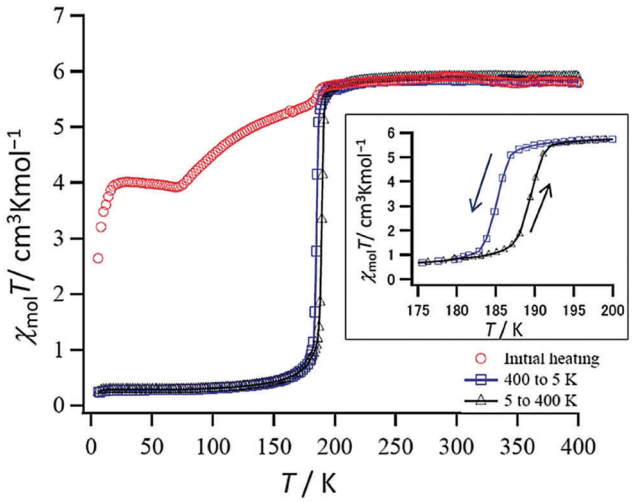

Fig. 21 $X_{mol}T$ *vs.* *T* for $[Fe_2\mathbf{L23}(NCS)_4]\cdot DMF\cdot 2H_2O$ (initial heating: red circles; cooling cycle: blue squares, heating cycles: black triangles (on heated sample)). Figure reproduced from ref. 95. Copyright 2013 John Wiley and Sons.

with the [LS–LS] state, however with a change in slope occurring at approximately χ_mT = 3 cm^3 K mol^{-1}, 185 K, indicating that the Fe(II) centres undergo SCO at differing temperatures. The LIESST studies on this pair of complexes gave pairs of thermal transition temperature ($T_{1/2}$) and photo-induced transition temperature (T_{LIESST}) values for desolvated $[Fe_2\mathbf{L23}(NCS)_4]$ (192, 70 K) and for $[Fe_2\mathbf{L24}(NCS)_4]\cdot DMF\cdot 2H_2O$ (210 and 56 K; 130 and 71 K). These fall close to the T_0 = 120 K line of the correlation, $T_{LIESST} = T_0 - 0.3T_{1/2}$, earlier identified by Létard and co-workers.[96]

In 2013, Petzold and co-workers reported a dinuclear Fe_2L complex of a bis-hexadentate, biphenyl-linked, **L25** (Chart 6), in which the two Fe(II) centres are linked by this single ligand.[97] Remarkably **L25** provides all twelve N-donors to the two octahedral Fe(II) centres in $[Fe_2(\mathbf{L25})](BPh_4)_4$. The structure determination shows the complex to be fully LS at 153 K (Fig. 22a) whereas mononuclear $[Fe(\mathbf{L25})](BPh_4)_2$ was paramagnetic at room temperature. In MeCN solution there is a very gradual, partial SCO towards HS as the temperature is raised from 298 (25 °C) to 348 K (75 °C), with the fraction HS rising from 0.05 to 0.15 (Fig. 22b).

Some of the 4,4′-bi-pyridine-like bridged SCO-active Fe_2L complexes were covered in our previous review,[35] but for completeness are also included here. Matouzenko and co-workers studied a series of dinuclear Fe_2L complexes, $[\{Fe(\mathbf{L26})(NCX)_2\}_2(\mathbf{L})]\cdot n$MeOH (X = S and BH_3; **L** = **L27–L30**, Chart 6) varying the length of the bipyridyl-like bridges **L**, between the Fe(II) centres (Fig. 2, **2C**), and employing **L26** capping ligands (Chart 6). They first reported this kind of complex in 2009, with X = S and **L27**.[98]

Then in 2011 they replaced the **L27** bridge by **L29** (Chart 6), retaining X = S, generating three forms of $[\{Fe(\mathbf{L26})(NCS)_2\}_2(\mathbf{L29})]\cdot n$MeOH, a pair of solvent-free polymorphs (n = 0) and a solvatomorph (n = 2), which displayed different SCO behaviours. The two solvent-free polymorphs were dark vinous (red-wine coloured) prismatic *versus* brown crystals. The crystal structures

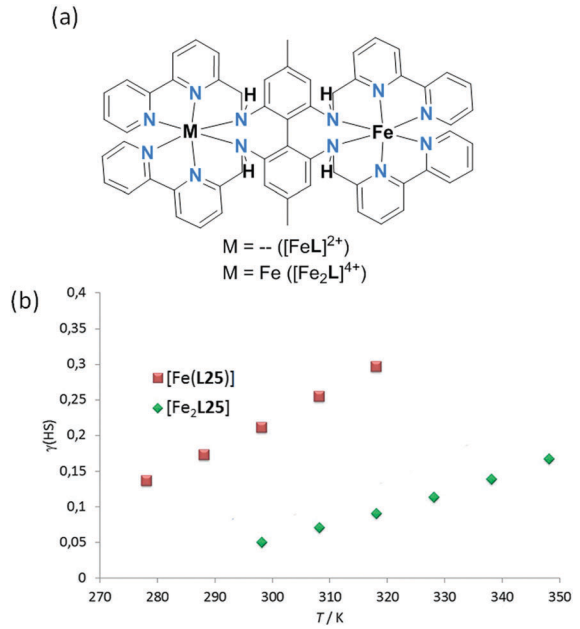

Fig. 22 (a) Binding sites in mononuclear and dinuclear Fe(II) complexes of hexadentate **L25**; dinuclear singly-ligand linked (Fig. 2, **2C**). (b) Evans measurements on mononuclear $[Fe(\mathbf{L25})](BPh_4)_2$ and dinuclear $[Fe_2(\mathbf{L25})](BPh_4)_4$. Figure adapted from reference, with permission.[97] Copyright 2013 John Wiley and Sons.

of the vinous polymorph at 300 K, 183 K and 90 K, revealed [HS–HS], localised [HS–LS], and [LS–LS] spin states, respectively. This is consistent with the occurrence of a two-step SCO, separated by a subtle inflection point with $T = 182$ K as revealed by the magnetic study. The brown crystals remained high spin. In contrast, the red-brown crystals of the methanol solvate underwent a complete one step transition, without hysteresis, at 159 K.[99]

The following year they instead employed a **L30** bridge (Chart 6), again retaining X = S, and generating two solvatomorphs, $n = 0$ and $n = 2$ (Fig. 23a), which differed in SCO behaviour. The solvent free complex underwent a two-step SCO, with 50% spin conversion and short plateau at 145 K, with a 17 K wide hysteresis loop for the lower temperature SCO event ($T_{1/2}\downarrow = 126$ and $T_{1/2}\uparrow = 143$ K) (Fig. 23b). The methanol solvate, $[\{Fe(\mathbf{L26})(NCS)_2\}_2(\mathbf{L30})]\cdot 2MeOH$, undergoes a one-step SCO with a narrow 4 K hysteresis loop ($T_{1/2}\downarrow = 150$ and $T_{1/2}\uparrow = 154$ K; Fig. 23c).[100]

Then in 2013 they changed to using cyanoborohydride anions, generating a set of three complexes which varied in the choice of **L** (**L** = **L27**, **L28**, **L30**), $[\{Fe(\mathbf{L26})(NCBH_3)_2\}_2(\mathbf{L})]$. The complex with an **L** = **L27** bridge showed abrupt two step SCO with an inflection point at 210 K whereas with the complexes with an **L** = **L28** or **L30** bridge showed gradual one step transitions with $T_{1/2}$ of 241 and 290 K, respectively.[101]

Pressure induced SCO is less commonly studied. A key early study carried out on bipymidine-bridged SCO-active Fe_2L complexes $\{[Fe(\mathbf{L})(NCE)_2]_2\mathbf{L31}\}$, where E = S or Se and the capping ligands were **L** = **L31** or **L32** (Chart 6), was reported in 2001 by Gutlich, Real and co-workers (Fig. 24).[102]

At ambient pressure $\{[Fe(\mathbf{L31})(NCS)_2]_2\mathbf{L31}\}$ was paramagnetic 4–300 K (Fig. 24a). In contrast, at 8.9 kbar it showed incomplete one-step SCO behaviour, $T_{1/2} \approx 150$ K. At ambient

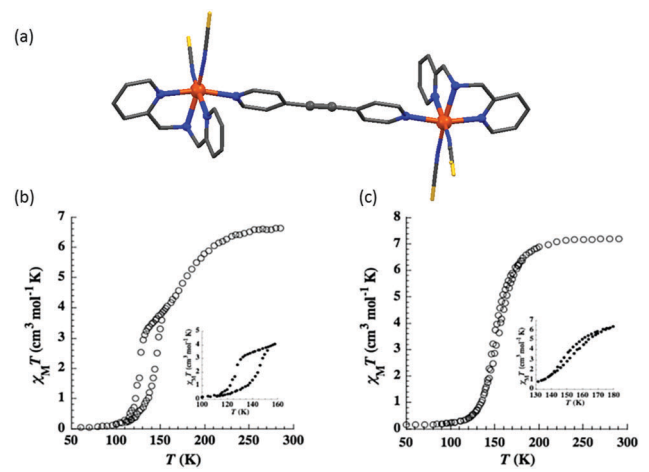

Fig. 23 (a) Crystal structure of $[\{Fe(\mathbf{L26})(NCS)_2\}_2(\mathbf{L30})]$. (b) $\chi_M T$ *vs.* T plot for $n = 0$ and (c) $n = 2$. Structure redrawn from CCDC data. (b and c) Reproduced with permission.[100] Copyright 2012 John Wiley and Sons.

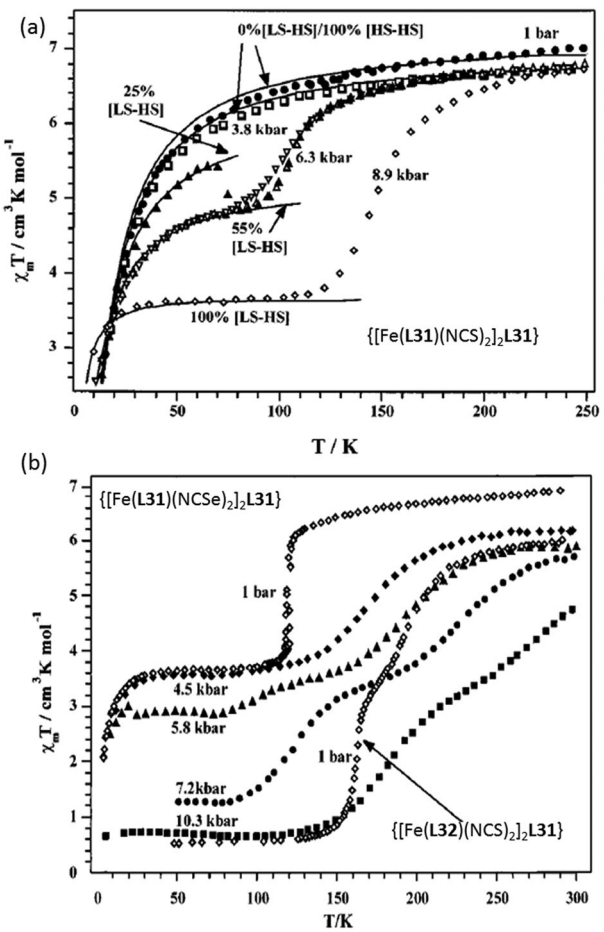

Fig. 24 (a) $\chi_m T$ *vs.* T plot of $[Fe(\mathbf{L31})(NCS)_2]_2\mathbf{L31}$ and (b) $[Fe(\mathbf{L31})(NCSe)_2]_2\mathbf{L31}$ and $[Fe(\mathbf{L32})(NCS)_2]_2\mathbf{L31}$ at various pressures. (a and b) Adapted with permission from ref. 102. Copyright 2001 ACS.

pressure (1 bar) the X = Se analogue, {[Fe(**L31**)(NCSe)$_2$]$_2$**L31**}, undergoes a 50% spin transition at $T_{1/2}$ = 120 K (Fig. 24b).[102] The complex featuring bis-thiazole capping ligands (**L32**, Chart 6), {[Fe(**L32**)(NCS)$_2$]$_2$**L31**}, underwent an almost complete two step SCO at ambient pressure (Fig. 24b).

In 2012, Molnár, Guionneau and co-workers reported the effect of pressure on the SCO curve of the 4,4′-bipyridine (**L27**, Chart 6) bridged Fe$_2$L complex, [{Fe(**L33**)(NCS)$_2$}$_2$(**L27**)]·2MeOH, which features **L33** capping ligands (Chart 6).[103] This complex undergoes thermally and photo-induced incomplete SCO, which was ascribed to a purely structural phase transition and only partial conversion to LS at low temperature.[104] But under the influence of high pressure, this complex showed no crystallographic phase transition. High pressure X-ray diffraction and Raman spectroscopic studies showed that a fully LS state is realised at low temperature, and that SCO is very gradual at pressures between 7 and 25 kbar.[103]

Assorted anion bridged dinuclear complexes

Non-heterocyclic anion bridged (Chart 7) SCO-active dinuclear Fe(II) complexes (Fig. 2, **2D**) are rarely reported, with only four cases in the literature, all of which employ polydentate N-donor capping ligands (Chart 8).

In the first case, dicyanamide (**dca**, Chart 7) acts as the anionic bridge between the two Fe(II) centres, with the N$_6$ coordination spheres completed by **L34** capping ligands (Chart 8).[105] In the second case, cyanocarbanions (**A1**, Chart 7) doubly bridge the two Fe(II) centres, with the N$_6$ coordination spheres completed by **L35** and **L36** capping ligands (Chart 8), giving a neutral complex.[106] In the third case, **NCS** anions doubly bridge the Fe(II) centres with N$_5$S coordination environments and **L37** capping ligands (Chart 8).[107] The fourth example features a diiminoquinonoid-bridges (**A2–A5**, Chart 7) with **L35** capping ligands (Chart 8).[108]

Real and co-workers reported the first example, a dicyanamide bridged Fe(II) SCO-active dinuclear complex, in 2005,[105] [Fe$_2$**L34**$_2$(**dca**)](PF$_6$)$_3$·nH$_2$O (n = 1 and 0). When n = 1 it remains HS with a constant $\chi_m T$ value of 6.7 cm^3 K mol^{-1} from 350 K to 50 K. In contrast, n = 0 [Fe$_2$**L34**$_2$(**dca**)](PF$_6$)$_3$ showed a two-step spin transition: at 400 K, $\chi_m T$ = 7.0 cm^3 K mol^{-1} indicating all iron centres are HS, then $\chi_m T$ decreased gradually to 3.65 cm^3 K mol^{-1} at 250 K with a broad plateau from 285–208 K, then in a second step it decreased gradually to 0.21 cm^3 K mol^{-1} at 50 K. This SCO response was attributed to 50% spin conversion in each step. Magnetic studies in D$_6$-acetone solution showed the one-step incomplete SCO-behaviour of both solvatomorphs.[105]

In 2016, Triki and co-workers used two types of tetradentate capping ligands, **L35** and **L36** (Chart 8), to obtain a pair of **A1**-bridged complexes (**A1**, Chart 7), [Fe$_2$**L**$_2$(**A1**)$_2$]·nMeOH (n = 0.8 and 2, respectively). The small difference between these tetradentate capping ligands, **L35** and **L36** (Chart 8), leads to a large change in $T_{1/2}$ ($\Delta T_{1/2}$ > 150 K), from 365 to 180 K, respectively (Fig. 25), which they attributed to changes in crystal packing. After desolvation of this pair of complexes, the $T_{1/2}$ values were slightly different, 352 and 196 K, respectively.[106]

Harris and co-workers also employed the tetradentate capping ligand **L35**, but utilised a series of diiminoquinonoid anion bridges, **A2–A5** (Chart 7) to generate dinuclear [Fe$_2$(**L35**)$_2$(**A**)]-(B(PhCF$_3$)$_4$)$_2$, with **A2–A5**, complexes in order to systematically study the effect of varying the electronic effects of substituents on the bridge **A** on the SCO behaviour (Fig. 26a).[108] They were able to correlate $T_{1/2}$ and ΔH (the latter obtained by fitting the magnetic data to an ideal solution model) (Fig. 26b). They showed that both the $T_{1/2}$ (from 160–110 K) and ΔH (from 11.4–7.5 kJ mol^{-1}) values decreased with increasingly electron-withdrawing groups X

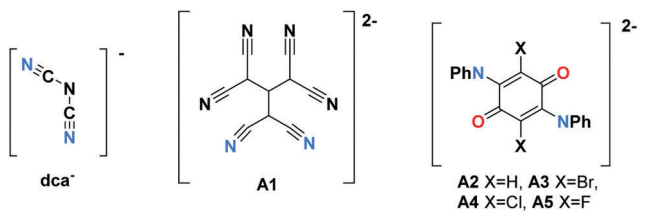

Chart 7 Anions used as bridges in SCO-active dinuclear Fe(II) complexes (Fig. 2, **2D**).

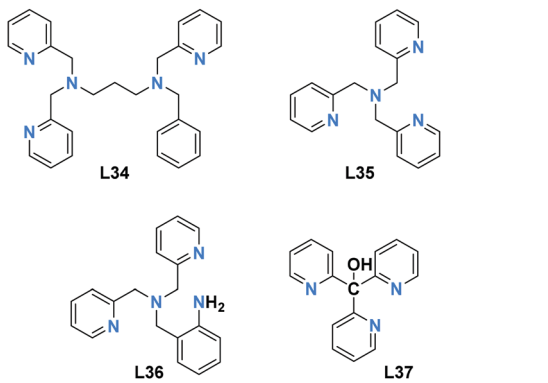

Chart 8 Capping ligands used in anion bridged SCO-active Fe(II) dinuclear complexes (Fig. 2, **2D**).

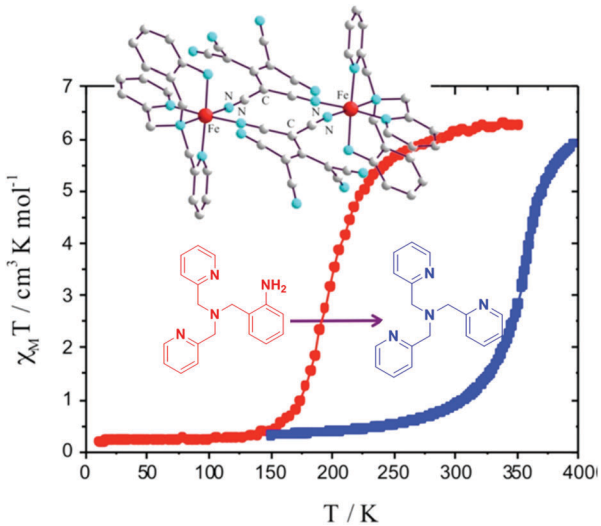

Fig. 25 Plot of $\chi_m T$ *vs.* T of desolvated [Fe$_2$**L**$_2$(**A1**)$_2$] [**L35** (blue points) and **L36** (red points)]. Figure adapted from reference with permission.[106] Copyright 2016 ACS.

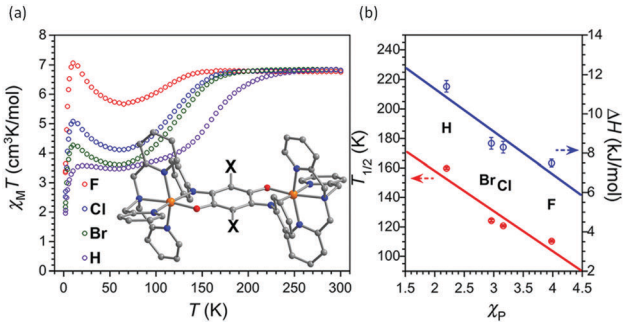

Fig. 26 (a) $\chi_m T$ *vs.* T plot of $[Fe_2(\mathbf{A})(\mathbf{L35})_2](B(PhCF_3)_4)_2$, **A2–A5**. (b) Correlation between $T_{1/2}$ (red points) and ΔH (blue points) as a function of Pauling electronegativity (χP) of the X substituent (F, Cl, Br, H). (a and b) Adapted with permission from ref. 108. Copyright 2015 ACS.

on the bridging anion **A2–A5** (–H to –Br to –Cl to –F), as measured by the Pauling electronegativity (χP).[108] The incorporation of electron withdrawing groups in **A** increases the π-back donation from the **L35** pyridyl capping ligand and stabilises the LS state, hence shifting $T_{1/2}$ towards higher temperatures.

Another example features bridging **NCS**$^-$ anions, and employs **L37** as capping ligands (Chart 8). The complex $[\{Fe(\mathbf{L37})(NCS)(\mu\text{-}\mathbf{NCS})\}_2]$ showed gradual one step SCO, [LS–LS] ↔ [HS–HS], at 207 K, with no hysteresis loop.[107]

Trinuclear: triply triazole bridged, Fe_3L_6

All of the structurally characterized SCO-active trinuclear Fe(II) complexes after 2011 are of one structural type: triply triazole-bridged (Fig. 2, **3A**). Like the dinuclear analogues, they are readily structurally characterised, in contrast to the related 1D-chain polymers. To date, 10 different N^4-substituted 1,2,4-triazoles (Chart 9) have been employed in generating these complexes. In all cases, the six R-triazole ligands provide triple N^1N^2 bridges between the central Fe(II) and each of the two terminal Fe(II) ions, resulting in an N_6 octahedral central Fe(II) ion, and providing 3N donors to each of the terminal Fe(II) ions

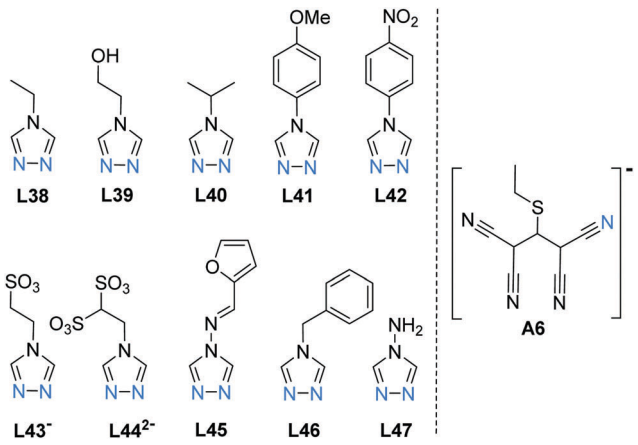

Chart 9 Ligands **L38–L47** reported in the literature to form SCO-active Fe^{II} trinuclear complexes (Fig. 2, **3A**): in all cases only the central Fe(II) site is SCO active – except for **L46** and **A6** which provide all three Fe(II) sites with SCO active N_6 coordination environments.

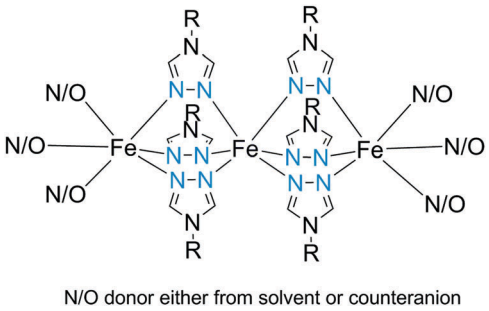

Fig. 27 Schematic representation of trinuclear triply-triazole bridged SCO-active Fe(II) complexes (Fig. 2, **3A**).

with their octahedral coordination completed by three mono-anions and/or solvent molecules (Fig. 27). Depending on coordinated or non-coordinated anions, the three Fe(II) centres are afforded either N_3O_3–N_6–N_3O_3[109–116] or N_6–N_6–N_6[117] or N_5O–N_6–N_5O[118] coordination environments. In all of these trinuclear complexes, the central Fe(II) is always N_6, being triply triazole bridged to each of the other two Fe(II) centres. Hence the central Fe(II) centre in these complexes is the only one that undergoes SCO – except in the case of $[Fe_3\mathbf{L46}_6\mathbf{A6}_4]$[117] ($N_6$–$N_6$–$N_6$) where all three of the Fe^{II} centres underwent SCO. These complexes have shown a range of gradual to abrupt SCO, with $T_{1/2}$ varying with the **R** group, anions and solvent molecules present.

In 1983, the first structurally characterized trinuclear SCO-active complex, $[(Fe_3(\mathbf{L38})_6(H_2O)_6)](CF_3SO_3)_6$, was reported by Reedijk and co-workers.[109] This complex showed an abrupt SCO of one third of the Fe(II) ions, as seen by Faraday balance at 203 K and confirmed by Mössbauer studies. By incorporating a hydroxyl group at C2 of the ethyl group (*i.e.* use of **L39**, Chart 9), the $T_{1/2}$ was tuned to room temperature (290 K) which was attributed to the incorporation of hydrogen bonding into the system which increased the ligand field strength at the central metal atom.[112]

The effect of anion variation on the complex of **L40** (Chart 9, 4-(4-isopropyl)triazole) was studied by Haasnoot and co-workers.[110] $[Fe_3\mathbf{L40}_6(H_2O)_6]^{6+}$ showed a gradual spin transition at 242 K and 187 K, for the tosylate and triflate anions, respectively. By varying the R group from **L41**[111] to **L42**[113] with tosylate anions, the $T_{1/2}$ values changed slightly to 245 K, which was similar to the case of **L40**, and 148 K, respectively.

Galán-Mascarós and co-workers reported $[Fe_3(\mathbf{L43})_6(H_2O)_6]\cdot 8H_2O$ with hysteresis in its partially dehydrated form, where **L43**$^-$ is anionic in nature with a highly polar functional group at the 4-position. It showed three crystallographic phases with three different magnetic behaviours (Fig. 28a). The original compound had a single step spin transition below 250 K with $T_{1/2}$ at 150 K. Upon partial dehydration at 320 K the second phase occurred and showed spin transition with hysteresis. The third phase, observed after heating at 393 K, was paramagnetic down to low temperature. For the first phase, the $\chi_m T$ value at room temperature was 9.25 cm^3 K mol^{-1}, as expected for three independent HS iron(II) centres. On heating, the $\chi_m T$ value remained constant from 300 K to 320 K, then decreased to 6.2 cm^3 K mol^{-1} at 330 K due to partial solvent loss to form the

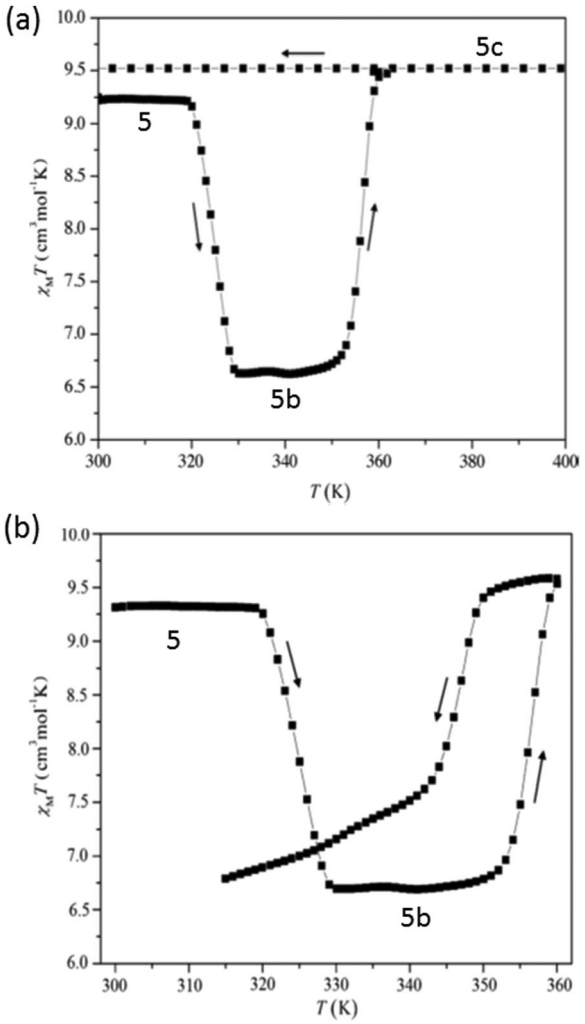

Fig. 28 (a) Plots of $\chi_m T$ *versus* T for $[Fe_3\mathbf{L43}_6(H_2O)_6]\cdot 8H_2O$; magnetic behaviour of all three crystallographic phases, (b) for $[Fe_3\mathbf{L43}_6(H_2O)_6]\cdot 8H_2O$ (5 in this figure) upon heating above room temperature (320 K) showing the transformation into phase partially de-solvated $[Fe_3\mathbf{L43}_6(H_2O)_6]$ (5b in this figure). Figure adapted from ref. 114 with permission. Copyright 2014 John Wiley and Sons.

second phase. This then showed an abrupt increase to 9.44 cm^3 K mol^{-1} at 360 K, and a 14 K wide hysteresis ($T_{1/2}\uparrow\downarrow$: 357, 343 K) on cooling down again (Fig. 28b).[114]

The same group subsequently reported the trinuclear complex of anionic $\mathbf{L44}^{2-}$ (Chart 9), $(Me_2NH_2)_6[Fe_3(\mathbf{L44})_6(H_2O)_6]\cdot 6H_2O$, in which the N^4-substituent is ethanedisulphonate. This compound showed a one step SCO above room temperature, with a 65 K wide thermal hysteresis loop (Fig. 29, inset filled squares). The $\chi_m T$ value was 6.37 cm^3 K mol^{-1} at 300 K, corresponding to [HS–LS–HS], and remains constant down to 50 K. On heating above 360 K it increased, and reached 7.92 cm^3 K mol^{-1} at 400 K, consistent with [HS–HS–HS]. Maintaining the sample at 400 K, $\chi_m T$ kept increasing over time and saturated at 8.89 cm^3 K mol^{-1} and the cooling cycle showed a 90 K wide and reproducible hysteresis, with $T_{1/2}\uparrow\downarrow$ = 400 K and 310 K (Fig. 29, inset empty squares). They have also studied the temperature induced excited spin transition (TIESST) effect. The excited spin state

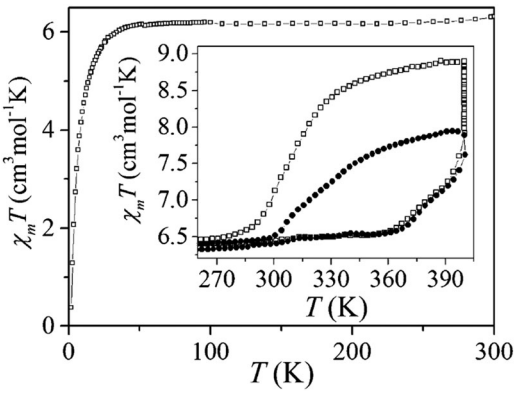

Fig. 29 Plot of $\chi_m T$ *vs.* T for $(Me_2NH_2)_6[Fe_3(\mathbf{L44})_6(H_2O)_6]\cdot 6H_2O$ in the range of 2–300 K. Inset: 270–400 K range, empty squares show the saturated magnetic behaviour of $(Me_2NH_2)_6[Fe_3\mathbf{L44}_6(H_2O)_6]\cdot 6H_2O$ when maintained at 400 K. Figure is reproduced from ref. 115. Copyright 2015 ACS.

(metastable-HS*) was thermally trapped and remained HS* at high temperature, T_{TIESST} = 250 K, which was the highest value ever reported.[115]

Neville and co-workers have recently reported $[Fe_3(\mathbf{L45})_6(p\text{-tol})_2(MeOH)_4](p\text{-tol})_4$ (p-tol = p-tolylsulfonate), which showed a gradual one step spin transition with no hysteresis. The χT value at 300 K was 10.2 cm^3 K mol^{-1} indicating fully HS Fe(II), then decreased gradually to 7.8 cm^3 K mol^{-1} at 50 K, which corresponds to one third of Fe(II) undergoing SCO to LS,[116] as is usual in these trinuclear complexes (see above).

In 2017, Marchivie and co-workers reported that $[Fe_3\mathbf{L46}_6(\mathbf{A6})_6]$ (Chart 9, **A6** = 1,1,3,3-tetracyano-2-thioethylpropenide), with N_3N_3–N_6–N_3N_3 coordination spheres around each Fe(II), undergoes an abrupt one-step complete SCO at 318 K, 3LS → 3HS.[117] At 380 K, the $\chi_m T$ value was 9.48 cm^3 K mol^{-1}, attributed to three uncoupled HS Fe(II) centres. The SCO curve decreased sharply at 320 K to 0.0 cm^3 K mol^{-1}, consistent with complete SCO to fully LS. The structural transition was also monitored by single crystal X-ray crystallography and DSC studies (Fig. 30).

Most recently, Tong, Dong, and co-workers used 4-amino-1,2,4-triazole, **L47** (Chart 9), to generate the trinuclear complex $[Fe_3(\mathbf{L47})_6(SCN)_4(H_2O)_2](SCN)_2\cdot H_2O$.[118] Heating at 400 K caused

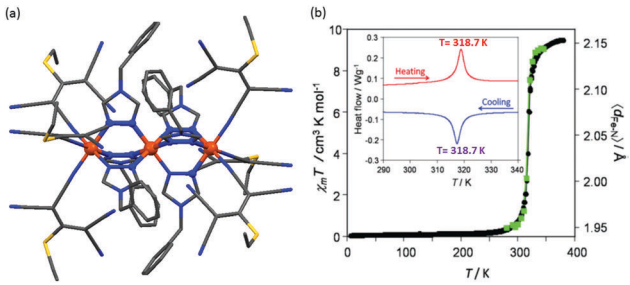

Fig. 30 Data for $[Fe_3\mathbf{L46}_6(\mathbf{A6})_6]$: (a) crystal structure (b) plot of $\chi_m T$ *vs.* T (black circle) and the average Fe–N distances (green squares) around the transition region. Inset: DSC study in both exo- and endo thermic modes. Structure redrawn from CCDC data. Figure (b) is adapted from ref. 117 with permission. Copyright 2017 RSC.

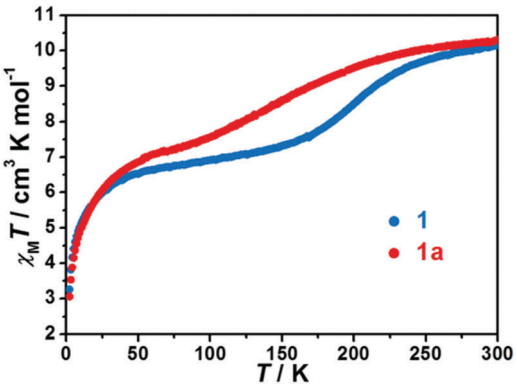

Fig. 31 $\chi_m T$ *vs.* T plots for as synthesised $[Fe_3(\mathbf{L47})_6(SCN)_4(H_2O)_2](SCN)_2 \cdot H_2O$ (blue, labelled 1 in this figure) and de-solvated $[Fe_3(\mathbf{L47})_6(SCN)_5(H_2O)](SCN)$ (red, labelled 1a in this figure). Figure adapted with permission from ref. 118. Copyright 2018 RSC.

the complex to undergo a thermally induced single crystal-to-single crystal transformation, losing two water molecules and becoming $[Fe_3(\mathbf{L47})_6(SCN)_5(H_2O)](SCN)$. This changed the SCO $T_{1/2}$ from 202 to 160 K, with the SCO being gradual and, as usual (see above), only being observed for the central Fe(II) ion in both cases, *i.e.* [HS–HS–HS] ↔ [HS–LS–HS] (Fig. 31).[118]

Tetrametallic anion-bridged Fe_4 squares

The metal ions in cyanometallates like $[Fe(CN)_6]^{4-}$ are LS due to the coordination of six strong field π-acceptor CN^- anions.[119] Such cyanometallate polyanions can be used to bridge other metal ions, as both the C and N of the cyanide anion can coordinate, and this has been a profitable line of enquiry for the generation of Single Chain Magnets (SCMs).[120] But to generate SCO-active complexes requires a significant reduction in the number of CN^- ligands, with weaker field co-ligands being used in place of some of them.[121]

In this section we consider CN^- or ($\mathbf{dca}^-$, Chart 7) bridged tetranuclear Fe(II) squares (Fig. 2, **4A**), featuring an Fe_4(μ-mono-/di-cyano)$_4$ core, with capping ligands (Chart 10) completing the, mixed N_4C_2–N_6 with cyano bridges or all –N_6 with dicyano bridges, octahedral coordination environments around the Fe(II) centres,[122–125] *i.e.* two *cis*-sites are occupied by N/C of two mono-/di-cyanide ions and the remaining four sites are occupied by either one tetradentate or two bidentate 'capping' ligands (Chart 10). In the case of μ-CN bridged squares, the Fe···Fe distance is ∼5 Å, whereas in $\mathbf{dca}^-$ bridged squares this distance is ∼8 Å (Table 7). The octahedral distortion Σ of the Fe(II) centres in these squares is modest: LS in the range 31–70° and HS in the range 74–109° (Table 7).

Oshio and co-workers have reported several such squares. The first, reported in 2005, featured a mixture of tetradentate **L35** and bidentate **L48** capping ligands (Chart 10). Initially, $[Fe_2\mathbf{L35}(\mathbf{L48})_2(\mu\text{-}NC)_2]_2(PF_6)_4$ was studied, in which $[Fe\mathbf{L35}]^{2+}$ and $[Fe(\mathbf{L48})_2]^{2+}$ centres are alternately arranged in the square, and bridged by four cyanide groups – with the carbon atoms of CN^- always binding to $[Fe(\mathbf{L48})_2]^{2+}$. This leads to alternating N_4C_2 and N_6 coordination of the four Fe(II) centres in the square. The magnetic studies showed thermally induced two step SCO, with $T_{1/2}$ = 160 K and 380 K. Up to 100 K all Fe^{II} sites are LS ($\chi_m T$ = 0.3 cm^3 mol^{-1} K), then upon warming to 200 K, χT increases to 3.2 cm^3 mol^{-1} K, corresponding to one HS iron site. X-ray crystallography at 200 K revealed that this SCO event occurs at one of the two $[Fe(\mathbf{L35})]^{2+}$ units (where both CN bridges bond through the N atom). Upon further increasing the temperature, the $\chi_m T$ remained constant until 300 K, then increased to 4.9 cm^3 mol^{-1} K at 400 K, which corresponds to 57% of the second $[Fe(\mathbf{L35})]^{2+}$ unit becoming HS (Fig. 32a).[122]

The authors also monitored SCO by reflectance studies on crystals at 100 K and 300 K on the (001) plane with unpolarised light. At 100 K, the spectra consisted of one sharp peak at 2.13 eV (582 nm) and two broad peaks at 2.3 eV (539 nm) and 2.6 eV (477 nm) (Fig. 32b). These peaks were assigned to d–d transitions of the LS Fe(II) centres in the $[Fe(\mathbf{L48})_2]^{2+}$ and $[Fe(\mathbf{L35})]^{2+}$ units respectively. At 300 K, two broad peaks merged at 2.40 eV (517 nm) and one new sharp peak appeared at 1.47 eV (843 nm) which was assigned to a d–d transition of a HS Fe(II) of a $[Fe(\mathbf{L35})]^{2+}$ moiety (Fig. 32b).

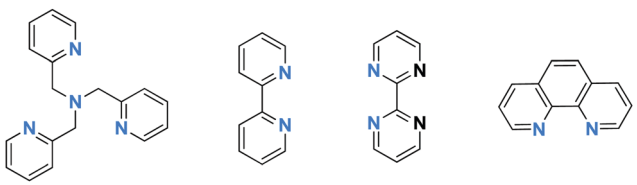

Chart 10 Capping ligands used in anion bridged SCO-active Fe(II) tetrametallic square complexes (Fig. 2, **4A**).

Table 7 Selected parameters for SCO-active tetranuclear Fe(II) squares (Fig. 2, **4A**). LS centres in italics

	T (K)	Fe–Fe (Å)	Σ (°)	Spin state	$T_{1/2}$ (K)	Lit.
$[Fe_2\mathbf{L35}(\mathbf{L48})_2(\mu\text{-}NC)_2]_2(PF_6)_4$	100	5.00, 4.95. 4.99, 4.99	*52*, *61*, *47*, *45*	LS–LS–LS–LS	160, 380	122
	200	5.04, 5.02, 4.99, 4.99	*50*, 108, *48*, *45*	LS–HS–LS–LS		
	293	5.05, 5.02, 5.0, 4.99	*49*, 109, *46*, *47*	LS–HS–LS–LS		
$[Fe_2\mathbf{L31}_2(\mathbf{L48})_2(NC)_2]_2(PF_6)_4 \cdot 6MeOH \cdot 4H_2O$	200	4.96, 4.98,	49, *56*	2LS–2LS	Not stated	123
$[Fe(\mathbf{L35})(CN)]_4(BF_4)_4 \cdot MeCN \cdot H_2O$	100	4.94, 4.97, 4.94, 4.95	*68*, *49*, *55*, *70*	LS–LS–LS–LS	Not stated	124
$[Fe(\mathbf{L35})(CN)]_4(BF_4)_4 \cdot 0.75MeCN \cdot H_2O$	210	4.59, 4.99, 4.96, 4.98	*69*, 74, *47*, 79	LS–HS–LS–HS		
$[Fe(\mathbf{L35})\{\mathbf{dca}\}]_4(BF_4)_4 \cdot 2(H_2O)$	150	8.23, 8.40	*54*, *60*	2LS–2LS	302, 194	126
	250	8.44, 8.36	*57*, 91	2LS–2HS		
$[Fe(\mathbf{L35})\{\mathbf{dca}\}]_4(BF_4)_4$	350	8.51, 8.49	88, 98	2HS–2HS		
$[Fe_4(\mathbf{L49})_4(\mathbf{L35})_2(CN)_4](PF_6)_4 \cdot 1MeCN \cdot H_2O$	100	4.98, 4.99	*44*, *43*	2LS–2LS	Not stated	125
$[Fe_4(\mathbf{L49})_4(\mathbf{L35})_2(CN)_4](PF_6)_4$	370	5.07, 5.04	*31*, 86	2LS–2HS		

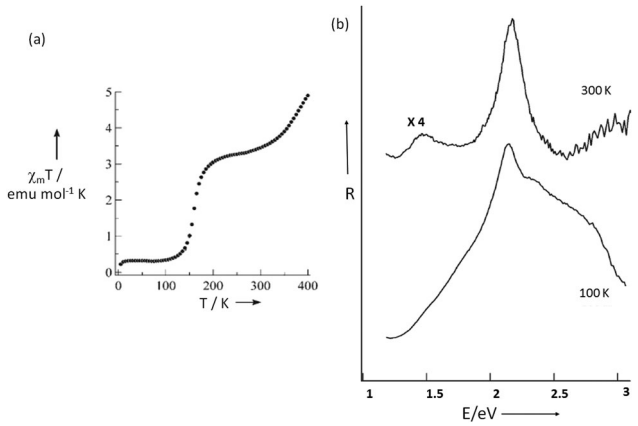

Fig. 32 (a) Plot of χ_mT *vs.* *T* for $[Fe_2$**L35**$($**L48**$)_2(u\text{-}CN)_2]_2(PF_6)_4$; (b) reflectance spectra; *R* = reflectivity, *E* = photon energy. Figure adapted with permission from ref. 122. Copyright 2005 John Wiley and Sons.

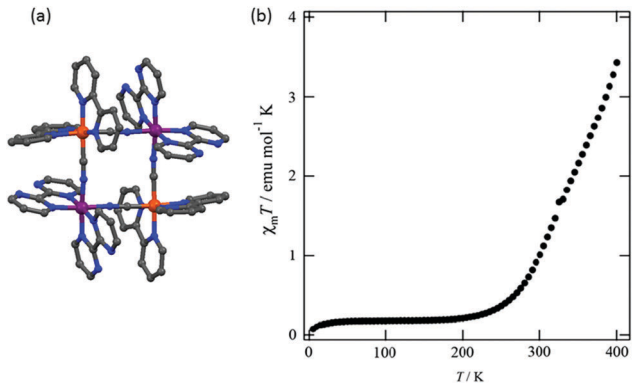

Fig. 33 (a) Crystal structure of the cation of $[Fe_4($**L48**$)_2($**L31**$)_2(CN)_4](PF_6)_4$, SCO active Fe(II) centres violet (b) plot of χ_mT *vs.* *T* for $[Fe_4($**L48**$)_2($**L31**$)_2(CN)_4](PF_6)_4{\cdot}6MeOH{\cdot}4H_2O$. Structure redrawn from CCDC data. (b) Reproduced with permission from ref. 123. Copyright 2009 Elsevier.

The same group has reported a related heteroleptic tetranuclear cyanide bridged square, again using bidentate **L48** but replacing tetradentate **L35** by two bidentate **L31** ligands (Chart 10), $[Fe_4($**L48**$)_2($**L31**$)_2(CN)_4](PF_6)_4{\cdot}6MeOH{\cdot}4H_2O$ (Fig. 33a). Again the corners alternate between $[Fe($**L48**$)_2]^{2+}$ and $[Fe($**L31**$)_2]^{2+}$ around the square. The complex remained LS up to 250 K, then the χ_mT product increased gradually to 3.42 cm^3 mol^{-1} K at 400 K. The $[Fe($**L48**$)_2]^{2+}$ corners remain LS throughout, whereas the $[Fe($**L31**$)_2]^{2+}$ corners undergo SCO to HS in one step (Fig. 33b).[123]

Shatruk and co-workers prepared homoleptic capped Fe^{II}_4 squares using the tetradentate capping ligand **L35** (Chart 10). $[Fe($**L35**$)(CN)]_4X_4{\cdot}n$MeOH (X = BF_4^-, ClO_4^-), revealed SCO curves which were strongly influenced by the presence of solvent MeOH molecules, while counteranion variation had little effect.[124] The χ_mT value of both complexes covered in a small amount of MeOH mother liquor at 300 K was ~7.5 cm^3 mol^{-1} K which was consistent with two HS and two LS Fe(II) centres in each cluster. The wet samples showed abrupt SCO with complete one step spin conversion of two N_6 Fe(II) HS ions to the LS state at

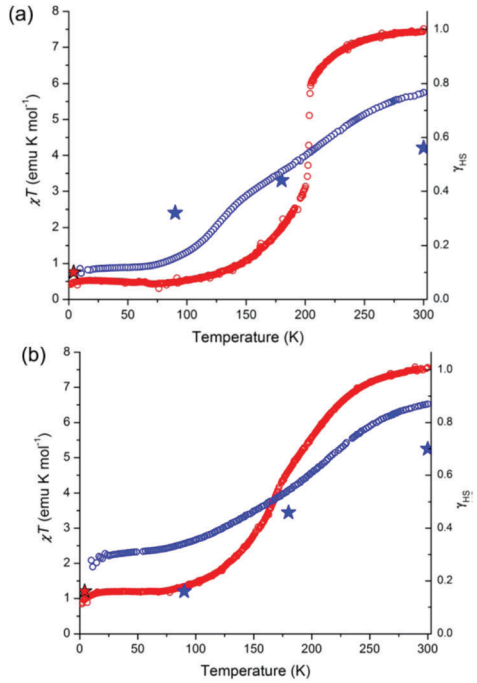

Fig. 34 Plot of χT and the high spin fraction (γ_{HS}) *vs.* *T* for the two HS Fe(II) sites attributed to being in N_6 coordination environments: red curves, as synthesized (wet) samples; blue curves, powder samples (a) $[Fe($**L35**$)(\mu\text{-}CN)]_4(BF_4)_4$ and (b) $[Fe($**L35**$)(\mu\text{-}CN)]_4(ClO_4)_4$. Figures adapted with permission from ref. 124. Copyright 2014 ACS.

low temperature. Dry powder samples showed more gradual incomplete one-step spin transition (Fig. 34).[124]

Zheng and co-workers have also used the tetradentate **L35** capping ligand (Chart 10) to prepare a homoleptic capped square, but this time featuring dicyanamide bridges, $[Fe($**L35**$)($**dca**$)_2]_4(BF_4)_4{\cdot}2(H_2O)$. In this square all of the Fe(II) centres have N_6 coordination (Fig. 35a). It exhibits both thermal and light irradiation induced two step, complete SCO in both the hydrated and dehydrated forms. The as-synthesized sample was heated at 350 K to SCSC transform the hydrated crystals to the dehydrated form. The asymmetric unit of the as-synthesised hydrated form contained two crystallographically different Fe(II) centres. At 150 K, $\Sigma = 60^\circ$ and 54°, which changed to 91° and 57° at 250 K (Table 7), which suggested that two identical iron(II) centres have undergone

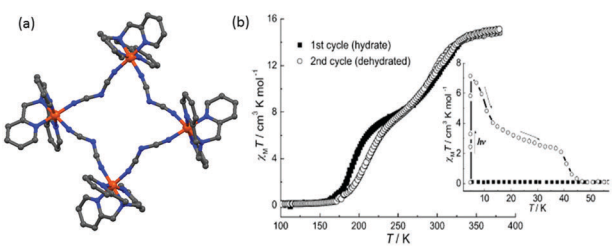

Fig. 35 (a) Crystal structure of the cation of $[Fe($**L35**$)($**dca**$)_2]_4(BF_4)_4{\cdot}2H_2O$ (b) plots of χ_mT *vs.* *T* for $[Fe($**L35**$)($**dca**$)_2]_4(BF_4)_4$; in two successive temperature cycles 300–100–380 K (square), and 380–100–380 K (circle). Inset: LIESST studies. Structure redrawn from CCDC data. (b) Reproduced with permission from ref. 126. Copyright 2011 John Wiley and Sons.

SCO to HS. At 350 K, solvent molecules are removed but crystal packing remained intact and Σ changed to 98.0 and 88.2° corresponding to all Fe(II) in the HS state. For the two-step SCO of the hydrated square $T_{1/2}$ = 302 and 194 K, and for the dehydrated form $T_{1/2}$ = 294 and 211 K. The $\chi_m T$ *vs.* T curve follows the same route for the cooling and heating processes, except for a 6 K wide hysteresis (Fig. 35b) in the 4LS to 2HS–2LS step. The LIESST effect was studied at 5 K with 457 nm irradiation: the maximum $\chi_m T$ observed was 7.08 cm^3 K mol^{-1}, which was assigned to 47.5% photo-excited HS population. When the light source is switched-off, the metastable HS state relaxed steeply between 5–13 K, then smoothly from 13–33 K, with a plateau at approximately 3 cm^3 mol^{-1} K which corresponds to relaxation of half of the metastable HS population (Fig. 35b, inset).[126]

Real and co-workers reported a heteroleptic capped square of **L35** and **L49** (Chart 10), $[Fe_4(\mu\text{-}CN)_4(\mathbf{L49})_4(\mathbf{L35})_2](PF_6)_4$. Again the cyanide bridges are ordered, binding *via* N to the $[Fe(\mathbf{L35})]^{2+}$ corners and *via* C to the $[Fe(\mathbf{L49})_2]^{2+}$ corners. This complex undergoes incomplete and gradual one-step SCO. The $\chi_m T$ value at 400 K was 5.3 cm^3 K mol^{-1}, which corresponds to a value just below that expected for a 2HS–2LS state, and decreased to 0.5 cm^3 K mol^{-1} at 4 K, *i.e.* fully LS. The crystal structure investigation showed that the two N_6-coordinated $[Fe(\mathbf{L35})]^{2+}$ units are SCO active, while the two N_4C_2-coordinated $[Fe(\mathbf{L49})_2]^{2+}$ units remain LS up to 370 K.[125] The authors also studied the magnetic behaviour on changing the ligand field strength by varying the extent of methyl substitution at the 6-position of one or two of the pyridine groups of **L35**. They observed that these methyl substituents increased the steric constraint which led to longer Fe–N bond distances, weakening the ligand strength and stabilising the HS state of $[FeN_6]$ and LS $[FeN_4C_2]$ centres all over the temperature range.[125]

Tetranuclear [2 × 2] grids Fe_4L_4

Like the tetrametallic squares, tetrametallic [2 × 2] grids (Fig. 2, **4B**) are an appealing architecture for SCO design, with the possibility of multistability being exhibited in an array of four addressable metal ion sites.[42,43] The combination of octahedral Fe(II), the most commonly studied SCO metal ion, with bis-terdentate rigid linear bridging ligands to, in a controlled way, self-assemble Fe_4L_4 grids is therefore a very attractive pursuit in SCO research. Again this is a relatively young area of investigation, with few reported Fe_4L_4 grids in the literature, and even fewer examples that exhibit SCO. In fact only 21 ligands (Chart 11) have been reported to produce SCO-active Fe_4 grids,[39,127–137] the first of which was reported in 2000 – this was also the first example of an SCO-active tetranuclear complex,[127] and held the record for the largest nuclearity discrete SCO-active complex until 2009 (see the 'nanoball' later). Interestingly, 16 of the ligands employed to date feature pyrimidine-bridging moieties **L50–L65**$^-$ (only 6 of the resulting grids have been structurally characterised, one in two different spin states, Table 8), whilst the other 5 ligands, **L66**$^-$ to **L70** (all of the resulting grids have been structurally characterised, Table 9), present a wide range of different bridging moieties (Chart 11).

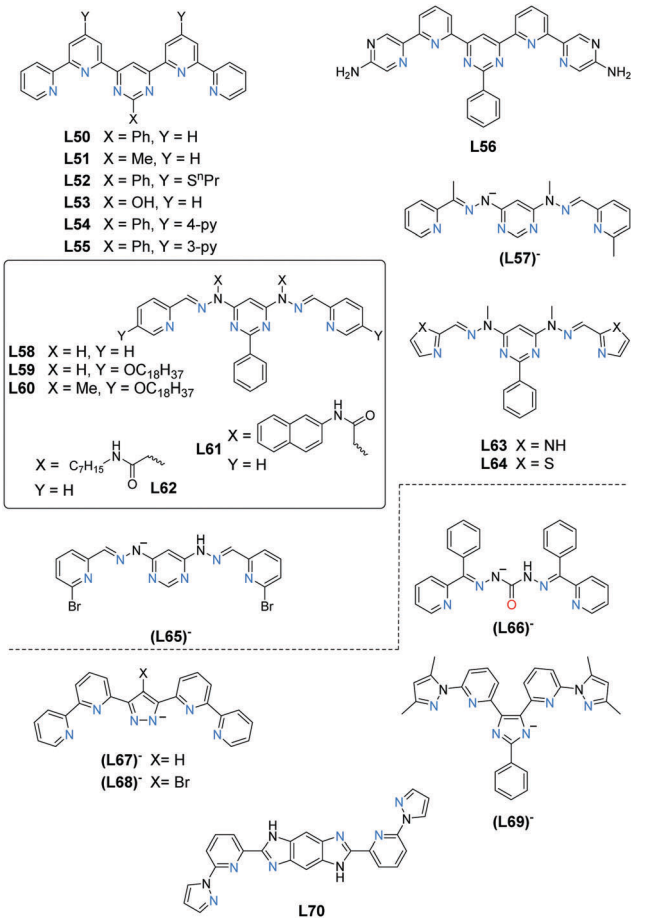

Chart 11 The 21 bis-terdentate ligands known to form SCO-active Fe_4L_4 grids (Fig. 2, **4B**). All ligands provide N_6 donor sets to the octahedral Fe(II) centres, except $(\mathbf{L66})^-$ which provides a N_4O_2 donor set, to the octahedral Fe(II) centres, so no co-ligands are bound.

In each case the ligand is bis-terdentate and as such the four ligands in the corresponding Fe_4L_4 grid complexes provide all of the donor atoms to the Fe(II) centres with no co-ligands bound. This, coupled with the fact that all ligands contain either a heterocyclic or single atom bridging moiety, results in a very rigid coordination environment and significant octahedral distortions at the Fe(II) centres. As a result, these grids impose much larger Σ values on the Fe(II) centres (LS 84–125°, HS 129–176°; Tables 8 and 9) than those observed in the other tetranuclear architectures, squares (LS 31–70°, HS 79–109°; Table 7) and cages (LS 43–75°, HS 69–121°; see later, Tables 10 and 11).

In 2000, Lehn, Gütlich and co-workers reported the first SCO-active Fe(II) [2 × 2] grid.[127] The grid was assembled from the linear bis-terdentate ligand 4,6-bis(2,2′-bipyridin-6-yl)-2-phenylpyrimidine (**L50**, Chart 11), and the structure of $[Fe_4(\mathbf{L50})_4]^{8+}$ was determined by X-ray crystallography (Fig. 36a). Analysis of the Fe–N bond lengths at 293 K clearly revealed three of the Fe(II) centres were HS while the fourth had bond lengths intermediate between those typical for HS and LS states. In contrast, at 100 K three of the Fe(II) centres have intermediate Fe–N bond lengths (but closer to LS) and one is HS, indicating that a thermal SCO has occurred. Variable temperature magnetic susceptibility

Table 8 Selected parameters for the structurally characterised SCO-active tetranuclear Fe(II) 2 × 2 grids (Fig. 2, **4B**) of pyrimidine-based ligands **L50–L65** (Chart 11, NB). The grids of pyrimidine-based ligands **L55–L64** were not structurally characterised. See Table 9 for grids of the non-pyrimidine-based ligands (Chart 11). LS centres in italics

	T (K)	Fe–Fe (Å)	Σ (°)	Spin state	$T_{1/2}$ (K)	Lit.
$[Fe^{II}_4(\mathbf{L50})_4](ClO_4)_8\cdot 9MeCN\cdot 1.25H_2O$	100	6.42, 6.35, 6.32, 6.42	*88*, *87*, *91*, 146	HS–3LS	Not stated	127
	293	6.43, 6.47, 6.50, 6.47	137, *109*, 143, 146	3HS–LS		
$[Fe^{II}_4(\mathbf{L53})_4](ClO_4)_8\cdot 3MeCN\cdot 5H_2O$	120	6.27, 6.33, 6.42, 6.39	160, 146, *125*, *98*	2HS–2LS	Not stated	128
$[Fe^{II}_4(\mathbf{L54})_4](ClO_4)_7(Cl)\cdot 7MeNO_2\cdot 6H_2O$	120	6.30, 6.35	*85*, *84*	2LS–2LS	Not stated	128 and 129
$[Fe^{II}_4(\mathbf{L65})_4]Cl_4\cdot 9H_2O$	153	5.93, 5.98	*88*, *91*	2LS–2LS	Not stated	135
$[Fe^{II}_4(\mathbf{L65})_4](BF_4)_4\cdot 7H_2O$	153	6.07, 6.06	*86*	4LS	Not stated	135

Table 9 Selected parameters for the structurally characterised SCO-active tetranuclear Fe(II) 2 × 2 grids (Fig. 2, **4B**) of non-pyrimidine-based ligands **L66** to **L70** (Chart 11). See Table 8 for grids of the pyrimidine-based ligands (Chart 11). LS centres in italics

	T (K)	Fe–Fe (Å)	Σ (°)	Spin state	$T_{1/2}$ (K)	Lit.
$[Fe^{II}_4(\mathbf{L66})_4](BF_4)_4\cdot MeOH\cdot 2H_2O$	123	3.77	*105*	2LS–2HS	175	134
		3.84	129			
		3.87	149			
		3.75	*113*			
$[Fe^{II}_4(\mathbf{L66})_4](BF_4)_4\cdot MeOH\cdot 2H_2O$	283	3.84	149	HS–HS–HS–HS		
		3.73	147			
		3.86	146			
		3.88	150			
$[Fe^{II}_4(\mathbf{L67})_4](BF_4)_4\cdot 4DMF$	133	4.52	145	3HS–LS	Not stated	39
		4.51	*97*			
		4.42	144			
		4.57	156			
$[Fe^{II}_4(\mathbf{L67})_4](BF_4)_4\cdot 4DMF$	233	4.88	151	HS–HS–HS–HS		
		4.45	137			
		4.45	149			
		4.51	152			
$[Fe^{II}_4(\mathbf{L67})_4](BF_4)_6\cdot 3CH_3CN$	133	4.53	*92*	2LS–2HS	LS–HS	39
		4.59	148			
$[Fe^{II}_3(\mathbf{HL67})_2(\mathbf{L67})_2](BF_4)_4\cdot 2CH_3CN$	133	4.59	*95*	2LS–HS	↑↓355, 329	138
		4.54	*94*			
			142			
$[Fe^{II}_4(\mathbf{L68})_4](PF_6)_4\cdot DMF\cdot THF$	133	4.50	*99*	2LS–2HS	2LS–2HS	133
		4.48	170			
$[Fe^{II}_4(\mathbf{L68})_4](PF_6)_4\cdot 4DMF$	133	4.42	150	HS–HS–HS–HS–HS–HS–HS–HS	HS	133
		4.35	153			
		4.36	153			
		4.40	159			
		4.36	159			
		4.39	139			
		4.40	148			
		4.37	155			
$[Fe^{II}_4(\mathbf{L68})_4](ClO_4)_4\cdot 0.25DMF\cdot DME$	133	4.41	152	6HS–2LS	3HS–1LS	133
		4.48	142			
		4.48	150			
		4.50	*90*			
		4.50	*91*			
		4.51	173			
		4.46	136			
		4.47	159			
$[Fe^{II}_4(\mathbf{L68})_4](BF_4)_4\cdot THF\cdot 4H_2O$	293	4.44	150	4HS	250	133
$[Fe^{II}_4(\mathbf{L68})_4]Br_4\cdot 4DMF\cdot 2H_2O$	133	4.53	*105*	LS–HS–HS–HS	Not stated	133
		4.41	176			
			176			
			160			
$[Fe^{II}_4(\mathbf{L69})_4](BF_4)_4\cdot 2MeCN$	293	6.48	131	HS–HS–HS–HS	Not stated	136
		6.44	145			
		6.51	144			
		6.42	147			
$[Fe^{II}_4(\mathbf{L70})_4](CF_3SO_3)_8\cdot 12MeNO_2\cdot C_6H_{14}O$	180	9.16	*87*	2LS–2LS	310	137
		9.05	*85*			
$[Fe^{II}_4(\mathbf{L70})_4](CF_3SO_3)_5(F)_3\cdot 2MeNO_2\cdot H_2O$	180	7.33	167	2HS–2HS	HS	137
		7.22	152			

Table 10 Selected parameters for SCO-active tetranuclear Fe(II) tetrahedral cages (Fig. 2, **4C**) of the tri-topic, face bridging, ligands **L71–L74** (Chart 12). See Table 11 for the di-topic, edge bridging, ligands. LS centres in italics

	T (K)	Fe–Fe (Å)	Σ (°)	Spin state	Lit.
$[Fe^{II}_4(\mathbf{L71})_4](BF_4)_8{\cdot}14.75MeCN{\cdot}4.5C_6H_6{\cdot}3H_2O$	153	14.28, 14.28, 14.28, 13.99, 14.14, 13.98	*61*, *60*	2LS–2LS	140
$[Fe^{II}_4(\mathbf{L71})_4](BF_4)_8{\cdot}14.75CH_3CN{\cdot}4.5C_6H_6{\cdot}3H_2O$	293	14.46, 14.29, 14.11, 14.52, 14.46, 14.11	66, 69	2LS/HS–2HS	140
$Fe^{II}_4(\mathbf{L73})(CF_3SO_3)_8$	100	6 × 11.85	*65*	4LS	141
$[Fe^{II}_4(\mathbf{L74})_4](BF_4)_4{\cdot}16CH_3CN$	100	3 × 14.61, 3 × 14.78, 3 × 14.54, 3 × 14.94, 3 × 14.56, 3 × 15.14	2 × 82, *2 × 67*, *2 × 70*, 2 × 121, 2 × 86, *2 × 75*	6LS–6HS	142

Table 11 Selected parameters for SCO-active tetranuclear Fe(II) tetrahedral cages (Fig. 2, **4C**) of the di-topic, edge bridging, ligands **L75–L78** (Chart 12). See Table 10 for the ti-topic, face bridging, ligands. LS centres in italics

	T (K)	Fe–Fe (Å)	Σ (°)	Spin state	Lit.
$[Fe^{II}_4(\mathbf{L75})_6](ClO_4)_8$ (*R*)	150	3 × 9.56, 3 × 9.67	*61*, *49*	LS–LS	143
$[Fe^{II}_4(\mathbf{L75})_6](ClO_4)_8$ (*S*)	123	3 × 9.66, 3 × 9.48	*60*, *42*	LS–LS	143
$[Fe^{II}_4(\mathbf{L76})_6](ClO_4)_8{\cdot}11.59MeCN{\cdot}2C_4H_{10}O{\cdot}H_2O$ (*R*)	123	9.66, 9.45, 9.70, 9.59, 9.64, 9.79	*56*, *58*, *56*, *64*	4LS	143
$[Fe^{II}_4(\mathbf{L76})_6](ClO_4)_8{\cdot}6MeCN$ (*S*)	123	9.74, 9.70, 9.68, 9.41, 9.77, 9.76	*56*, *55*, *60*, *63*	4LS	143
$[Fe^{II}_4(\mathbf{L77})_6](ClO_4)_8{\cdot}2MeCN$ (*S*)	123	3 × 9.53, 3 × 9.81	*55*, *57*	2LS	143
$[Fe^{II}_4(\mathbf{L78})_6](ClO_4)_8{\cdot}2MeCN$	173	11.35, 11.04, 11.90, 11.73, 11.95, 11.18, 3 × 11.97, 3 × 11.78	*43*, *45*, *49*, *43*, *53*, *50*	6LS	144

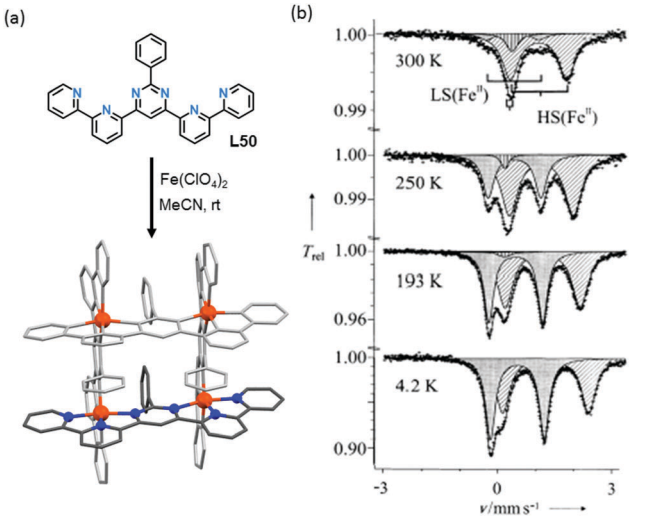

Fig. 36 (a) Reaction of 4,6-bis(2,2′bipyrid-6-yl)-2-phenyl-pyrimidine (**L50**) with iron(II) perchlorate in acetonitrile at room temperature to produce the corresponding $[Fe_4(\mathbf{L50})_4](ClO_4)_8$ [2 × 2] grid and (b) evidence of the SCO, by Mössbauer spectroscopy, from 80% HS at 300 K (top) to 46% HS at 4.2 K (bottom). Structure redrawn from CCDC data.[127] (b) Figure adapted, reproduced with permission, from ref. 127. Copyright 2000 John Wiley and Sons.

showed that there was indeed a SCO event, which was very gradual and incomplete over 300–30 K. The authors performed Mössbauer spectroscopy studies to yield further evidence of SCO (Fig. 36b) and were able to induce SCO by varying the pressure, and by the LIESST effect, making this a triply switchable SCO [2 × 2] grid.

Modifications to the bis-terdentate ligand, through substitution of peripheral groups at the pyrimidine or bipyridine groups, allowed for a family of closely related grids to be investigated. Substitution of the phenyl group at the pyrimidine-2-position for a methyl group (**L51**, Chart 11) accessed the second example of an Fe(II) SCO grid, whereas H or OH groups yielded diamagnetic analogues.[128] Further SCO-active grids were obtained by either the attachment of peripheral groups at the pyrimidine or bipyridine groups (X or Y, **L52–L55**, Chart 11)[128,129] or the use of bipyridine-like groups (**L56**, Chart 11).[128] Lehn and co-workers have since produced several more SCO-active Fe(II) grids of related pyrimidine ligands. In fact they have produced more than half of the known SCO-active Fe(II) grids in the literature. The other ligands used by them are also based on the pyrimidine bridging unit, but these ligands contain functionalised bis-hydrazone side arms and either pyridine[130,131] [$(\mathbf{L57})^-$ and **L58–L62**, Chart 11] or imidazole/thiazole[132] (**L63** and **L64**, Chart 11) rings, and various substitutions thereof, to complete the terdentate binding pockets. In each case where SCO was observed the transition was very gradual and incomplete across a wide thermal range.

In 2013 Kou and co-workers reported two SCO-active $[Fe_4(\mathbf{L65})_4]X_4$ grid complexes based on a bis-terdentate Schiff base ligand [$(\mathbf{L65})^-$, Chart 11].[135] Similar to the ligands employed by Lehn and co-workers, the ligand scaffold also features a central pyrimidine bridging moiety. The SCO for the X = Cl^- grid is incomplete, with the transition taking place above room temperature between (approximately) the [2HS–2LS] and [HS–3LS] states (Fig. 37, black data points). The transition is noticeably more abrupt than the pyrimidine based grids of Lehn and co-workers, and that of the X = BF_4^- grid is even more abrupt again and appears to be centred at about 400 K, the high temperature limit of the measurement (Fig. 37, red data points). Interestingly, the analogous grid with less bulky methyl groups in place of the bromine atoms on the ligand scaffold is fully LS to high temperature.

Whilst nearly all of the SCO-active Fe(II) [2 × 2] grids reported in the literature to date have iron(II) ions with an N_6 coordination sphere, there is one exception, the N_4O_2 coordinated grid from Sato and co-workers.[134] Here $(\mathbf{L66})^-$ (Chart 11) features two terdentate pockets which share one bridging oxygen atom, and the corresponding O-bridged $[Fe_4(\mathbf{L66})_4](BF_4)_4$ grid

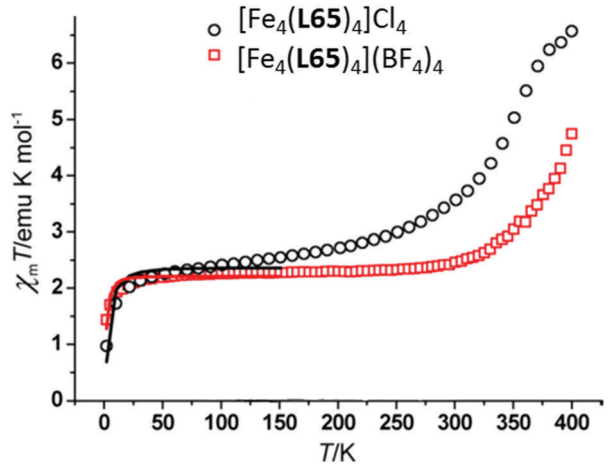

Fig. 37 $\chi_m T$ *vs.* *T* for the [2 × 2] grids of $[Fe_4(\mathbf{L65})_4]Cl_4{\cdot}9H_2O$ (black circles) and $[Fe_4(\mathbf{L65})_4](BF_4)_4{\cdot}6H_2O$ (red squares).[135] Figure adapted, reproduced with permission, from ref. 135. Copyright 2013 ACS.

complex undergoes an abrupt SCO from [4HS] to [2HS–2LS] centred around 175 K.

Another bis-terdentate bridging ligand family which has provided a wealth of Fe_4L_4 [2 × 2] grids are the bis-bipyridine pyrazolate family (Chart 11) from the group of Meyer. In 2010 they reported the synthesis of the $[Fe_4(\mathbf{L67})_4](BF_4)_4$ [2 × 2] grid (Fig. 38a) of the simple 3,5-bis{6(2,2′-dipyridyl)}pyrazolate ligand [$(\mathbf{L67})^-$, Chart 11].[39]

At room temperature both magnetic measurements and structural analysis indicate a fully HS state. Upon cooling to 133 K the structure is consistent with one LS Fe(II) and three HS Fe(II) ions in the grid complex and this is confirmed by a

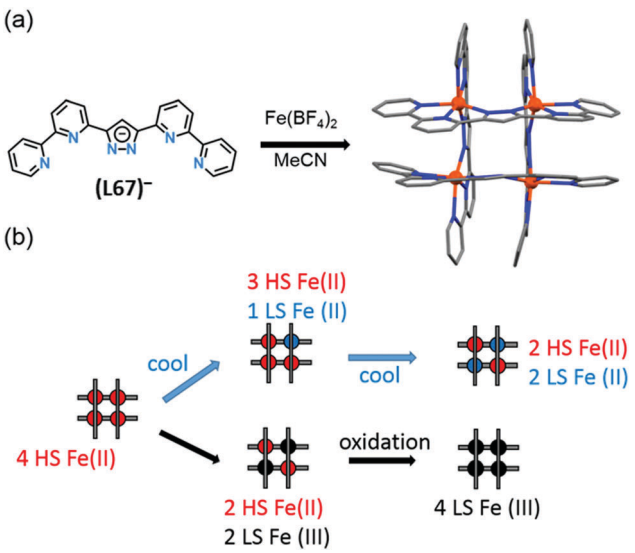

Fig. 38 (a) Synthesis of the $[Fe_4(\mathbf{L67})_4](BF_4)_4$ [2 × 2] grid from 3,5-bis{6(2,2′-dipyridyl)}pyrazolate $(\mathbf{L67})^-$ and iron(II) tetrafluoroborate in MeCN. (b) Overview of the physical (SCO) and chemical (redox) transformations of the grid complex $[Fe_4(\mathbf{L67})_4](BF_4)_4$. Structure redrawn from CCDC data.[39] Figure adapted, reproduced with permission, from ref. 39. Copyright 2010 John Wiley and Sons.

[3HS–LS] plateau in the $\chi_M T$ *vs.* *T* data. Cooling even further allows for the beginning of a second SCO event to be observed, the SCO of a second Fe(II) to the LS state, thus the complex almost reaches [2HS–2LS] at 50 K. Cyclic voltammetry revealed two separate Fe(II)/Fe(III) redox events, meaning the complex is doubly switchable, by SCO or redox, with multistep events observed for both phenomena (Fig. 38b). By stoichiometric control, Meyer and co-workers have been able to access the "corner" unit of their $[Fe_4(\mathbf{L67})_4]^{4+}$ grids, *i.e.* $[Fe(H\mathbf{L67})_2]^{2+}$ which crystallises as hydrogen-bonded dimers.[139]

Here the Fe(II) ion of each FeL_2 unit of the dimer is in the LS state, as evidenced by the short Fe–N bond lengths and regular octahedral geometry (Σ = 85.24°) as well as by Mössbauer spectroscopy. The LS $[Fe(H\mathbf{L67})_2]^{2+}$ complex suggests that the bipyridine-pyrazole binding pocket of **HL67** is strong field and not suited to SCO. However, when the ligand is pyrazolate and bridging two Fe(II) ions, in addition to the steric constraints of four rigid ligands holding four Fe(II) ions in a [2 × 2] grid, the binding environment facilitates SCO in the tetranuclear $[Fe_4(\mathbf{L67})_4]^{4+}$ complex.

Meyer and co-workers have since introduced a bromo substituent to the C^4 position of the pyrazolate ring, *i.e.* $(\mathbf{L68})^-$ (Chart 11), and subsequently synthesised the corresponding $[Fe_4(\mathbf{L68})_4]X_4$ grids.[133] Variation of the counteranion (X = PF_6^-, ClO_4^-, BF_4^-, Br^-) gave access to a variety of stable spin states, from [4HS] to [3HS–LS] to [2HS–2LS], with gradual thermal SCO between the states seen for some of the grids. The analogous grid of the C^4-methyl-substituted pyrazolate bis-bipyridine ligand is SCO inactive and persists in the [2HS–2LS] state up to 350 K; however, the authors note that the observed stability of the mixed spin state is favourable for potential use as a component for quantum cellular automata.[38] Finally, whilst technically not a [2 × 2] grid, the controlled formation of a trinuclear defect grid $[Fe_3(H\mathbf{L67})_2(\mathbf{L67})_2](BF_4)_4{\cdot}MeCN$ is nevertheless highly relevant work.[138] It exists in the [HS–2LS] state at room temperature, but after loss of the lattice solvent MeCN it can undergo thermal SCO to the [2HS–LS] state above room temperature.

Another prominent example of a SCO-active Fe(II) grid was reported by Oshio and co-workers, using a bis-(pyrazole-pyridyl) ligand with a central bridging imidazolate, $(\mathbf{L69})^-$ (Chart 11).[136] Here, a two-step hysteretic SCO occurs for the Fe(II) grid, $[Fe_4(\mathbf{L69})_4](BF_4)_4$, from the [4HS] state *via* the [3HS–LS] state to the [2HS–2LS] state (Fig. 39). At low temperatures, the [3HS–LS] state was also accessible by the LIESST effect, meaning the tri-stable [2 × 2] grid is doubly switchable by thermal variation and light irradiation. The corresponding mixed valent $[Fe^{II}_2Fe^{III}_2(\mathbf{L69})_4](BF_4)_6$ grid is fully LS at low temperatures and only undergoes an incomplete gradual SCO upon warming at one of the Fe(III) centres (Fig. 39).

An interesting case of two tauto-conformer Fe(II) [2 × 2] grids, where only one is SCO-active, was reported by Ruben and co-workers.[137] Here the bis-terdentate ligand **L70** (Chart 11) consists of a benzo-diimidazole bridge, with two imidazole-pyridyl side-arms. The central bridging unit can undergo tautomerisation which, along with rotation of the single bonds

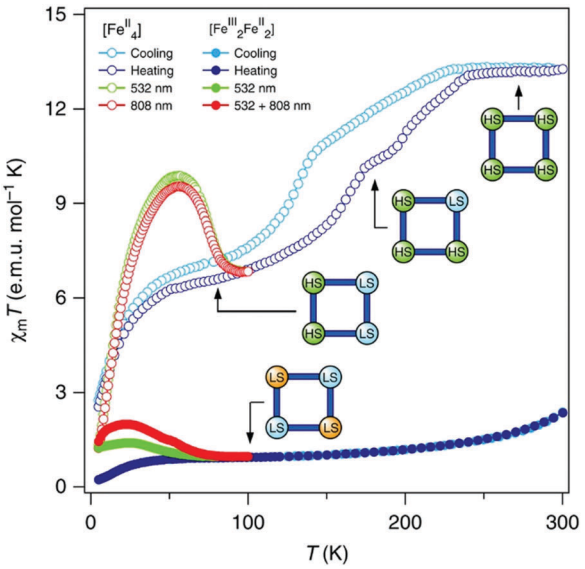

Fig. 39 $\chi_m T$ *vs.* T for the two [2 × 2] grids of the imidazolate-bridging ligand **L69**$^-$. [Fe$_4$(**L69**)$_4$](BF$_4$)$_4$·2MeCN undergoes multistep hysteretic SCO, [4HS] to [2HS–2LS], and also LIESST at low temperature. [Fe$^{II}_2$Fe$^{III}_2$(**L69**)$_4$](BF$_4$)$_6$ shows incomplete gradual Fe(III) SCO and modest LIESST effects. Figure reproduced with permission from ref. 136. Copyright 2014 Springer Nature.

between aromatic side-arm groups, results in the two terdentate pockets being in either a *cis* or *trans* arrangement (Fig. 40). This gives rise to the parallel formation of two isomeric grid complexes [Fe$_4$(**L70**)$_4$](CF$_3$SO$_3$)$_8$, which can be separated by fractional crystallisation – only one of which undergoes SCO. This is the direct result of the impact of the ligand conformations on the octahedral geometries at the Fe(II) centres: the *cis* conformation gives a highly distorted octahedral geometry (Σ = 160°) which locks the Fe(II) ions in the HS state, while the *trans* conformation reduces the octahedral distortion (Σ = 86°) and facilitates SCO to the LS state. This highlights that the geometric strain imposed by highly chelating ligands can have a larger influence on the spin state of the bound metal ions than the donor atoms alone.

Tetranuclear tetrahedral cage Fe$_4$L$_4$ and Fe$_4$L$_6$ complexes

In 2013, tetrametallic SCO-active architectures were expanded from [2 × 2] grids and squares to include Fe$_4$ tetrahedral cages (Fig. 2, **4C**).[140–144] The SCO-active Fe$_4$ cage architectures have been mostly prepared *via* self-assembly of Fe(II) with tritopic bidentate ligands which define the four faces of the Fe$_4$L$_4$ tetrahedral (Td) cages, *i.e.* four face-capping ligands (**L71–L74**, Chart 12), but examples of ditopic bidentate ligands which define the six edges of Fe$_4$L$_6$ Td cages are also known (**L75–L78**, Chart 12). In all cases, all of the donors to the bound Fe(II) centres are provided by the ligands. But, as these are bidentate, and quite long, they are reasonably flexible, so the Fe(II) octahedral distortion parameters Σ are smaller for these cages (42–121°, Tables 10 and 11) than for the tetranuclear grids (84–176°, Tables 8 and 9). The advent of these SCO-active 3D cages has also led to increased interest in studying SCO in solution,[14,16,145] in particular due to the possibility of guest recognition by the cage interior modifying the SCO-response.

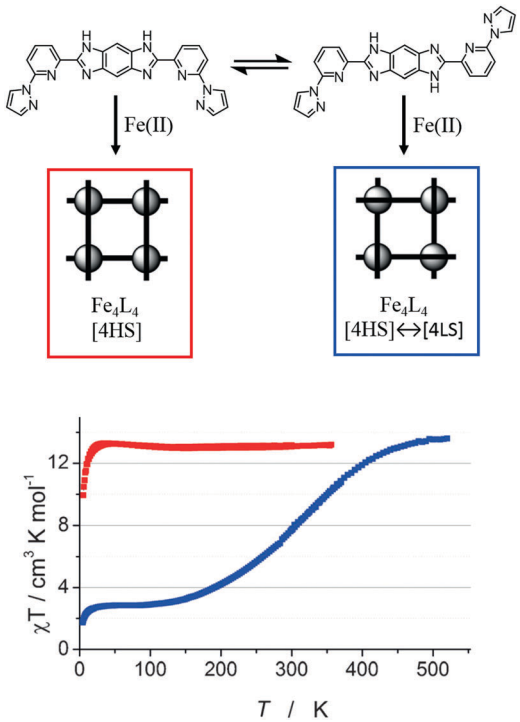

Fig. 40 (top) Tautomerisation of ligand **L70** gives rise to parallel formation of a HS grid (red box) where the ligands bind two metals in a *cis* mode, and a SCO-active grid (blue box) where ligands bind in a *trans* mode, and (bottom) $\chi_M T$ *vs.* T for the HS *cis*-grid (red) and SCO *trans*-grid (blue). Figure adapted, reproduced with permission, from ref. 137. Copyright 2016 John Wiley and Sons.

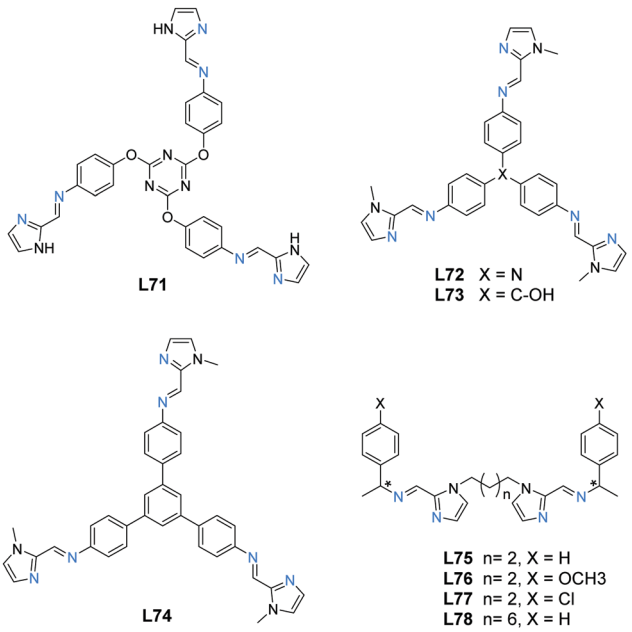

Chart 12 The eight ligands reported in the literature to form SCO-active Fe$_4$ tetrahedral cages. Four are tri-topic (face bridging, to give [Fe$_4$(**L**)$_4$]$^{8+}$) and other four are di-topic (edge bridging to give [Fe$_4$(**L**)$_6$]$^{8+}$). All provide N$_6$ donor sets to the octahedral Fe(II) metal ions through the binding of three sets of bidentate binding pockets. For **L75–L77** both the (*R*,*R*) and (*S*,*S*) configurations at the chiral (*) centre have been used to form cages.

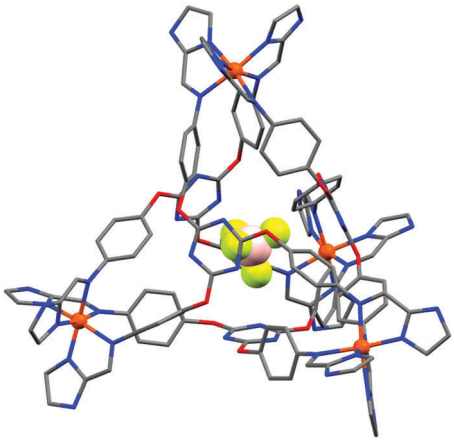

Fig. 41 Structure of the complex cation of $[Fe_4(\mathbf{L71})_4](BF_4)_8$ showing the encapsulated BF_4^- counteranion in spacefill.[140] Structure redrawn from CCDC data.

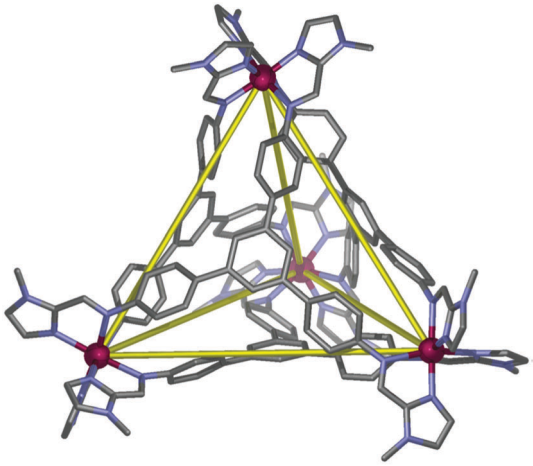

Fig. 43 Complex cation structure of $[Fe_4(\mathbf{L74})_4](BF_4)_8$. Figure reproduced, with permission, from ref. 142. Copyright 2015 RSC.

The first example of an SCO-active Td cage was reported by Kruger, Clérac and co-workers in 2013, with a face-capping ligand that was assembled from a triamine with a substituted triazine central moiety and 2-imidazolecarboxaldehyde (**L71**, Chart 12).[140] Coordination to Fe(II) resulted in a $[Fe_4(\mathbf{L71})_4](BF_4)_8$ tetrahedral cage (Fig. 41), which exhibits SCO in both the solid state and acetone solution.

Also in 2013, Nitschke, Brooker and co-workers reported a pair of self-assembled cages, $[Fe_4(\mathbf{L72})_4](OTf)_8$ and $[Fe_4(\mathbf{L73})_4](OTf)_8$ (Fig. 42), featuring smaller face-capping ligands (Chart 12).[141] While only $[Fe_4(\mathbf{L72})_4](OTf)_8$ was SCO-active in the solid state (approximately [4HS] to [HS–3LS] transition), both were SCO-active in nitromethane solution. Furthermore, the solution SCO properties were able to be tuned by encapsulation of Br^- or CS_2, with the $T_{1/2}$ lowering from 336 K for the empty cage $[Fe_4(\mathbf{L73})_4](OTf)_8$ to 328 K for Br^- or 324 K for CS_2, thus highlighting the exciting possibilities of synergistic host–guest chemistry and magnetic properties that arise when SCO is extended to such large architectures.

A third face-capped SCO-active $[Fe_4(\mathbf{L74})_4](BF_4)_8$ tetrahedral cage (Fig. 43), also self-assembled from an imidazole carboxaldehyde and a triamine (Chart 12), was reported by Li and co-workers in 2015.[142] It exhibits a very gradual SCO from fully HS at 300 K to approximately 75% HS at 50 K in the solid state.

An Fe(II) tetrahedral cage system which instead involves di-topic Schiff base bidentate ligands (**L75–L77**, Chart 12) that define the six edges of the tetrahedron, giving $[Fe_4(\mathbf{L})_6]^{8+}$ cages, was reported by Gu and co-workers in 2015 (Fig. 44).[143] Here the intrinsic at-metal chirality of the tetrahedral cage architecture is exploited to produce enantiopure homochiral cages by self-assembly involving either the (*R*) or (*S*) optical isomer of the amine. The enantiomers, of course, exhibit identical magnetic properties. R group variation (H, OCH_3, Cl) on the ligand, as well as solvent desorption, subtly affecting the (gradual and incomplete) SCO behaviour observed in the solid state. Specifically, below 200 K the cages are 3–18% HS when solvated

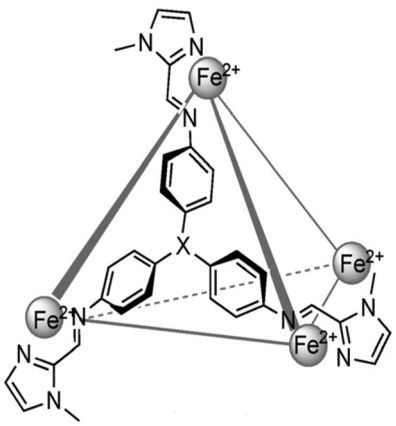

Fig. 42 Representation of the molecular structure of $[Fe_4(\mathbf{L72})_4](OTf)_8$ and $[Fe_4(\mathbf{L73})_4](OTf)_8$. Figure adapted, reproduced with permission, from ref. 141. Copyright 2013 John Wiley and Sons.

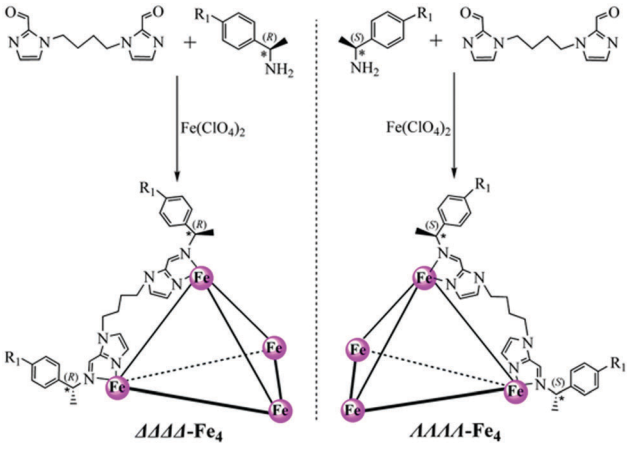

Fig. 44 Synthesis of enantiopure chiral tetrahedral $[Fe_4L_6]^{8+}$ cages, where L is **L75–L77**, by use of either (*R*)- or (*S*)-phenylethylamine. Figure reproduced with permission from ref. 143. Copyright 2015 RSC.

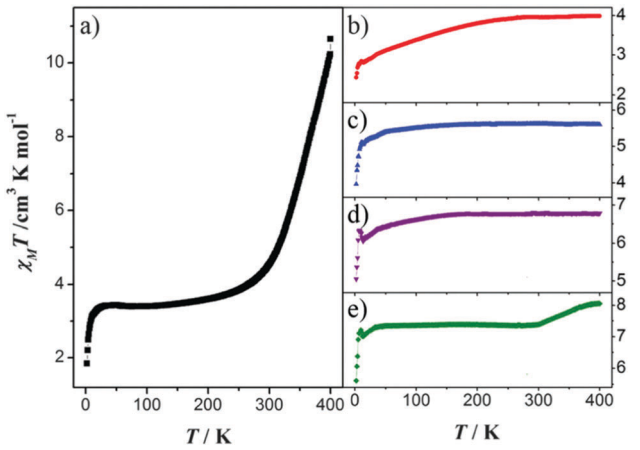

Fig. 45 $\chi_m T$ *vs.* T plots for cage $[Fe_4\mathbf{L78}_6](BF_4)_8$ (a) Fe^{II} cage (b) Ni^{II} cage (c) 20% Fe^{II} into Ni^{II} cage (d) 33% Fe^{II} content into Ni^{II} cage (e) 50% Fe^{II} content in Ni^{II} cage. Figure adapted, reproduced with permission from ref. 144. Copyright 2016 RSC.

or 17–37% HS when desolvated, and transition to 74–87% HS at 400 K (desolvated), with the LS state best stabilised when R = Cl.

The same group reported a $Fe^{II}_4\mathbf{L78}_6$ (Chart 12) cage exhibiting gradual and incomplete SCO. The $\chi_m T$ value at 400 K was 10.64 cm^3 K mol^{-1} which indicated about 88.7% of Fe(II) were HS. The SCO curve falls abruptly from 400 K to 300 K, then gradually from 300 to 10 K (Fig. 45a). They have also studied the effect of varying the Fe(II) content of a $Ni^{II}_4L_6$ cage on the SCO behaviour. Through SCSC transformations, they successfully manipulated the Fe(II) proportion in a colourless $Ni(II)_4$ cage from 20% (yellow) to 33% (red) and 50% (dark purple), which was confirmed *via* atomic absorption spectroscopy. The former two did not show any SCO, but at 50% Fe(II), the Ni_2Fe_2 cage showed a gradual transition at 300 K (Fig. 45e).[144]

Penta-, hexa- and octa-nuclear complexes

SCO has rarely been seen in Fe(II) supramolecular architectures with more than four metal centres, but this is an active area of research, and since 2009 this has been achieved in an Fe_6 "nanoball",[146] then in an Fe_5 "helical cluster" with a planar $[Fe^{II}_3(\mu_3\text{-O})]^{4+}$ core,[147] and in 2017 in a pair of Fe_8 cubes[45] (Fig. 2, **6A**, **5A** and **8A**, respectively), using the ligands shown in Chart 13.

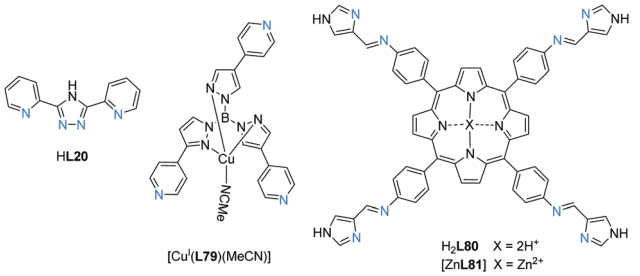

Chart 13 Ligands used in penta-, hexa- and octa-nuclear SCO-Fe(II) complexes (Fig. 2, **5A**, **6A** and **8A**).

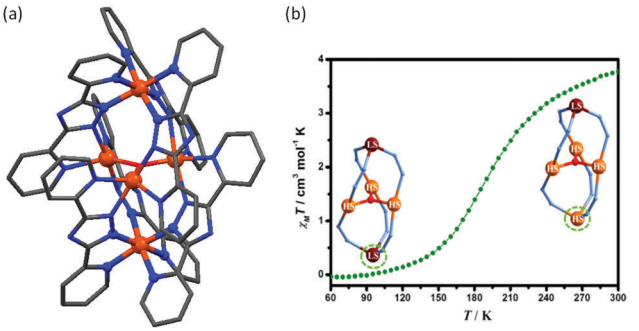

Fig. 46 (a) Structure of $[\{Fe^{II}(\mu\text{-}\mathbf{L20})_3\}_2Fe^{II}_3(\mu_3\text{-O})]$. (b) $\chi_M T$ plot for the single SCO-active site (Fe2, at the bottom in these images) in the pentanuclear cluster complex, $[\{Fe^{II}(\mu\text{-}\mathbf{L20})_3\}_2Fe^{II}_3(\mu_3\text{-O})][Fe^{II}_2(\mu\text{-Cl})(\mu\text{-}\mathbf{L20})(NCS)_4(H_2O)]\cdot 2H_2O\cdot C_2H_5OH$, after subtraction from the contribution of $[Fe^{II}_3(\mu_3\text{-O})]^{4+}$ core, LS $[FeL_3]^-$ and dinuclear counteranion. (b) Reproduced from reference with permission.[147] Copyright 2016 ACS.

The first SCO-active cluster helicate, $[\{Fe^{II}(\mu\text{-}\mathbf{L20})_3\}_2Fe^{II}_3(\mu_3\text{-O})][Fe^{II}_2(\mu\text{-Cl})(\mu\text{-}\mathbf{L20})(NCS)_4(H_2O)]$ (**HL20**, Chart 13), was reported by Tong and Ni and co-workers in 2016 (Fig. 46a).[147] Closely related cationic cluster helicates had already been reported by Kawata and Kaizaki and co-workers in 2006, where two LS triple stranded $[FeL_3]^-$ units wrapped a planar HS $[Fe_3(\mu_3\text{-O})]^{4+}$ core, but with different counter anion, NCS^-,[148] and in 2010 Oshio and co-workers varied the anions: the two apical $[FeL_3]^-$ units were LS in the case of NCS^-, ClO_4^-, I^- and HS in the case of $Fe^{III}_2(\mu\text{-O})Cl_6^{2-}$. But no SCO behaviour was observed with any of these complexes.[149]

Tong and Ni and co-workers instead crystallised this cationic pentanuclear cluster helicate by use of a complex dinuclear dianion, $[Fe^{II}_2(\mu\text{-Cl})(\mu\text{-}\mathbf{L20})(NCS)_4(H_2O)]^{2-}$, to induce SCO behaviour. In this modified cluster helicate, which again features a planar HS $[Fe^{II}_3(\mu_3\text{-O})]^{4+}$ core, the average Fe–N bond lengths (and Σ values), at 150 and 293 K, clearly showed that one of the two apical $[FeL_3]^-$ moieties was SCO-active (Fe2) whilst the other (Fe1) remained LS up to 300 K (Fig. 46b). All other Fe(II) centres, in the cluster and in the anion, remained HS. The Σ for two apical $[FeL_3]^-$ moieties, Fe1 changed from 60.9 to 63.7° and Fe2 changed from 65.8 to 93.7°, at 150 and 293 K respectively.

In 2009, Batten and co-workers reported the first SCO-active Fe_6 supramolecular architecture. The six Fe(II) centres are bridged by eight neutral tritopic tris-monodentate Cu(I) metalloligands, $\{Cu^I\mathbf{L79}(MeCN)\}$ (Chart 13), forming a Fe_6L_8 cluster which they termed a "nanoball", $[Fe^{II}_6(NCS)_{28/3}(MeCN)_{8/3}\{Cu^I\mathbf{L79}\text{-}(MeCN)\}_8](ClO_4)_{8/3}$.[146] The equatorial plane of each of the octahedral N_6-coordinated Fe(II) centres comprises four 4-pyridyl groups from four Cu(I) metalloligands, and the axial sites are occupied by either NCS or NCMe. The six Fe(II) ions are arranged octahedrally, so, along with the cubic arrangement of the eight Cu(I) ions, this forms a distorted rhombic dodecahedron with a diameter of *ca.* 3 nm (Fig. 47). The as-synthesised complex undergoes approximately a 50% HS to LS SCO in the solid state, which is switched off, reversibly, by MeCN solvent loss. Owing to the poor lattice packing of the nanoball, large voids between

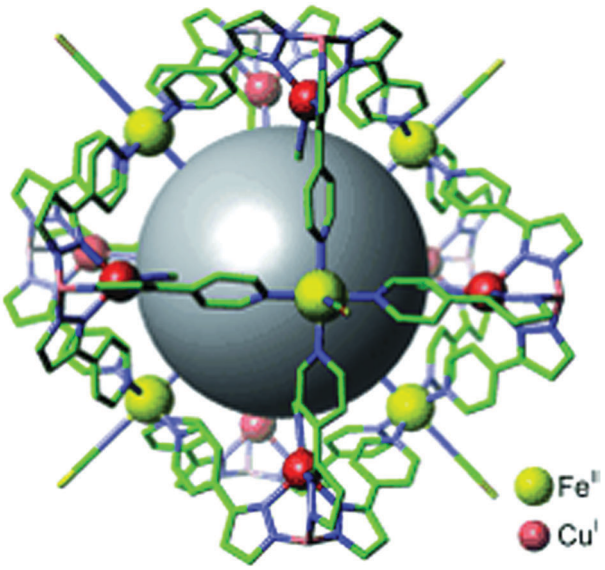

Fig. 47 $Fe_6[Cu^{I}\mathbf{L79}(MeCN)]_8$ shell of nanoball structure featuring eight Cu(I) metalloligands. Figure reproduced with permission from ref. 146. Stick colours: blue = nitrogen, green = carbon, yellow = sulphur, pink = boron. Copyright 2009 John Wiley and Sons.

complex cations were exploited for guest solvent molecule sorption/desorption, and this was found to tune the SCO properties. The same group went on to report the analogues with different anions, NCE^- (E = Se, BH_3) in 2012, *i.e.* $[Fe^{II}_6(NCSe)_{28/3}(MeCN)_{8/3}\{Cu^{I}\mathbf{L79}(MeCN)\}_8](ClO_4)_{8/3}$ and $[Fe^{II}_6(NCBH_3)_{28/3}(MeCN)_{8/3}\{Cu^{I}\mathbf{L79}(MeCN)\}_8](ClO_4)_{8/3}$.[150] These new family members, with $NCSe^-$ and $NCBH_3^-$ co-ligands, which provide stronger field strengths than NCS^-, did not change the geometry significantly but, as expected, increased the $T_{1/2}$ from 124 (NCS) to 162 (NCSe) to 173 K ($NCBH_3$). The authors also studied the LIESST effect on all three nanoballs and correlated the $T_{1/2}$ with T_{LIESST}. These nanoballs held the record for the largest nuclearity discrete Fe(II) complex to undergo SCO until 2017.

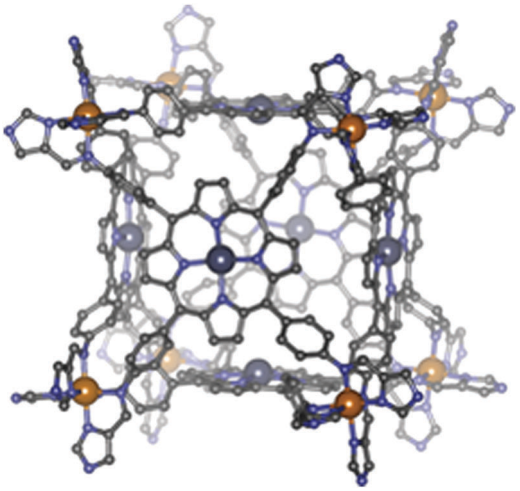

Fig. 48 $[Fe_8(Zn\mathbf{L81})_6]^{16+}$ cube structure featuring six face capping Zn(II) porphyrin metalloligands. Figure reproduced with permission from ref. 45. Copyright 2017 John Wiley and Sons.

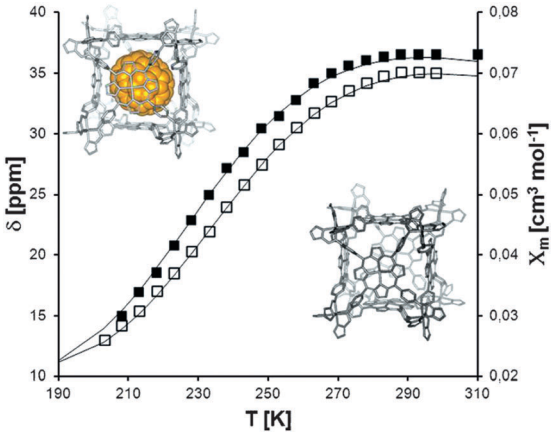

Fig. 49 VT-^{1}H NMR in [D_4] MeOH, empty squares: $[Fe_8(Zn\mathbf{L81})_6]^{16+}$ cube; filled square C70@$[Fe_8(Zn\mathbf{L81})_6]^{16+}$; black line calculated molar susceptibility χ_m based on the ideal solution model. Figure reproduced with permission from ref. 45. Copyright 2017 John Wiley and Sons.

In 2017, Lützen and co-workers reported two $[Fe_8L_6]^{16+}$ cubes, $[Fe_8(H_2\mathbf{L80})_6](CF_3SO_3)_{16}$ and $[Fe_8(Zn\mathbf{L81})_6](CF_3SO_3)_{16}$ which exhibit SCO in methanol solution.[45] The eight Fe(II) centres define the corners of the supramolecular cube, and six tetra-topic porphyrin ligands (Chart 13), where the porphyrins are all either uncoordinated ($H_2\mathbf{L80}$) or bound to Zn(II) (Zn**L81**), act as face-capping units (Fig. 48). Zn(II) coordination to the porphyrin faces of the Fe_8 cube appears to very slightly stabilise the HS state. Evans method studies from 298–203 K in deuterated-methanol solution revealed that the Zn-coordinated cube transitions from ~85% HS to ~30% HS (Fig. 49), while the cube without Zn(II) transitions from ~80% HS to ~15% HS. In a nice example of guest influence on SCO, encapsulation of C_{70}, facilitated by the appropriately sized internal cavity, was found to stabilise the HS state and lowered the $T_{1/2}$ of the solution based SCO by 15 K and 20 K for the Zn and Zn-free Fe_8 cubes respectively.

Summary

We have reviewed all 79 of the new discrete polynuclear SCO-active Fe(II) complexes reported between 2012 to February 2018, as well as selected examples from before then, which brings the total to 127 complexes. Of these 127 complexes, 54% are dinuclear, 10% trinuclear, 31% tetranuclear, and the remaining 5% are penta, hexa and octanuclear (Fig. 50 and 51).

For the design of Fe(II) SCO-active complexes, the first and foremost consideration is providing the right ligand field strength through careful choice of donor groups, and this also applies when constructing polynuclear architectures. As for mononuclear Fe(II) SCO-active materials, most commonly a N_6 coordination sphere is targeted, by the use of exclusively N-donor ligands. Of the 93 ligand and 8 bridging anion designs featured here, only 11 of them provide anything other than purely N-donors: three **PSRT** ligands (N_4S_2 coordination sphere), ligand $\mathbf{L66}^-$ (N_4O_2), ligand **HL22** (N_5P) and anions **A2–A5** (N_5O, Chart 7), μ-NCS (N_5S), and μ-CN^- (N_4C_2) feature

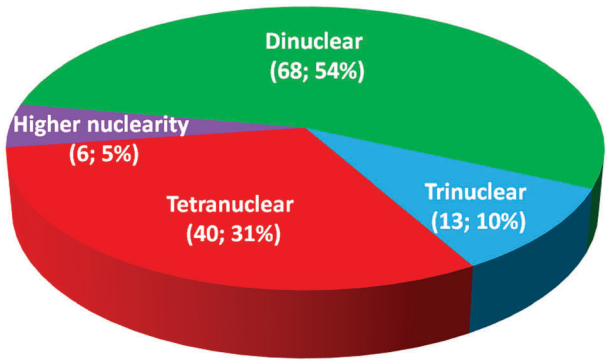

Fig. 50 Distribution of the 127 discrete polynuclear Fe(II) SCO-active complexes reviewed herein, as a function of nuclearity.

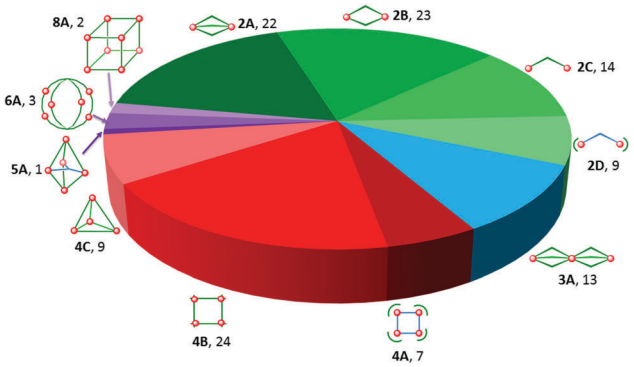

Fig. 51 The distribution of the 127 SCO complexes studied in this review across the different categories from dinuclear (**2A** triply bridged, **2B** doubly bridged, **2C** single bridged, **2D** anion bridged), to trinuclear (**3A** triply triazole bridged), to tetranuclear (**4A** squares, **4B** grids, **4C** tetrahedral cages), to pentanuclear (**5A**), to hexanuclear (**6A** 'nanoball') to octanuclear cube (**8A**).

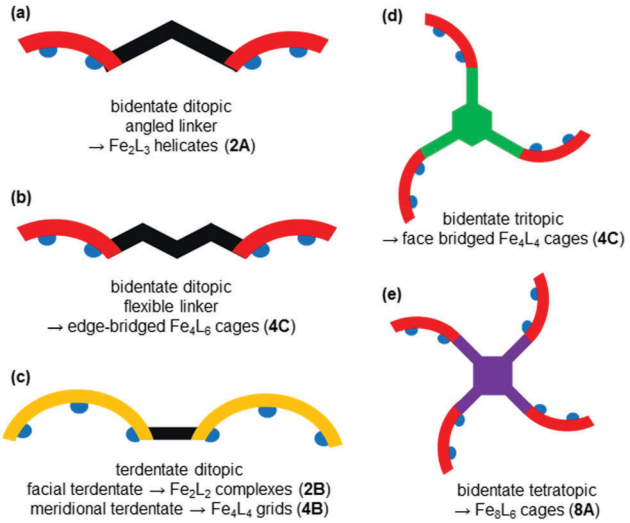

Fig. 52 Examples of ligand designs which provide the right number and topology of binding pockets, each with appropriate denticity, for the controlled self-assembly of discrete polynuclear Fe(II) complexes.

some S, O, P, or C donor atoms. Amongst the types of N-donor moieties, azoles feature strongly across a range of architectures, with them being incorporated into 60 of the 93 designer ligands, including those that generated the numerous examples of simple triply-triazole-bridged dinuclear and trinuclear SCO-active Fe(II) complexes (Charts 1 and 9).

Of the 93 designer ligands presented here, 55 provide all of the donor atoms to the Fe(II) centres (no co-ligands are coordinated) in the polynuclear architectures. These ligands are constructed to have a particular number of bi- or tri-dentate binding pockets that are arranged carefully relative to each other to predictably result in the self-assembly of the desired architecture (Fig. 52). Specific examples include ditopic ligands with bidentate pockets (bis-bidentate), with a central linker which directs the angle of the two pockets (**L8–L16**), to give dinuclear Fe_2L_3 helicates (Fig. 52a). When the linker is flexible (**L75–L78**), such ligands can instead generate edge-bridged tetranuclear Fe_4L_6 tetrahedral cages (Fig. 52b). Carefully designed ditopic-tridentate ligands (Fig. 52c) result in either (a) dinuclear Fe_2L_2 complexes, in the case of flexible facially coordinating pockets (**PMRT** and **PSRT** families, **PMTD**, **PMOD**, **L17**, **L18**), or (b) tetranuclear Fe_4L_4 grids, all but one (**L66**$^-$, O^- bridge) featuring heterocycle-bridged, meridionally coordinated, binding pockets (**L50–L70**). Moving up another level of complexity, tritopic-bidentate (tris-bidentate) ligands (**L71–L74**) can be used to generate face-capped tetranuclear Fe_4L_4 tetrahedral cages (Fig. 52d). Finally, taking this to the maximum level of complexity reported to date, the first examples of octanuclear SCO-active complexes were generated using designer tetratopic-bidentate ligands (H_2**L80**, Zn**L81**) to form face-bridged Fe_8L_6 cubes (Fig. 52e).

It is worth noting that amongst these 55 designer ligands, that the 19 which provide bidentate pockets all generate 5-membered chelate rings, and comprise either azole-imine (17 ligands; 22 complexes) or azole-pyridine (2 ligands; 5 complexes) moieties (Fig. 53) – so clearly the combination of three such azole-imine/pyridine pockets around Fe(II) is a winner for providing about the right ligand field to support SCO.

Similarly, out of these 55 designer ligands, 35 provide tridentate pockets, all of which generate a pair of fused 5-membered chelate rings (Fig. 54). These 35 poly-tridentate ligands all comprise either (a) azole-amine–pyridine (9 ligands) or azole-thioether–pyridine (3 ligands) binding facially (Fig. 54a) to give dinuclear **PMRT**-like complexes, or (b), with the exception of oxygen-bridging **L66**$^-$, a combination of three conjugated azines and/or azoles (11 ligands) or two azines or azine/azole joined by a conjugated central imine (12 ligands), all of which bind meridionally to give Fe_4L_4 grids (Fig. 54b). So clearly the coordination of two such pockets, heterocycle-imine/amine/thioether/pyridine-heterocycle, provides about the right ligand field to support SCO at Fe(II).

The remaining ligand of this group of 55 designer ligands is the unique **L25** (Chart 6), which is bis-hexadentate and provides all 12 N-donor atoms to two Fe(II) centres in an Fe_2L complex.

On the other hand, of the 38 ligands designed to work in conjunction with co-ligands, 28 of the resulting complexes involve NCE anions (NCS, NCSe, $NCBH_3$, **dca**$^-$) completing

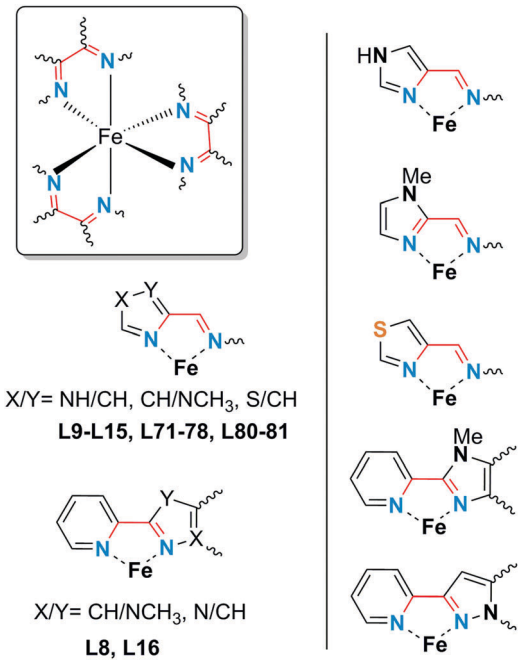

Fig. 53 Binding motifs common to the 19 bidentate ligands out of the 55 designer ligands that provide all of the donors to the SCO-active octahedral Fe(II) centres (no co-ligands bound) – by binding of three identical bidentate pockets (box). Right: The 5 specific binding moieties employed in all 19 of these polytopic ligands.

the coordination sphere and helping to provide the right overall field strength for SCO at Fe(II). Overall, 22% of the 127 complexes reviewed herein contain NCE^- anions as co-ligands, so it is clear that the use of NCE co-ligands remains another key way to obtain ligand fields that are in the right ballpark to promote the formation of SCO-active Fe(II) complexes.

Another factor that must be taken into consideration is the degree of distortion of the Fe(II) centres away from perfect octahedral geometry, as this also modifies the ligand field. There are a number of ways to probe and quantify this distortion. Here we focus on the octahedral distortion parameter Σ, the sum of the deviations from 90° of the 12 *cis* angles, and the SChM,[151–154] the continuous shape measure of the degree of distortion from an ideal geometry, here octahedral (Tables 1–11 and Fig. 55–59; see also the ESI†). As expected, in general the Fe(II) centres are less distorted when in the LS state than when in the HS state. Another key finding from this analysis of the structurally characterised discrete polynuclear complexes reviewed herein is that for the 55 designer ligands which provide all of the donors to the Fe(II) centres, the octahedral distortion is generally higher than for the 38 ligands which are designed to work in conjunction with co-ligands. This is perhaps not surprising, as the latter systems will have greater flexibility due to involving a mixture of ligands, often including some monodentate ligands. Clearly the same arguments, regarding the degree of distortion away from octahedral being to some extent a function of whether the metal ion is coordinated by (a) only polydentate ligands or (b) a mixture of ligands including monodentate, also apply to non SCO-active complexes – of iron(II) or indeed other metal ions.

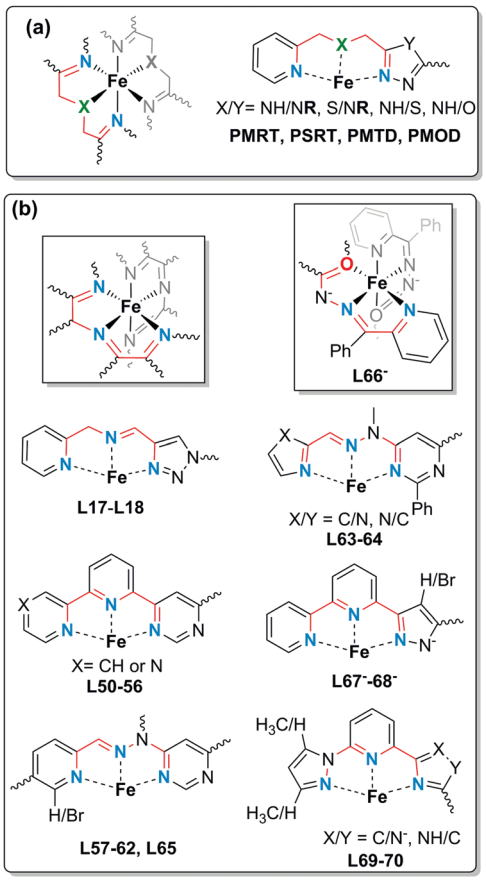

Fig. 54 Binding motifs common to the 35 tridentate ligands, out of the 55 designer ligands that provide all of the donors to the SCO-active octahedral Fe(II) centres (no co-ligands bound) by binding of two identical tri-dentate pockets in either (a) facial or (b) meridional binding mode.

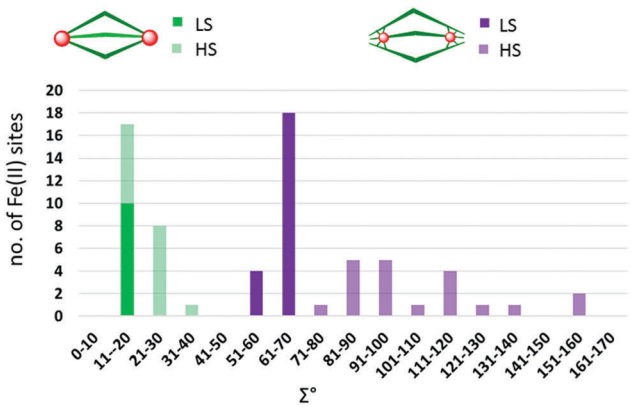

Fig. 55 Distribution of octahedral distortion parameter, Σ (°), for the Fe(II) centres in dinuclear complexes of type **2A** (Fig. 2): triply triazole bridged $[Fe_2L_5(NCE)_4]$ (green) and triple helicates $[Fe_2L_3]$ (violet). Dark colour = LS; light colour = HS.

Examples of this variation, within SCO active iron(II) complexes, of the octahedral distortion as a function of complex type, are clearly seen in comparing the triply bridged dinuclear complexes (**2A**), which fall into two distinct categories: triply-triazole bridged with co-ligands $[Fe_2L_5(NCE)_4]$ (Fig. 3 and Chart 1) for

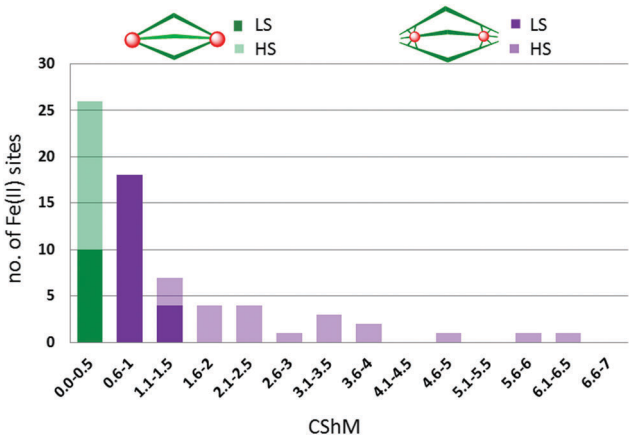

Fig. 56 Distribution of continuous shape measured value, CShM, of octahedral distortion, for the Fe(II) centres in dinuclear complexes of type **2A** (Fig. 2): triply triazole bridged $[Fe_2L_5(NCE)_4]$ (green) and triple helicates $[Fe_2L_3]$ (violet). Dark colour = LS; light colour = HS.

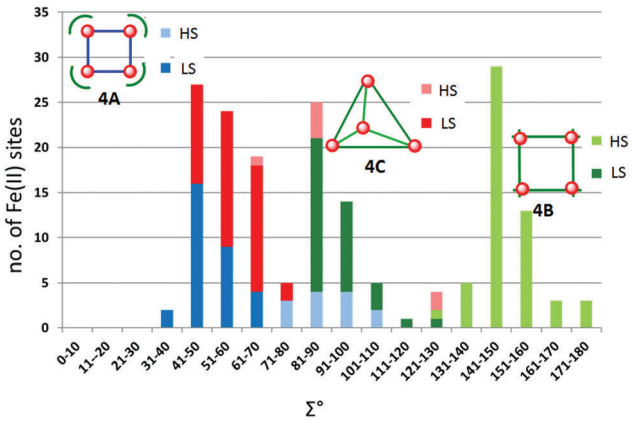

Fig. 57 Distribution of octahedral distortion parameter, Σ (°), for the Fe(II) centres in tetranuclear complexes: types **4A** squares (blue), **4B** grids (green) and **4C** tetrahedral cages (red) (Fig. 2).

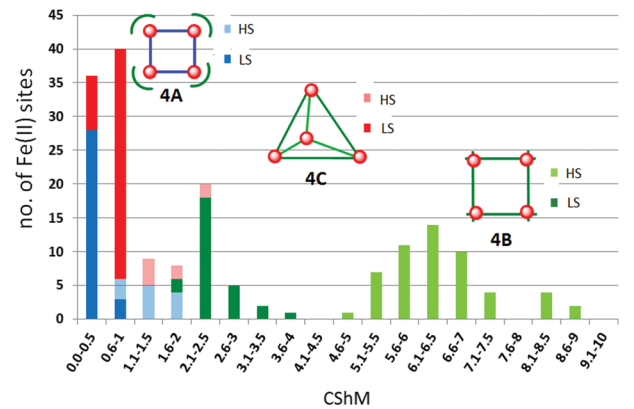

Fig. 58 Distribution of continuous shape measured value, CShM, of octahedral distortion, for the Fe(II) centres in tetranuclear complexes: types **4A** squares (blue), **4B** grids (green) and **4C** tetrahedral cages (red) (Fig. 2).

which Σ is consistently lower (Table 1) than it is for the triple helicates $[Fe_2L_3]$ (Fig. 6–9, Chart 2 and Tables 2–4), as is

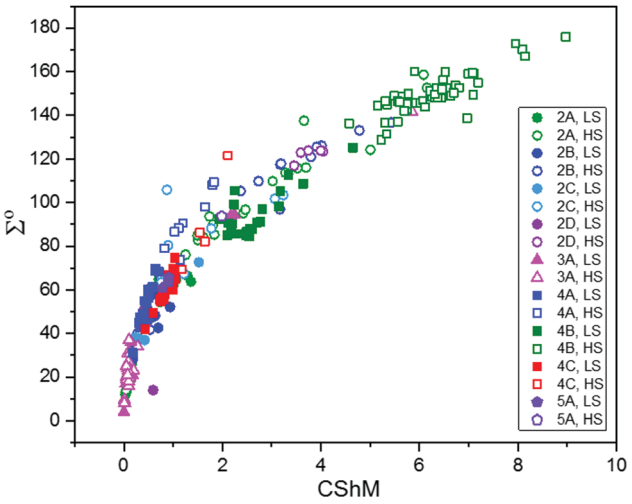

Fig. 59 Comparison of two measures of octahedral distortion, Σ (°) and CShM, for structurally characterised discrete polynuclear SCO-active Fe(II) complexes reviewed herein (see also ESI,† Table S1).

illustrated in Fig. 55. Indeed the Σ values for the Fe(II) centres in the triply-triazole bridged complexes (Fig. 55, green) are in the range 11–20° for LS and 11–40° for HS, with the octahedral geometry close to ideal in both cases (CShM < 0.5, Fig. 56, green). In contrast, for Fe_2L_3 helicates, the Σ values are far higher, at 51–70° for LS *versus* 71–160° for HS (Fig. 55, violet), with correspondingly high CShM values (LS = 0.6–1.5, HS = 1.1–6.5; Fig. 56, purple).

Similarly, the Fe(II) centres in tetranuclear squares with co-ligands (Fig. 2, **4A**) have smaller Σ values (Fig. 57, blue) than those in grids (Fig. 2, **4B**, Fig. 57 green), as the latter systems comprise just four ligands that provide all of the 24 donors to the four Fe(II) centres. Interestingly, the tetranuclear tetrahedral cages (Fig. 2, **4C**, Fig. 57 red) also comprise a single type of ligand which provides all of the donors, and yet the distortions are smaller than in the grids, falling in a similar range to those seen for the squares (Fig. 57 blue). Specifically, in the LS state, the Fe(II) centres in the squares and cages have consistently much lower Σ (31–70° and 43–75° respectively, Fig. 57 dark blue and red) and CShM (0.183–0.826 and 0.433–1.035 respectively, Fig. 58 dark blue and red) values, than in the grids (Σ = 84–125°, Fig. 57 dark green; CShM = 1.935–5.686; Fig. 58, dark green). Indeed the Σ values for the LS grids (Fig. 57, dark green) are in the same range as for the HS squares (Σ = 79–109°, Fig. 57 light blue).

The highly constrained coordination environment imposed by the four bis-terdentate ligands in the Fe_4L_4 grids, as evidenced by large Σ and CShM values, may be providing a barrier to complete SCO to the [4LS] state, with a regular octahedral LS coordination environment for all four of the Fe(II) centres perhaps geometrically impossible in some cases. In most of the grids reviewed here, the fully LS state is inaccessible, with only the grids of **L54**, **L65**, and **L70** (only the *trans* isomer, which is unique among the grids reviewed here) being structurally characterised in the [4LS] state. On the other hand, all of the square complexes, which contain co-ligands and hence a more

readily accessible regular octahedral geometry, have been structurally characterised as [4LS]. For the tetrahedral cages, all but two complexes, $[Fe^{II}_4(\mathbf{L74})_4](BF_4)_4{\cdot}16CH_3CN$ and $[Fe^{II}_4(\mathbf{L71})_4](BF_4)_8{\cdot}14.75CH_3CN{\cdot}4.5C_6H_6{\cdot}3H_2O$, have been observed in the [4LS] state by X-ray crystallography, despite having all donors to the Fe(II) centres provided by just the one type of ligand. The key difference, however, for the tetrahedral cages is that the octahedral environment at the Fe(II) centres is completed by three bidentate donors, unlike in the grid complexes where just two terdentate donors coordinate to each Fe(II) centre.

Unsurprisingly a positive, but not linear, correlation is observed between these two measures of distortion, Σ and CShM (Fig. 59 and Table S1, ESI†). It is interesting to note that when the distortion away from octahedral is relatively small, Σ is perhaps a more informative measure than the CShM. Indeed it is pertinent to note that a CShM value of just 2 corresponds to a Σ value of approximately 90°. Finally, as expected, regardless of the measure used, Σ or CShM, lower distortion parameters are observed for the LS Fe(II) centres (Fig. 59, solid points) than for the HS Fe(II) centres (Fig. 59, hollow points).

Generally, the Fe···Fe distances in the helicates vary from 9–12 Å, except in case of **L14** and **L15** (Chart 2), where distance is far lower, ~4 Å, because of the short NN bridge between them and the resultant twist of the ligand to bind, which also leads to a very high distortion Σ and CShM for the Fe(II) centres (158.5° and 6.084, respectively, Table S1, ESI†). The Fe_4 grids have a very rigid geometry around the metal centres and their Fe···Fe distances (4–7 Å) are much lower than those seen in the Fe_4 tetrahedral cages (with face capping ligands, 11–15 Å; edge capping ligands 9–11 Å). This is mostly because the bis-terdentate ligands of the grids also provide a short bridge (*e.g.* pyrimidine-bridge) between the two binding pockets and hence Fe(II) centres, whereas for the cages, longer, non-coordinating linkers (*e.g.* 1,3,5-triphenylbenzene) are utilised.

An important feature of many of the SCO-active polynuclear architectures reviewed here is the presence of a guest-accessible internal cavity which may be exploited for SCO tuning and/or guest sensing. The effects on SCO of guest inclusion into the cavity in Fe_2L_3 helicates, Fe_4L_4 cages, and Fe_8L_6 cubes have been probed in a handful of studies. The largest of the internal cavities to date occur in the Fe_8L_6 cubes, where the uptake of the large C_{70} into the 1300 $Å^3$ cavity tuned the SCO $T_{1/2}$ by 15–20 K in the solution phase. For the face-capped Fe_4L_4 cages, smaller internal cavities of 61–183 $Å^3$ are reported, and in the case of $[Fe_4(\mathbf{L73})_4](OTf)_8$ inclusion of the small guests Br^- and CS_2 tuned the SCO $T_{1/2}$ by 8–12 K in the solution phase. Interestingly, the smallest of the cavities probed for guest tuning of SCO, the 28–33 $Å^3$ cavities in the $\{X@[Fe_2(\mathbf{L16})_3]\}X(PF_6)_2$ (X = Cl^- or Br^-) helicates, had the largest observed shift in $T_{1/2}$. Upon changing the encapsulated Cl^- to the larger Br^- anion, the $T_{1/2}$ in the solid state was decreased by 40 K. Furthermore, the position of the halide inside the small cavity was seen to greatly affect the nature of the SCO, with half *vs.* full SCO observed when the halide is positioned closer to one Fe(II) centre *vs.* equidistant to both Fe(II) centres. Clearly, large, easily observable effects on the SCO properties of these complexes can be induced by the encapsulation of various guests, and as more examples of large cage-like SCO-active complexes are developed one can anticipate a wealth of host–guest chemistry, including sensing applications, being reported in the near future.

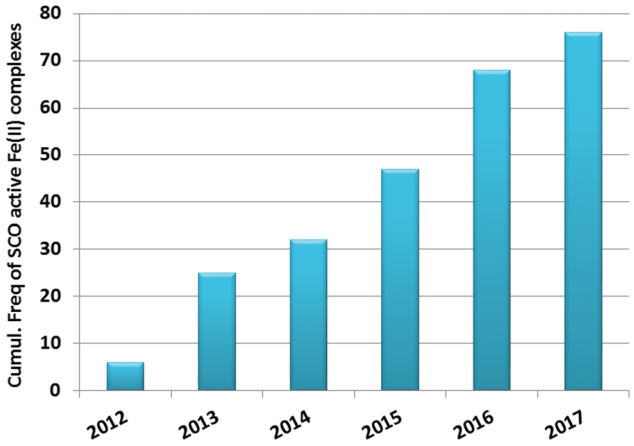

Fig. 60 Increasing number of discrete di- to poly-nuclear SCO-active Fe(II) complexes reported in the period from 2012 to 2017 (76 in total). Our previous review[35] covered the 68 examples reported 2004–2011.

Finally, the number of discrete polynuclear SCO-active Fe(II) complexes has increased significantly over the period from 2012 to 2017 (Fig. 60): the 76 new examples reported more than doubles the number reported in the literature, 68, over the period 2004–2011 covered by our previous review.[35]

Concluding remarks

By applying supramolecular self-assembly strategies,[43,58,155–158] and linking multiple donor pockets of the right ligand field strength and denticity into carefully structured ligands (Fig. 52), chemists have created a wealth of SCO-active discrete polynuclear Fe(II) complexes, ranging to date from dinuclear to octanuclear. The development of such complexes is a flourishing field, as illustrated by the fact that the 8 years from 2004–2011, 68 complexes were reported, and in the 7 subsequent years another 76 were reported. The architectural diversity of these complexes has also expanded considerably since 2011, with the first examples of SCO-active tetranuclear cages reported in 2013, and then a new record nuclearity for a discrete SCO complex was set in 2017 when the first examples of SCO-active octanuclear cube cages were reported. These trends are likely to continue, with many more reports of SCO-active discrete supramolecular architectures anticipated.

Covalently linking Fe(II) centres into polynuclear architectures has led to access to multistep SCO with stable intermediate spin states, *e.g.* [HS–LS], which opens up the possibility of multi-state molecular switches. In some cases linking SCO-appropriate binding pockets has led to more abrupt and even hysteretic SCO being observed in comparison to mononuclear analogues of the same immediate coordination environment. In many cases, the polymetallic architectures are highly strained, with steric and intermolecular crystal packing or solvent interactions often

dominating the SCO properties. In other cases, less strained ligands in same family induced different SCO behaviour through very small modification in ligand or counter-anion/solvent molecules.

Whilst a number of winning ligand design features for inducing SCO at Fe(II) are identified in the previous section (*e.g.* Fig. 53 and 54), it remains very difficult to predictably fine-tune or control SCO behaviour (including $T_{1/2}$ or hysteresis) in advance of synthesis and characterisation.[159–163] The effects of intermolecular crystal packing and/or counter anion/solvent interactions can dominate, over ligand field effects, the SCO properties in the solid state.

Solution state studies[13–16,145] are of increasing prevalence and promise to facilitate the development of more detailed understanding of the ligand field effects, as packing effects no longer apply. Solution studies are also of key importance in the case of SCO-active systems that can recognise guests, such as cages, as modifications in the SCO behaviour could facilitate guest sensing. But solution studies warrant two notes of caution: (a) the potential for speciation to be an issue must be addressed, otherwise it could confound such studies, and (b) the influence of solvent choice on the SCO should also be explored.[164] Nevertheless, the solution stability of many of these supramolecular assemblies is such that exploiting the internal cavities of SCO-active helicates, cages and new types of discrete supramolecules for guest sensing applications is another rapidly evolving area of interest in this field.

Conflicts of interest

There are no conflicts to declare.

Acknowledgements

We thank the University of Otago (PhD scholarships to RWH and SS) for supporting this research.

References

1 P. Gütlich and H. A. Goodwin, *Top. Curr. Chem.*, 2004, **233**, 1–47.
2 A. Bousseksou, G. Molnár, L. Salmon and W. Nicolazzi, *Chem. Soc. Rev.*, 2011, **40**, 3313–3335.
3 M. A. Halcrow, *Spin-Crossover Materials: Properties and Applications*, John Wiley & Sons, Ltd, Chichester, 1st edn, 2013.
4 P. Gütlich, A. B. Gaspar and Y. Garcia, *Beilstein J. Org. Chem.*, 2013, **9**, 342–391.
5 H. J. Shepherd, I. A. Gural'skiy, C. M. Quintero, S. Tricard, L. Salmon, G. Molnár and A. Bousseksou, *Nat. Commun.*, 2013, **4**, 2607.
6 S. Brooker, *Chem. Soc. Rev.*, 2015, **44**, 2880–2892, and front cover feature.
7 K. Senthil Kumar and M. Ruben, *Coord. Chem. Rev.*, 2017, **346**, 176–205.
8 O. Kahn, *Molecular Magnetism*, VCH Publishers Inc., New York, 1993.
9 A. Hauser, *Top. Curr. Chem.*, 2004, **233**, 49–58.
10 M. H. Klingele, B. Moubaraki, J. D. Cashion, K. S. Murray and S. Brooker, *Chem. Commun.*, 2005, 987–989 and front cover feature.
11 J. A. Kitchen, N. G. White, C. Gandolfi, M. Albrecht, G. N. L. Jameson, J. L. Tallon and S. Brooker, *Chem. Commun.*, 2010, **46**, 6464–6466.
12 H. L. C. Feltham, C. Johnson, A. B. S. Elliot, K. C. Gordon, M. Albrecht and S. Brooker, *Inorg. Chem.*, 2015, **54**, 2902–2909.
13 D. F. Evans, *J. Chem. Soc.*, 1959, 2003–2005.
14 B. Weber and F. A. Walker, *Inorg. Chem.*, 2007, **46**, 6794–6803.
15 B. Weber, E. S. Kaps, J. Obel, K. Achterhold and F. G. Parak, *Inorg. Chem.*, 2008, **47**, 10779–10787.
16 R. W. Hogue, C. P. Lepper, G. B. Jameson and S. Brooker, *Chem. Commun.*, 2018, **54**, 172–175.
17 P. Gütlich, A. Bhattacharjee, M. Seredyuk and A. B. Gaspar, *Hyperfine Interact.*, 2009, **189**, 3–19.
18 Y. Garcia, F. Robert, A. D. Naik, G. Zhou, B. Tinant, K. Robeyns, S. Michotte and L. Piraux, *J. Am. Chem. Soc.*, 2011, **133**, 15850–15853.
19 M. J. Murphy, K. A. Zenere, F. Ragon, P. D. Southon, C. J. Kepert and S. M. Neville, *J. Am. Chem. Soc.*, 2017, **139**, 1330–1335.
20 O. Roubeau, M. Castro, R. Burriel, J. G. Haasnoot and J. Reedijk, *J. Phys. Chem. B*, 2011, **115**, 3003–3012.
21 M. Sorai and S. Seki, *J. Phys. Chem. Solids*, 1974, **35**, 555–570.
22 O. Kahn, J. Kröber and C. Jay, *Adv. Mater.*, 1992, **4**, 718–728.
23 O. Kahn and C. J. Martinez, *Science*, 1998, **279**, 44–48.
24 J. Krober, E. Codjovi, O. Kahn, F. Groliere and C. Jay, *J. Am. Chem. Soc.*, 1993, **115**, 9810–9811.
25 J. A. Real, A. B. Gaspar, V. Niel and M. C. Muñoz, *Coord. Chem. Rev.*, 2003, **236**, 121–141.
26 M. A. Halcrow, *Chem. Soc. Rev.*, 2011, **40**, 4119–4142.
27 O. Kahn, L. Sommier and E. Codjovi, *Chem. Mater.*, 1997, **9**, 3199–3205.
28 E. Codjovi, L. Sommier, O. Kahn and C. Jay, *New J. Chem.*, 1996, **20**, 503–505.
29 J. Kroeber, J.-P. Audiere, R. Claude, E. Codjovi, O. Kahn, J. G. Haasnoot, F. Groliere, C. Jay, A. Bousseksou, J. Linares, F. Varret and A. Gonthier-Vassal, *Chem. Mater.*, 1994, **6**, 1404–1412.
30 A. Grosjean, N. Daro, B. Kauffmann, A. Kaiba, J.-F. Létard and P. Guionneau, *Chem. Commun.*, 2011, **47**, 12382–12384.
31 K. S. Murray, *Eur. J. Inorg. Chem.*, 2008, 3101–3121.
32 J. A. Real, A. B. Gaspar, M. C. Muñoz, P. Gütlich, V. Ksenofontov and H. Spiering, *Top. Curr. Chem.*, 2004, **233**, 167–193.
33 Y. Garcia, V. Niel, M. C. Muñoz and J. A. Real, *Top. Curr. Chem.*, 2004, **233**, 229–258.
34 A. B. Gaspar, M. C. Muñoz and J. A. Real, *J. Mater. Chem.*, 2006, **16**, 2522–2533.

35 J. Olguín and S. Brooker, in *Spin-Crossover Materials: Properties and Applications*, ed. M. A. Halcrow, John Wiley & Sons, Ltd, 1st edn, 2013, pp. 77–120.
36 J.-F. Létard, P. Guionneau and L. Goux-Capes, *Top. Curr. Chem.*, 2004, **235**, 221–249.
37 J. A. Real, H. Bolvin, A. Bousseksou, A. Dworkin, O. Kahn, F. Varret and J. Zarembowitch, *J. Am. Chem. Soc.*, 1992, **114**, 4650–4658.
38 B. Schneider, S. Demeshko, S. Neudeck, S. Dechert and F. Meyer, *Inorg. Chem.*, 2013, **52**, 13230–13237.
39 B. Schneider, S. Demeshko, S. Dechert and F. Meyer, *Angew. Chem., Int. Ed.*, 2010, **49**, 9274–9277.
40 I. Amlani, A. O. Orlov, G. Toth, G. H. Bernstein, C. S. Lent and G. L. Snider, *Science*, 1999, **284**, 289–291.
41 C. S. Lent, *Science*, 2000, **288**, 1597–1599.
42 M. Ruben, J. Rojo, F. J. Romero-Salguero, L. H. Uppadine and J.-M. Lehn, *Angew. Chem., Int. Ed.*, 2004, **43**, 3644–3662.
43 J. G. Hardy, *Chem. Soc. Rev.*, 2013, **42**, 7881–7899.
44 A. B. Gaspar, M. C. Munoz and J. A. Real, *J. Mater. Chem.*, 2006, **16**, 2522–2533.
45 N. Struch, C. Bannwarth, T. K. Ronson, Y. Lorenz, B. Mienert, N. Wagner, M. Engeser, E. Bill, R. Puttreddy, K. Rissanen, J. Beck, S. Grimme, J. R. Nitschke and A. Lützen, *Angew. Chem., Int. Ed.*, 2017, **56**, 4930–4935.
46 S. B. Erenburg, N. V. Bausk, V. A. Varnek and L. G. Lavrenova, *J. Magn. Magn. Mater.*, 1996, **157-158**, 595–596.
47 O. Roubeau, *Chem. – Eur. J.*, 2012, **18**, 15230–15244; L. G. Lavrenova and O. G. Shakirova, *Eur. J. Inorg. Chem.*, 2013, 670–682.
48 X. Cheng, Q. Yang, C. Gao, B.-W. Wang, T. Shiga, H. Oshio, Z.-M. Wang and S. Gao, *Dalton Trans.*, 2015, **44**, 11282–11285.
49 J.-L. Wang, Q. Liu, Y.-S. Meng, H. Zheng, H.-L. Zhu, Q. Shi and T. Liu, *Inorg. Chem.*, 2017, **56**, 10674–10680.
50 O. Roubeau, P. Gamez and S. J. Teat, *Eur. J. Inorg. Chem.*, 2013, 934–942.
51 X. X. Wu, Y. Y. Wang, P. Yang, Y. Y. Xu, J. Z. Huo, B. Ding, Y. Wang and X. Wang, *Cryst. Growth Des.*, 2014, **14**, 477–490.
52 B. Ding, Y. Y. Liu, Y. Wang, J.-G. Ma, Z. Niu, W. Shi and P. Cheng, *Inorg. Chem. Commun.*, 2013, **31**, 44–48.
53 J. J. A. Kolnaar, M. I. deHeer, H. Kooman, A. L. Spek, G. Schmitt, V. Ksenofontov, P. Gütlich, J. G. Haasnoot and J. Reedijk, *Eur. J. Inorg. Chem.*, 1999, 881–886.
54 A. Williams, *Chem. – Eur. J.*, 1997, **3**, 15–19.
55 C. Piguet, G. Bernadinelli and G. Hopfgarter, *Chem. Rev.*, 1997, **97**, 2005–2062.
56 C. Piguet, M. Borkovec, J. Hamacek and K. Zeckert, *Coord. Chem. Rev.*, 2005, **249**, 705–726.
57 C. R. K. Glasson, L. F. Lindoy and G. V. Meehan, *Coord. Chem. Rev.*, 2008, **252**, 940–963.
58 A. J. McConnell, C. S. Wood, P. P. Neelakandan and J. R. Nitschke, *Chem. Rev.*, 2015, **115**, 7729–7793.
59 M. J. Hannon and L. J. Childs, *Supramol. Chem.*, 2004, **16**, 7–22.
60 M. Albrecht, *Chem. Rev.*, 2001, **101**, 3457–3498.
61 M. Darawsheh, L. A. Barrios, O. Roubeau, S. J. Teat and G. Aromí, *Chem. – Eur. J.*, 2016, **22**, 8635–8645.
62 S. Goetz and P. E. Kruger, *Dalton Trans.*, 2006, 1277–1284.
63 F. Cui, S. Li, C. Jia, J. S. Mathieson, L. Cronin, X.-J. Yang and B. Wu, *Inorg. Chem.*, 2012, **51**, 179–187.
64 J. Xu, T. N. Parac and K. N. Raymond, *Angew. Chem., Int. Ed.*, 1999, **38**, 2878–2882.
65 C. R. K. Glasson, G. V. Meehan, C. A. Motti, J. K. Clegg, P. Turner, P. Jensen and L. F. Lindoy, *Dalton Trans.*, 2011, **40**, 12153–12159.
66 L. J. Charbonnière, A. F. Williams, C. Piguet, G. Bernardinelli and E. Rivara-Minten, *Chem. – Eur. J.*, 1998, **4**, 485–493.
67 F. Tuna, M. R. Lees, G. J. Clarkson and M. J. Hannon, *Chem. – Eur. J.*, 2004, **10**, 5737–5750.
68 Y. Sunatsuki, R. Kawamoto, K. Fujita, H. Maruyama, T. Suzuki, H. Ishida, M. Kojima, S. Iijima and N. Matsumoto, *Inorg. Chem.*, 2009, **48**, 8784–8795.
69 D. Pelleteret, R. Clérac, C. Mathonière, E. Harte, W. Schmitt and P. E. Kruger, *Chem. Commun.*, 2009, 221–223.
70 S. Yukinari, M. Hisashi, F. Kunihiro, S. Takayoshi, K. Masaaki and M. Naohide, *Bull. Chem. Soc. Jpn.*, 2009, **82**, 1497–1505.
71 A. Craze, N. Sciortino, M. Badbhade, C. Kepert, C. Marjo and F. Li, *Inorganics*, 2017, **5**, 62.
72 L. Li, A. R. Craze, R. Akiyoshi, A. Tsukiashi, S. Hayami, O. Mustonen, M. M. Bhadbhade, S. Bhattacharyya, C. E. Marjo, Y. Wang, L. F. Lindoy, J. R. Aldrich-Wright and F. Li, *Dalton Trans.*, 2018, **47**, 2543–2548.
73 S. G. Telfer, B. Bocquet and A. F. Williams, *Inorg. Chem.*, 2001, **40**, 4818–4820.
74 Y. Garcia, M. Grunert, S. Reiman, O. van Campenhoudt and P. Gütlich, *Eur. J. Inorg. Chem.*, 2006, 3333–3339.
75 R. J. Archer, C. S. Hawes, G. N. L. Jameson, V. McKee, B. Moubaraki, N. F. Chilton, K. S. Murray, W. Schmitt and P. E. Kruger, *Dalton Trans.*, 2011, **40**, 12368–12373.
76 H. Hagiwara, T. Tanaka and S. Hora, *Dalton Trans.*, 2016, **45**, 17132–17140.
77 S. Hora and H. Hagiwara, *Inorganics*, 2017, **5**, 49.
78 M. H. Klingele, B. Moubaraki, K. S. Murray and S. Brooker, *Chem. – Eur. J.*, 2005, **11**, 6962–6973.
79 C. M. Grunert, S. Reiman, H. Spiering, J. A. Kitchen, S. Brooker and P. Gütlich, *Angew. Chem., Int. Ed.*, 2008, **47**, 2997–2999, and front cover feature.
80 A. Bhattacharjee, V. Ksenofontov, J. A. Kitchen, N. G. White, S. Brooker and P. Gütlich, *Appl. Phys. Lett.*, 2008, **92**, 174104.
81 J. A. Kitchen, N. G. White, G. N. L. Jameson, J. L. Tallon and S. Brooker, *Inorg. Chem.*, 2011, **50**, 4586–4597.
82 A. Bhattacharjee, M. Roy, V. Ksenofontov, J. A. Kitchen, S. Brooker and P. Gütlich, *Eur. J. Inorg. Chem.*, 2013, 843–849.
83 K. Nakano, S. Kawata, K. Yoneda, A. Fuyuhiro, T. Yagi, S. Nasu, S. Morimoto and S. Kaizaki, *Chem. Commun.*, 2004, 2892–2893.
84 J. A. Kitchen, J. Olguín, R. Kulmaczewski, N. G. White, V. A. Milway, G. N. L. Jameson, J. L. Tallon and S. Brooker, *Inorg. Chem.*, 2013, **52**, 11185–11199.

85 R. Kulmaczewski, J. Olguín, J. A. Kitchen, H. L. C. Feltham, G. N. L. Jameson, J. L. Tallon and S. Brooker, *J. Am. Chem. Soc.*, 2014, **136**, 878–881.
86 R. W. Hogue, H. L. C. Feltham, R. G. Miller and S. Brooker, *Inorg. Chem.*, 2016, **55**, 4152–4165.
87 N. G. White and S. Brooker, *Polyhedron*, 2016, **103**, 283–287.
88 C. F. Herold, L. M. Carrella and E. Rentschler, *Eur. J. Inorg. Chem.*, 2015, 3632–3636.
89 C. F. Herold, S. I. Shylin and E. Rentschler, *Inorg. Chem.*, 2016, **55**, 6414–6419.
90 C. Köhler and E. Rentschler, *Eur. J. Inorg. Chem.*, 2016, 1955–1960.
91 J. J. M. Amoore, C. J. Kepert, J. D. Cashion, B. Moubaraki, S. M. Neville and K. S. Murray, *Chem. – Eur. J.*, 2006, **12**, 8220–8227.
92 C. J. Schneider, J. D. Cashion, N. F. Chilton, C. Etrillard, M. Fuentealba, J. A. K. Howard, J. F. Létard, C. Milsmann, B. Moubaraki, H. A. Sparkes, S. R. Batten and K. S. Murray, *Eur. J. Inorg. Chem.*, 2013, 850–864.
93 S. Rodríguez-Jiménez, H. L. C. Feltham and S. Brooker, *Angew. Chem., Int. Ed.*, 2016, **55**, 15067–15071, and back cover.
94 S. Samanta, S. Demesko, S. Dechert and F. Meyer, *Angew. Chem., Int. Ed.*, 2015, **54**, 583–587.
95 S. Kanegawa, S. Kang and O. Sato, *Eur. J. Inorg. Chem.*, 2013, 725–729.
96 J.-F. Létard, P. Guionneau, O. Nguyen, J. S. Costa, S. Marcén, G. Chastanet, M. Marchivie and L. Goux-Capes, *Chem. – Eur. J.*, 2005, **11**, 4582–4589.
97 S. Heider, H. Petzold and G. Teucher, *Eur. J. Inorg. Chem.*, 2013, 2382–2388.
98 A. Y. Verat, N. Ould-Moussa, E. Jeanneau, L. G. Boris, A. Boussekou, S. A. Borshch and G. S. Matouzenko, *Chem. – Eur. J.*, 2009, **15**, 10070–10082.
99 G. S. Matouzenko, E. Jeanneau, A. Y. Verat and A. Bousseksou, *Dalton Trans.*, 2011, **40**, 9608–9618.
100 G. S. Matouzenko, E. Jeanneau, A. Y. Verat and Y. d. Gaetano, *Eur. J. Inorg. Chem.*, 2012, 969–977.
101 Y. d. Gaetano, E. Jeanneau, A. Y. Verat, L. Rechignat, A. Bousseksou and G. S. Matouzenko, *Eur. J. Inorg. Chem.*, 2013, 1015–1023.
102 V. Ksenofontov, A. B. Gaspar, J. A. Real and P. Gütlich, *J. Phys. Chem. B*, 2001, **105**, 12266–12271.
103 H. J. Shepherd, P. Rosa, L. Vendier, N. Casati, J.-F. Létard, A. Bousseksou, P. Guionneau and G. Molnár, *Phys. Chem. Chem. Phys.*, 2012, **14**, 5265–5271.
104 D. Fedaoui, Y. Bouhadja, A. Kaiba, P. Guionneau, J.-F. Létard and P. Rosa, *Eur. J. Inorg. Chem.*, 2008, 1022–1026.
105 N. Ortega-Villar, A. Thompson, M. C. Muñoz, V. M. Ugalde-Saldívar, A. E. Goeta, R. Moreno-Esparza and J. A. Real, *Chem. – Eur. J.*, 2005, **11**, 5721–5734.
106 E. Milin, S. Belaïd, V. Patinec, S. Triki, G. Chastanet and M. Marchivie, *Inorg. Chem.*, 2016, **55**, 9038–9046.
107 M. Yamasaki and T. Ishida, *Chem. Lett.*, 2015, **44**, 920–921.
108 J. G. Park, I.-R. Jeon and T. D. Harris, *Inorg. Chem.*, 2015, **54**, 359–369.
109 G. Vos, R. A. le Fèbre, R. A. G. de Graaff, J. G. Haasnoot and J. Reedijk, *J. Am. Chem. Soc.*, 1983, **105**, 1682–1683.
110 J. J. A. Kolnaar, G. v anDijk, H. Kooijman, A. L. Spek, V. G. Ksenofontov, P. Gütlich, J. G. Haasnoot and J. Reedijk, *Inorg. Chem.*, 1997, **36**, 2433–2440.
111 M. Thomann, O. Kahn, J. Guilhem and F. Varret, *Inorg. Chem.*, 1994, **33**, 6029–6037.
112 Y. Garcia, P. Guionneau, G. Bravic, D. Chasseau, J. A. K. Howard, O. Kahn, V. Ksenofontov, S. Reiman and P. Gütlich, *Eur. J. Inorg. Chem.*, 2000, 1531–1538.
113 D. Savard, C. Cook, G. D. Enright, I. Korobkov, T. J. Burchell and M. Murugesu, *CrystEngComm*, 2011, **13**, 5190–5197.
114 V. Gómez, J. Benet-Buchholz, E. Martin and J. R. Galán-Mascarós, *Chem. – Eur. J.*, 2014, **20**, 5369–5379.
115 V. Gómez, C. Sáenz de Pipaón, P. Maldonado-Illescas, J. C. Waerenborgh, E. Martin, J. Benet-Buchholz and J. R. Galán-Mascarós, *J. Am. Chem. Soc.*, 2015, **137**, 11924–11927.
116 Y. Klein, N. Sciortino, C. Housecroft, C. Kepert and S. Neville, *Magnetochemistry*, 2016, **2**, 7.
117 N. Pittala, F. Thetiot, C. Charles, S. Triki, K. Boukheddaden, G. Chastanet and M. Marchivie, *Chem. Commun.*, 2017, **53**, 8356–8359.
118 W.-B. Chen, Y.-C. Chen, M. Yang, M.-L. Tong and W. Dong, *Dalton Trans.*, 2018, **47**, 4307–4314.
119 H. Vahrenkamp, A. Gei and G. N. Richardson, *J. Chem. Soc., Dalton Trans.*, 1997, 3643–3652.
120 S. Dhers, H. L. C. Feltham and S. Brooker, *Coord. Chem. Rev.*, 2015, **296**, 24–44.
121 C. P. Berlinguette, A. Dragulescu-Andrasi, A. Sieber, J. R. Galán-Mascarós, H.-U. Güdel, C. Achim and K. R. Dunbar, *J. Am. Chem. Soc.*, 2004, **126**, 6222–6223.
122 M. Nihei, M. Ui, M. Yokota, L. Han, A. Maeda, H. Kishida, H. Okamoto and H. Oshio, *Angew. Chem., Int. Ed.*, 2005, **44**, 6484–6487.
123 M. Nihei, M. Ui and H. Oshio, *Polyhedron*, 2009, 1718–1721.
124 O. Hietsoi, P. W. Dunk, H. D. Stout, A. Arroyave, K. Kovnir, R. E. Irons, N. Kassenova, R. Erkasov, C. Achim and M. Shatruk, *Inorg. Chem.*, 2014, **53**, 13070–13077.
125 I. Boldog, F. J. Muñoz-Lara, A. B. Gaspar, M. C. Muñoz, M. Seredyuk and J. A. Real, *Inorg. Chem.*, 2009, **48**, 3710–3719.
126 R.-J. Wei, Q. Huo, J. Tao, R.-B. Huang and L.-S. Zheng, *Angew. Chem., Int. Ed.*, 2011, **50**, 8940–8943.
127 E. Breuning, M. Ruben, J.-M. Lehn, F. Renz, Y. Garcia, V. Ksenofontov, P. Gütlich, E. Wegelius and K. Rissanen, *Angew. Chem., Int. Ed.*, 2000, **39**, 2504–2507.
128 M. Ruben, E. Breuning, J.-M. Lehn, V. Ksenofontov, F. Renz, P. Gütlich and G. B. M. Vaughan, *Chem. – Eur. J.*, 2003, **9**, 4422–4429.
129 M. Ruben, U. Ziener, J.-M. Lehn, V. Ksenofontov, P. Gütlich and G. B. M. Vaughan, *Chem. – Eur. J.*, 2005, **11**, 94–100.
130 L. H. Uppadine, J.-P. Gisselbrecht, N. Kyritsakas, K. Nättinen, K. Rissanen and J.-M. Lehn, *Chem. – Eur. J.*, 2005, **11**, 2549–2565.

131 A. R. Stefankiewicz, G. Rogez, J. Harrowfield, M. Drillon and J.-M. Lehn, *Dalton Trans.*, 2009, 5787–5802.
132 A. R. Stefankiewicz, G. Rogez, J. Harrowfield, A. N. Sobolev, A. Madalan, J. Huuskonen, K. Rissanen and J.-M. Lehn, *Dalton Trans.*, 2012, **41**, 13848–13855.
133 M. Steinert, B. Schneider, S. Dechert, S. Demeshko and F. Meyer, *Inorg. Chem.*, 2016, **55**, 2363–2373.
134 D.-Y. Wu, O. Sato, Y. Einaga and C.-Y. Duan, *Angew. Chem., Int. Ed.*, 2009, **48**, 1475–1478.
135 Y.-T. Wang, S.-T. Li, S.-Q. Wu, A.-L. Cui, D.-Z. Shen and H.-Z. Kou, *J. Am. Chem. Soc.*, 2013, **135**, 5942–5945.
136 T. Matsumoto, G. N. Newton, T. Shiga, S. Hayami, Y. Matsui, H. Okamoto, R. Kumai, Y. Murakami and H. Oshio, *Nat. Commun.*, 2014, **5**, 3865.
137 B. Schäfer, J.-F. Greisch, I. Faus, T. Bodenstein, I. Šalitroš, O. Fuhr, K. Fink, V. Schünemann, M. M. Kappes and M. Ruben, *Angew. Chem., Int. Ed.*, 2016, **55**, 10881–10885.
138 M. Steinert, B. Schneider, S. Dechert, S. Demeshko and F. Meyer, *Angew. Chem., Int. Ed.*, 2014, **53**, 6135–6139.
139 B. Schneider, S. Demeshko, S. Dechert and F. Meyer, *Inorg. Chem.*, 2012, **51**, 4912–4914.
140 A. Ferguson, M. A. Squire, D. Siretanu, D. Mitcov, C. Mathonière, R. Clérac and P. E. Kruger, *Chem. Commun.*, 2013, **49**, 1597–1599.
141 R. A. Bilbeisi, S. Zarra, H. L. C. Feltham, G. N. L. Jameson, J. K. Clegg, S. Brooker and J. R. Nitschke, *Chem. – Eur. J.*, 2013, **19**, 8058–8062.
142 L. Li, N. Saigo, Y. Zhang, D. J. Fanna, N. D. Shepherd, J. K. Clegg, R. Zheng, S. Hayami, L. F. Lindoy, J. R. Aldrich-Wright, C.-G. Li, J. K. Reynolds, D. G. Harman and F. Li, *J. Mater. Chem. C*, 2015, **3**, 7878–7882.
143 D.-H. Ren, D. Qiu, C.-Y. Pang, Z. Li and Z.-G. Gu, *Chem. Commun.*, 2015, **51**, 788–791.
144 F.-L. Zhang, J.-Q. Chen, L.-F. Qin, L. Tian, Z. Li, X. Ren and Z.-G. Gu, *Chem. Commun.*, 2016, **52**, 4796–4799.
145 M. P. Shores, C. M. Klug and S. R. Fiedler, *Spin-Crossover Materials: Properties and Applications*, John Wiley & Sons Ltd, Chichester, 2013, pp. 281–301.
146 M. B. Duriska, S. M. Neville, B. Moubaraki, J. D. Cashion, G. J. Halder, K. W. Chapman, C. Balde, J.-F. Létard, K. S. Murray, C. J. Kepert and S. R. Batten, *Angew. Chem., Int. Ed.*, 2009, **48**, 2549–2552.
147 Z. Yan, W. Liu, Y.-Y. Peng, Y.-C. Chen, Q.-W. Li, Z.-P. Ni and M.-L. Tong, *Inorg. Chem.*, 2016, **55**, 4891–4896.
148 K. Yoneda, K. Adachi, K. Nishio, M. Yamasaki, A. Fuyuhiro, M. Katada, S. Kaizaki and S. Kawata, *Angew. Chem., Int. Ed.*, 2006, **45**, 5459–5461.
149 X. Bao, J.-D. Leng, Z.-S. Meng, Z. Lin, M.-L. Tong, M. Nihei and H. Oshio, *Chem. – Eur. J.*, 2010, **16**, 6169–6174.
150 M. B. Duriska, S. M. Neville, B. Moubaraki, K. S. Murray, C. Balde, J.-F. Létard, C. J. Kepert and S. R. Batten, *ChemPlusChem*, 2012, **77**, 616–623.
151 S. Alvarez, *Chem. Rev.*, 2015, **115**, 13447–13483.
152 M. Llunell, D. Casanova, J. Cirera, P. Alemany and S. Alvarez, SHAPE (2.1), University of Barcelona, Spain, 2013.
153 S. Alvarez, P. Alemany, D. Casanova, J. Cirera, M. Llunell and D. Avnir, *Coord. Chem. Rev.*, 2005, **249**, 1693–1708.
154 S. Alvarez, D. Avnir, M. Llunell and M. Pinsky, *New J. Chem.*, 2002, **26**, 996–1009.
155 J.-M. Lehn, *Supramolecular chemistry: concepts and perspectives*, VCH, Weinheim, 1995.
156 S. Leininger, B. Olenyuk and P. J. Stang, *Chem. Rev.*, 2000, **100**, 853–908.
157 H. S. Scott, R. W. Staniland and P. E. Kruger, *Coord. Chem. Rev.*, 2018, **362**, 24–43.
158 A. J. McConnell, *Supramol. Chem.*, 2018, **30**, 858–868.
159 K. Nakano, N. Suemura, K. Yoneda, S. Kawata and S. Kaizaki, *Dalton Trans.*, 2005, 740–743.
160 L. J. Kershaw Cook, R. Kulmaczewski, R. Mohammed, S. Dudley, S. A. Barrett, M. A. Little, R. J. Deeth and M. A. Halcrow, *Angew. Chem., Int. Ed.*, 2016, **55**, 4327–4331.
161 H. Phan, J. J. Hrudka, D. Igimbayeva, L. M. Lawson Daku and M. Shatruk, *J. Am. Chem. Soc.*, 2017, **139**, 6437–6447.
162 S. Rodríguez-Jiménez, M. Yang, I. Stewart, A. L. Garden and S. Brooker, *J. Am. Chem. Soc.*, 2017, **139**, 18392–18396.
163 A. Kimura and T. Ishida, *ACS Omega*, 2018, **3**, 6737–6747.
164 S. Rodríguez-Jiménez, A. S. Barltrop, N. G. White, H. L. C. Feltham and S. Brooker, *Inorg. Chem.*, 2018, **57**, 6266–6282.

